

AEDC-TR-06-6



Real-Time Processing of Pressure-Sensitive Paint Images

**Wim Ruyten
Aerospace Testing Alliance**

December 2006

Final Report for Period October 1, 2001 to September 30, 2004

STATEMENT A: Cleared for public release; distribution is unlimited.

**ARNOLD ENGINEERING DEVELOPMENT CENTER
ARNOLD AIR FORCE BASE, TENNESSEE
AIR FORCE MATERIEL COMMAND
UNITED STATES AIR FORCE**

NOTICES

When U. S. Government drawings, specifications, or other data are used for any purpose other than a definitely related Government procurement operation, the Government thereby incurs no responsibility nor any obligation whatsoever, and the fact that the Government may have formulated, furnished, or in any way supplied the said drawings, specifications, or other data, is not to be regarded by implication or otherwise, as in any manner licensing the holder or any other person or corporation, or conveying any rights or permission to manufacture, use or sell any patented invention that may in any way be related thereto.

Qualified users may obtain copies of this report from the Defense Technical Information Center.

References to named commercial products in this report are not to be considered in any sense as an endorsement of the product by the United States Air Force or the Government.

DESTRUCTION NOTICE

For unclassified documents, destroy by any method that will prevent disclosure or reconstruction of the document.

APPROVAL STATEMENT

This report has been reviewed and approved.



STEVEN A. BANCROFT
Applied Technology Division
Test Operations Directorate

Approved for publication:

FOR THE COMMANDER



ROBERT T. CROOK
Deputy Chief, Applied Technology Division
Test Operations Directorate

REPORT DOCUMENTATION PAGE					Form Approved OMB No. 0704-0188	
<p>The public reporting burden for this collection of information is estimated to average 1 hour per response, including the time for reviewing instructions, searching existing data sources, gathering and maintaining the data needed, and completing and reviewing the collection of information. Send comments regarding this burden estimate or any other aspect of this collection of information, including suggestions for reducing the burden, to Department of Defense, Washington Headquarters Services, Directorate for Information Operations and Reports (0704-0188), 1215 Jefferson Davis Highway, Suite 1204, Arlington, VA 22202-4302. Respondents should be aware that notwithstanding any other provision of law, no person shall be subject to any penalty for failing to comply with a collection of information if it does not display a currently valid OMB control number.</p> <p>PLEASE DO NOT RETURN YOUR FORM TO THE ABOVE ADDRESS</p>						
1. REPORT DATE (DD-MM-YYYY) 00-12-2006			2. REPORT TYPE Final		3. DATES COVERED (From – To) October 1, 2001 to September 30, 2004	
4. TITLE AND SUBTITLE Real-Time Processing of Pressure-Sensitive Paint Images				5a. CONTRACT NUMBER F40600-03-R-0001		
				5b. GRANT NUMBER		
				5c. PROGRAM ELEMENT NUMBER		
6. AUTHOR(S) Wim Ruyten Aerospace Testing Alliance				5d. PROJECT NUMBER 9830		
				5e. TASK NUMBER		
				5f. WORK UNIT NUMBER		
7. PERFORMING ORGANIZATION NAME(S) AND ADDRESS(ES) AEDC/DOT 1099 Avenue C Arnold AFB, TN 37389-9013					8. PERFORMING ORGANIZATION REPORT NO. AEDC-TR-06-6	
9. SPONSORING/MONITORING AGENCY NAME(S) AND ADDRESS(ES) Air Force Office of Scientific Research 4015 Wilson Blvd, Room 713 Arlington, VA 22203-1954					10. SPONSOR/MONITOR'S ACRONYM(S) AFRL/AFOSR	
					11. SPONSOR/MONITOR'S REPORT NUMBER(S)	
12. DISTRIBUTION/AVAILABILITY STATEMENT Statement A: Approved for public release; distribution is unlimited.						
13. SUPPLEMENTARY NOTES Available in Defense Technical Information Center (DTIC).						
14. ABSTRACT The Arnold Engineering Development Center is one of the leading aerospace test centers to use pressure-sensitive paint (PSP) technology to measure full-field pressure distributions on the surfaces of test articles in a wind tunnel. This report addresses one of the principal challenges identified prior to the start of this reporting period: automated, on-line processing of the large amounts of image data that are acquired during a typical PSP test. This report shows that this image-processing challenge has been met successfully through innovations with regard to automatic image registration and parallel processing. This report also describes additional studies performed to guide the continued development of improved paints and data acquisition strategies for the application of lifetime-based PSP techniques.						
15. SUBJECT TERMS Pressure-sensitive paint, automatic image registration, on-line processing, template matching, lifetime analysis, aerodynamic testing						
16. SECURITY CLASSIFICATION OF:			17. LIMITATION OF ABSTRACT	18. NUMBER OF PAGES	19a. NAME OF RESPONSIBLE PERSON	
a. REPORT	b. ABSTRACT	c. THIS PAGE			Steven A. Bancroft	
Unclassified	Unclassified	Unclassified	Same as Report	90	19b. TELEPHONE NUMBER (Include area code) (931) 454-6418	

PREFACE

The work reported herein was conducted by the Arnold Engineering Development Center (AEDC), Air Force Materiel Command (AFMC), under funding from the Air Force Office of Scientific Research (AFOSR). The results of the research were obtained by Aerospace Testing Alliance, the operations, maintenance, information management, and support contractor for AEDC, AFMC, Arnold Air Force Base, Tennessee, under Project Number 9830. The Air Force Project Managers were Drs. Neil Glassman, Thomas Beutner, and John Schmisser for AFOSR and Mr. Steven A. Bancroft for AEDC. The author is also indebted to his colleagues at AEDC, in particular, Mr. Marvin Sellers and Mr. Daryl Sinclair.

CONTENTS

1.0	INTRODUCTION.....	7
2.0	ON-LINE PROCESSING OF PRESSURE-SENSITIVE PAINT IMAGES	9
2.1	Overview	9
2.2	Introduction.....	9
2.3	Theory	9
2.3.1	Paint Response.....	9
2.3.2	Image Mapping.....	10
2.3.3	Self-Illumination (SI) Correction	11
2.4	Processing Schemes	12
2.5	Benchmarks.....	13
2.6	Software and Hardware.....	14
2.6.1	Software.....	14
2.6.2	Hardware	16
2.6.3	Implementation.....	16
2.7	Timing Results	17
2.8	Concluding Remarks	18
3.0	MESSAGE PASSING FOR PARALLEL PROCESSING OF PRESSURE-SENSITIVE PAINT IMAGES.....	19
3.1	Overview	19
3.2	Introduction.....	19
3.3	Parallelization Approach.....	19
3.4	Implementation	20
3.5	Results	22
3.6	Conclusion	23
3.7	Appendix 3A: Green Boot Run Modes.....	23
3.8	Acknowledgments.....	24
4.0	AUTOMATIC IMAGE REGISTRATION FOR OPTICAL TECHNIQUES IN AERODYNAMIC TEST FACILITIES	25
4.1	Overview	25
4.2	Introduction.....	25
4.3	Review of Photogrammetry	25
4.4	Sting Model.....	27
4.5	Resulting Prediction Model.....	29
4.6	Template-Based Target Search	30
4.6.1	Calculation of the Search Template.....	32
4.6.2	Conventional Template Matching	33
4.6.3	Augmented Template Matching	34
4.7	Completion of the Image Registration Task	35
4.8	Implementation of Algorithm and Its Use.....	36
4.9	Sample Results	37
4.10	Conclusion	37
4.11	Acknowledgments.....	38
5.0	EXTENSION OF SUBPIXEL-AUGMENTED TEMPLATE MATCHING TO IMPERFECTLY RENDERED BINARY TARGETS	39
5.1	Overview	39

5.2	Introduction	39
5.3	Review of Concept	39
5.4	Review of Theory for Binary Scene	41
5.5	Application to Binary Scenes	42
5.5.1	Pressure-Sensitive Paint Tests	43
5.5.2	Model Attitude Tests	44
5.6	Extension to Nonbinary Scenes: Theory	44
5.7	Extension to Nonbinary Scenes: Practice	46
5.8	Conclusion	48
5.9	Acknowledgments	49
5.10	Appendix 5A: Global RMS Fit Error	49
5.11	Appendix 5B: Justification of Composite Similarity Measure	49
6.0	IMPROVED DATA PROCESSING FOR PRESSURE-SENSITIVE PAINT MEASUREMENTS IN A PRODUCTION FACILITY	50
6.1	Overview	50
6.2	Introduction	50
6.3	Review of Prior Processing Scheme	50
6.4	Improvements to Processing Scheme	52
6.5	Sample Results for NASA Space Shuttle Test	55
6.6	Discussion	57
6.7	Acknowledgments	58
6.8	Appendix 6A: Improved Mapping Scheme	58
6.9	Appendix 6B: Overlapping Camera Views	58
7.0	ASSIMILATION OF PHYSICAL CHEMISTRY MODELS FOR LIFETIME ANALYSIS OF PRESSURE-SENSITIVE PAINT	60
7.1	Overview	60
7.2	Introduction	60
7.3	Lifetime Models from Physical Chemistry	61
7.3.1	Paint as a Microheterogeneous System	61
7.3.2	Discrete Exponential Model	62
7.3.3	Förster Decay Model	62
7.3.4	Maximum Entropy Model	63
7.3.5	Excitation Response Function	64
7.3.6	Reconstruction of Decay Rate Distribution from Fluorescence Response	64
7.4	Lifetime Analysis of PtTFPP in FIB	65
7.4.1	Experiment	65
7.4.2	Data Analysis	66
7.4.3	Interpretation of Results	70
7.5	Discussion	71
7.6	Appendix 7A: Derivation of Proportionality Constant	71
7.7	Appendix 7B: Conditions for Linear Excitation and Fluorescence	72
7.8	Appendix 7C: Special Pulse Shapes	73
7.9	Acknowledgments	74
8.0	OXYGEN QUENCHING OF PTTFPP IN FIB POLYMER: A SEQUENTIAL PROCESS?	75
8.1	Overview	75
8.2	Introduction	75
8.3	Experiment	75

8.4	Analysis.....	76
8.5	Results.....	76
8.6	Proposed Model	77
8.7	Discussion	78
8.8	Acknowledgments.....	78
9.0	OPTIMIZATION OF THREE-GATE LIFETIME PRESSURE- AND TEMPERATURE- SENSITIVE PAINT MEASUREMENTS	79
9.1	Overview	79
9.2	Introduction.....	79
9.3	Review of Previous Work	79
9.4	Three-Gate vs. Two-Gate Measurements.....	82
9.5	Paint Optimization	83
9.6	Discussion	85
9.7	Appendix 9A: Derivation of Two-Gate and Three-Gate Shot-Noise Errors.....	85
9.8	Acknowledgment	86
	REFERENCES.....	87

TABLE OF FIGURES

1.	Example of PSP Calibration Curves	10
2.	Example of PSP Image with Registration Targets	11
3.	Basic Processing Sequences.....	13
4.	Examples of Processed Data for the Two Benchmark Cases.....	13
5.	Schematic of Wind Tunnel Setup with Positions of the Eight Cameras Shown	14
6.	Illustration of Effect of Self-Illumination Correction on X-38 Tail Section.....	15
7.	Parallel-Processing Implementation for the Processing Schemes from Fig. 3.....	16
8.	Master-Slave Approach to PSP Data Processing	19
9.	Typical Master Macro Script.....	20
10.	Typical Realization of slave_macro in Fig. 9	20
11.	Implementation of Master-Slave Communication through File Descriptors	21
12.	Interprocess Communication via System-Level WRITE and READ Calls	21
13.	Fork-Pipe Implementation with Master and Slave Processes	21
14.	TCP/IP Implementation with Master and Slave Processes	22
15.	Schematic of Imaging Process	26
16.	Schematic of Sting-Deflecting Model.....	28
17.	Sting Deflection of F-16C Model Under Air Loads.....	28
18.	Illustration of Use of Search Template.....	31
19.	Example of Conventional Search Template.....	31
20.	Augmented Templates Corresponding to Fig. 19.....	31
21.	Calculation of Template from Polygonal Curve	32
22.	Correlation Sums Arising in Augmented Template Search	34
23.	Image Registration Flow Diagram	36
24.	Example of Augmented Template.....	40
25.	Determination of AT Derivative Terms	40
26.	Flow Diagram for Augmented Template Search and Centering	41
27.	Demonstration of AT-Based SR Detection and Centering for Test I of Table 7	43
28.	AT-Based Convergence Rates of Centering Loop in Fig. 26.....	44
29.	Image from Test III of Table 7, with SRs Detected by the AT Scheme	44

30. Image of Calibration Plate in Test III with SRs Detected by the AT Scheme	45
31. Division of Search Template into Subtemplates	45
32. Detected SRs from Test III Found Using the CAT Scheme	47
33. Detected SRs from Tests I and II Found Using the CAT Scheme	47
34. Comparison of AT and CAT Correlation Values	47
35. Comparison of Predicted Centering Precisions for Data from Fig. 34	48
36. Comparison of Measured and Predicted Precisions for Data from Fig. 34	48
37. Key Processing Steps Prior to Improvements	51
38. Improved Processing Sequence	52
39. Schematic of Mapped Grid Projected onto Image	53
40. Schematic of Eight-Camera PSP System	54
41. Mapped Pressure Distribution on Space Shuttle Model	56
42. Pixel-Based Precision Associated with Fig. 41	56
43. Number of Camera Views for Fig. 41	56
44. Camera-Based Precision Associated with Fig. 41	56
45. Example of Elimination of Seam Resulting from Improved Processing	57
46. Illustration of DEM Decay Rate Distribution	62
47. Illustration of FDM	63
48. Illustration of MEM Decay Rate Distribution	63
49. Normalized Illumination Pulse Shape	66
50. Selected Fluorescence Response Curves for PtTFPP in FIB	66
51. Fit Residuals for Data from Fig. 50 for Four Models	67
52. RMS Fit Residuals as a Function of Pressure	68
53. Implied Decay Rate Distribution for Data from Fig. 50	68
54. Areas Under Distribution Function as a Function of Pressure	68
55. Förster Parameters a and b as a Function of Pressure	69
56. Stern-Volmer Diagram with Peak Positions Versus Pressure	69
57. Peak Area Fractions Associated with Fig. 56	70
58. Pulse Shapes and ERFs from Table 10	74
59. Schematic of Proposed Sequential Decay Process	77
60. Peak Positions and Contribution Fractions for Sequential Decay Model	78
61. Schematic of Gated Measurement	80
62. Dependence of Signal Ratio on Pressure and Temperature	80
63. Error Sources in Two-Gate PSP	83
64. Error Sources in Three-Gate PSP	83

TABLES

1. Benchmark Data Sets	14
2. Support Files for Data Processing	15
3. Cumulative Single-Processor Times (in Seconds) for X-38 Data on SGI Octane 2	17
4. Processing Times per Data Point in Seconds	17
5. Parallel Processing Times per Data Point in Seconds	23
6. Selected Data from Three Wind Tunnel Tests	38
7. Parameters for Wind Tunnel Tests Considered in this Study	42
8. Comparison of Centering Errors for Calibration Plate in Test III of Table 7	45
9. Fitted Stern-Volmer Parameters for PtTFPP in FIB at 70°F	70
10. Excitation Response Functions for Selected Pulse Shapes	73
11. Paint Parameters at 1 atm and 25°C	81

1.0 INTRODUCTION

The Arnold Engineering Development Center (AEDC) is one of the leading aerospace test centers in the world and operates many facilities that have unmatched capabilities anywhere. In addition, AEDC strives to offer its customers, both military and commercial, the best measurement techniques available. Among the newest of these techniques is the use of pressure-sensitive paint (PSP) for the measurement of full-field pressure distributions on the surfaces of test articles.

Introduced in the early 1990s, PSP techniques have since gone through a significant maturation process, but prior to the start of Air Force Office of Scientific Research (AFOSR) contract F40600-03-R-0001, a principal challenge remained: automated, online processing of the large amounts of image data that are acquired during a typical PSP test. It was not unusual for such data reduction to take weeks following completion of the test. This was unsatisfactory to test customers and has posed a significant challenge to scientists and engineers. This challenge was the motivation for the present AFOSR contract.

This report shows that the image-processing challenge has been met successfully, in large part because of the support of AFOSR. This success is rooted not merely in the development of improved software, per se. Several noteworthy innovations have been developed with regard to automatic image registration and parallel processing—innovations that have the potential for leading to improved data-processing techniques in other disciplines.

Furthermore, as a direct result of the support provided by AFOSR, opportunities have arisen to improve not only the speed with which data from a PSP test can be processed, but also the quality of the resulting data. In addition, several studies have been performed to guide the continued development of improved paints and data acquisition strategies for the application of lifetime-based PSP techniques (for example, the kind of strategies being pursued under AFOSR contract STTR-AF04-T001, “Improved Pressure- and Temperature-Sensitive Paint.”)

This report consists of previously published material that was made possible with AFOSR support under this contract. The material has been reformatted into a cohesive report, with cross-references between sections, where applicable. A complete list of publications generated under this contract follows, with a brief explanation of how this material was merged into the present report.

SOURCE DOCUMENTS

1. W. Ruyten and M. Sellers, “On-Line Processing of Pressure-Sensitive Paint Images,” *Journal of Aerospace Computing, Information, and Communication*, Vol. 1, September 2004, pp. 372-382. This material is presented first (in Section 2.0 of the present report), because it provides a good introduction both to the problem of automated processing and to the approach to its solution.
2. W. Ruyten and M. Sellers, “On-Line Processing of Pressure-Sensitive Paint Images,” AIAA Paper 2003-3947, 21st AIAA Applied Aerodynamics Conference, Orlando, Florida, June 23-26, 2003. This paper is an earlier version of the material in Doc. 1, above.
3. W. Ruyten and W. E. Sisson, “Message-Passing for Parallel Processing of Pressure-Sensitive Paint Images,” DoD HPCMP Users Group Conference, Williamsburg, Virginia, June 7-11, 2004, published by IEEE as ISBN 0-7695-2259-9, pp. 308-312. This material is presented in Section 3.0 of the present report.
4. W. Ruyten, “Automatic Image Registration for Optical Techniques in Aerodynamic Test Facilities,” AIAA Paper 2004-2400, 24th AIAA Aerodynamic Measurement Technology and Ground Testing Conference, Portland, Oregon, June 28-July 1, 2004 [one of two papers (out of a field 118 papers) to be presented with an outstanding paper award]. This material is presented in Section 4.0 of the present report.

5. W. Ruyten, "Sting Deflection Model for Automatic Image Registration in Wind Tunnel Testing," *Journal of Aircraft*, Vol. 43, No. 3, May – June 2006, pp. 853-855. This material was extracted from Doc. 4, above.
6. W. Ruyten, "Implementation of Template-Based Image Registration for Aerodynamic Testing," *Journal of Aerospace Computing, Information, and Communication*, Vol. 3, No. 4, April 2006, pp. 138-145. This material also was extracted from Doc. 4, above.
7. W. Ruyten, "Extension of Subpixel Augmented Template Matching to Imperfectly Rendered Binary Targets," *Optical Engineering*, Vol. 43, No. 3, March 2004, pp. 639-647. This paper was initiated prior to the AFOSR contract as an IEEE conference paper but was brought to completion as a refereed publication with the support of AFOSR. The material is presented in Section 5.0 of this report.
8. W. Ruyten and M. Sellers, "Improved Data Processing for Pressure-Sensitive Paint Measurements in a Production Facility," AIAA Paper 2006-1042, 44th Aerospace Sciences Meeting and Exhibit, Reno, Nevada, 9-12 January, 2006. This material forms the culmination of the work that was performed under the AFOSR contract. It reflects the innovations that were made possible with the support of AFOSR, while demonstrating their applicability to a series of wind tunnel tests conducted at AEDC in support of the Return-to-Flight program for the U.S. Space Shuttle.
9. W. Ruyten, "Assimilation of Physical Chemistry Models for Lifetime Analysis of Pressure-Sensitive Paint," *AIAA Journal*, Vol. 43, No. 3, March 2005, pp. 465-471. This material is presented in Section 7.0 of the present report and reflects a shift from image processing per se to understanding the inherent fluorescence dynamics of lifetime-based PSP measurements.
10. W. Ruyten, "Assimilation of Physical Chemistry Models for Lifetime Analysis of Pressure-Sensitive Paint," AIAA Paper 2004-0880, 42nd AIAA Aerospace Sciences Meeting and Exhibit, Reno, Nevada, January 5-8, 2004. This paper (along with Doc. 11, below) formed the basis for Doc. 9. Some of the material from Doc. 10 that is not included in Doc. 9 is also included in Section 7.0 of the present report.
11. W. Ruyten and M. Sellers, "Lifetime Analysis of the Pressure-Sensitive Paint PtTFPP in FIB," AIAA Paper 2004-0881, 42nd AIAA Aerospace Sciences Meeting and Exhibit, Reno, Nevada, January 5-8, 2004. This paper is an earlier version of the material published in Docs. 7 and 10.
12. W. Ruyten, "Oxygen quenching of PtTFPP in FIB Polymer: A Sequential Process?" *Chemical Physics Letters*, Vol. 394, No. 1-3, 2004, pp. 101-104. This material is presented in Section 8.0 of the present report.
13. W. Ruyten, "Optimization of Three-Gate Lifetime Pressure- and Temperature-Sensitive Paint Measurements," AIAA Paper 2004-2190, 24th AIAA Aerodynamic Measurement Technology and Ground Testing Conference, Portland, Oregon, June 28-July 1, 2004. This material is presented in Section 9.0 of the present report. An updated version of this paper will also be published as a Technical Note in the *AIAA Journal*.

2.0 ON-LINE PROCESSING OF PRESSURE-SENSITIVE PAINT IMAGES*

2.1 OVERVIEW

Section 2.0 documents a milestone that has been reached at AEDC, namely to reduce data reduction times for both intensity-based and lifetime-based pressure-sensitive paint measurements from an eight-camera system sufficiently that one data point can be processed in full (in 5 to 10 seconds) while the next data point is being acquired. This paper describes the hardware, software, and data reduction strategies used, and it presents results for benchmark data from wind tunnel tests on scale models of an F-16C fighter jet and NASA's X-38 Crew Return Vehicle.

2.2 INTRODUCTION

Pressure-sensitive paint (PSP) has established itself as an important test and evaluation tool in the area of aerodynamic testing, particularly for use in transonic wind tunnels.¹⁻⁷ Most commonly, the luminescence from the painted test article is captured using digital cameras. Thus, PSP is essentially an image-based technique. (The much less frequently used approach based on a scanned laser spot system is not considered here.) To achieve full coverage across the surface of the test article, multiple cameras typically are used. Data are then processed and presented to the test customer either in 2D image format or as data that have been mapped to a 3D grid of the test article. The latter format is preferred because it allows force and moment integrations to be performed, across either the whole surface or parts thereof.

Considerable computational resources are required to convert raw images into fully processed PSP data. In the past, days or weeks were required to perform this task. Over the years, analysis techniques have become more sophisticated and computers have become faster, making it possible, at present, to process data while a wind tunnel test is in progress. The purpose of this section is to review the technology that has made this milestone possible at AEDC.

2.3 THEORY

2.3.1 Paint Response

The theory behind PSP has been reviewed extensively elsewhere.^{1,2} At the heart of PSP processing is the notion that the pressure, P , can be obtained from a ratio, R , of two signals, $S^{(1)}$ and $S^{(2)}$, by a calibration function, $P(R, T)$, where T is the temperature. Symbolically, this may be written as

$$R_{ij} = S_{ij}^{(1)} / S_{ij}^{(2)} \quad (1)$$

and

$$P_{ij} = P(R_{ij}, T). \quad (2)$$

The subscripts ij indicate that the respective quantities may be thought of as pixel values in a digital image. The pressure from Eq. (2) is usually converted to a pressure coefficient according to the relation

$$c_{p,ij} = (P_{ij} - P_{\infty}) / Q, \quad (3)$$

where P_{∞} and Q are the freestream static and dynamic pressures, respectively.

*W. Ruyten and M. Sellers, "On-line Processing of Pressure-Sensitive Paint Images," *Journal of Aerospace Computing, Information, and Communication*, Vol. 1, September 2004, pp. 372-382. An earlier version was presented as AIAA Paper 2003-3947, 21st AIAA Applied Aerodynamics Conference, Orlando, Florida, June 23-26, 2003.

In intensity-based PSP tests, the signals $S^{(1)}$ and $S^{(2)}$ in Eq. (1) are the wind-off and wind-on signals. In lifetime-based PSP tests, both $S^{(1)}$ and $S^{(2)}$ are obtained at the run condition, but at different gates with respect to the excitation pulse train.

The calibration function $P(R, T)$ typically is cast in the form of a polynomial with fixed coefficients.^{3,8} Figure 1 shows an example of a set of calibration curves for the paint PtTFPP in FIB,⁹ which is produced by Innovative Scientific Solutions, Inc. and is the current industry standard for large-scale PSP testing in the U.S. Ideally, the temperature, T , in Eq. (2) would be provided on a per-pixel basis. In practice, a single, average value typically is supplied.

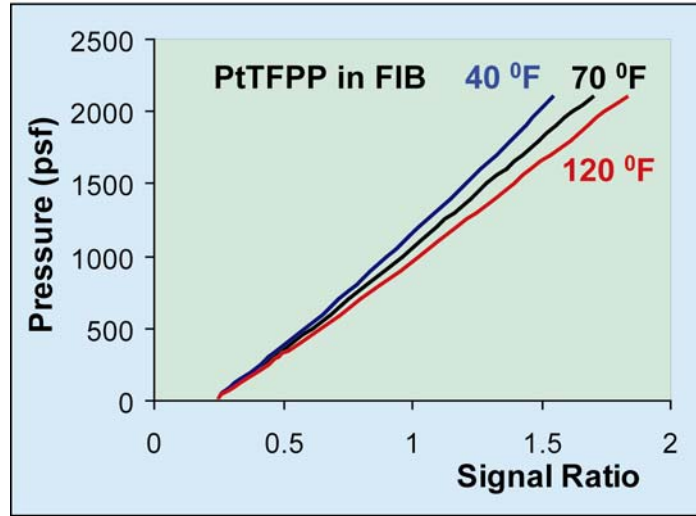


Figure 1. Example of PSP Calibration Curves

More complex implementations of PSP are possible—for example, those based on the use of bilumiphore paints (Refs. 10 and 11) or those based on multigate imaging.^{12,13} In such alternate schemes two signal ratios are defined, allowing the determination of either a temperature-corrected PSP measurement or a combined pressure and temperature measurement.

In the following paragraphs it is assumed that the paint response is given by Eq. (2) and that the calibration function, $P(R, T)$, has been determined prior to the wind tunnel test.

2.3.2 Image Mapping

To establish the mapping transformation between 2D image coordinates and 3D spatial coordinates on the surface of the test article, registration targets are applied to the test article. Let \mathbf{X}_n denote the 3D model coordinates of the target with index n , as determined by a coordinate-measuring machine. The resulting image coordinates, (x_n, y_n) , may be written symbolically as (see Section 4.5)^{14,15}:

$$(x_n, y_n) = F(\mathbf{X}_n; \mathbf{p}_c^*, \mathbf{q}_c, \mathbf{a}_m, \mathbf{t}), \quad (4)$$

where the function $F(\dots)$ represents a projective transform that takes as input the 3D model coordinates, \mathbf{X}_n , of the targets; the set of exterior parameters, \mathbf{p}_c^* , for camera c (representing the position and orientation of camera c with respect to the test facility); the set of interior parameters, \mathbf{q}_c , for the same camera (representing the effective focal length, optical center, and lens distortion parameters); a set of angles, \mathbf{a}_m , that describes the pitch and roll settings of the model-positioning system at a model attitude m ; and a fixed set of model alignment parameters, \mathbf{t} .

Before the function $F(\dots)$ can be determined for a given image, the image coordinates, (x_n, y_n) , of a sufficiently large set of targets must be obtained. This requires that the registration targets be located and

identified in the image (see Fig. 2). To do this automatically and efficiently has been the single biggest challenge in achieving on-line processing of PSP data. Aspects of this task are described in Refs. 16 through 18 and in Section 4.0 of this report.

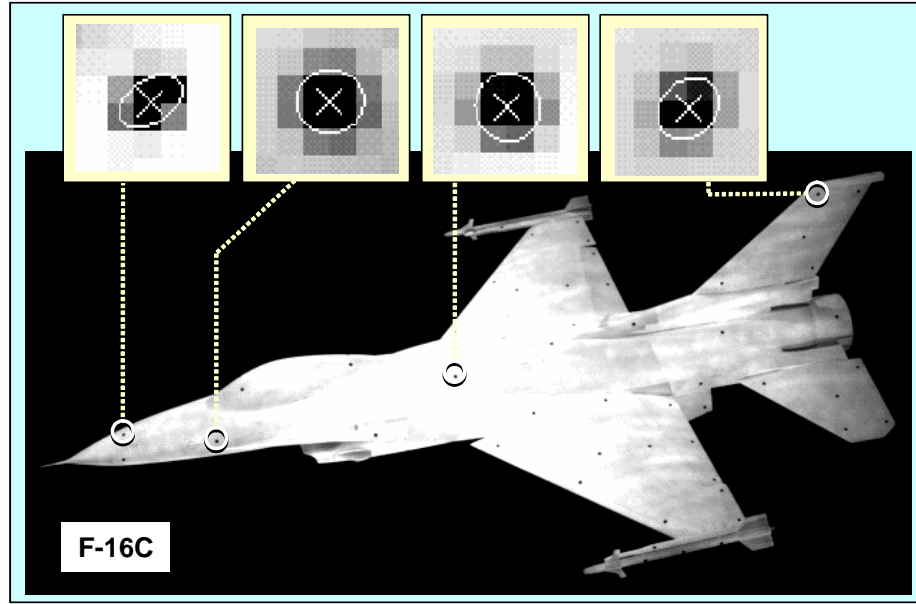


Figure 2. Example of PSP Image with Registration Targets

Once the mapping function, F , is known, it may be used to map image pixels to the predefined 3D grid of the test article. This typically involves the use of a z-buffer to preclude image data from being mapped to occluded parts of the 3D surface grid. So far, only multizone structured grids have been used as 3D grids, though the use of unstructured grids is under consideration.

A related image registration problem in intensity-based PSP is that of aligning a wind-on image to a wind-off image. If the misalignment between the two images is not too severe, the image coordinates in the second image may be related to the image coordinates in the first image by a polynomial transformation that may be written symbolically in terms of a function, G , as^{19,20}:

$$(x_n^{(2)}, y_n^{(2)}) = G(x_n^{(1)}, y_n^{(1)}). \quad (5)$$

2.3.3 Self-Illumination (SI) Correction

When emitted light from a low-pressure region on the surface of the test article (i.e., a region with relatively high signal) is emitted toward a high-pressure region (i.e., a region with relatively low signal) and is reflected toward the camera, the increased signal caused by the reflection process tends to lower the measured pressure. To a lesser extent, measured pressures in low-pressure regions are affected as well. It is possible to correct for these effects by approximating the painted surface as a diffuse reflector. The net emitted signal, S'_k , at a point, k , on the 3D grid can then be obtained from the measured signals, S_l , at other points, l , according to

$$S'_k = S_k - R_{\text{diff}} \sum_l A_{kl} S_l, \quad (6)$$

where R_{diff} is the reflectivity of the paint, A_{kl} is an influence coefficient that depends only on the geometry of the test article, and the summation is over that part of the surface with nonzero influence coefficients.²¹ Higher-order corrections, based on the use of a bidirectional reflection distribution function, are also possible.²²

The SI correction from Eq. (6) needs to be performed separately on both of the signal terms in Eq. (1). This implies that the image data must be mapped to the 3D grid before a signal ratio is calculated. In this regard, SI corrections require a deviation from the conventional data-processing sequence in which data from each camera are processed separately to a pressure distribution on the 3D grid.

The A-matrix from Eq. (6) can be precalculated, allowing the SI correction to be performed efficiently. Moreover, because the reflected light is, by assumption, diffusely distributed, the SI correction needs to be calculated explicitly only for a fraction of the grid points (10 percent, typically). The SI correction at the remaining points can then be obtained by interpolation.

2.4 PROCESSING SCHEMES

More than 70 macro commands are built into the original image-processing software (that is, the Green Boot code; see Section 2.6.1). The most important of these can be grouped into the following eight processing steps. (These eight reflect more closely the processing commands in the more recently developed software.)

DEFINE: Locate the required input data files on the basis of the to-be-processed run and sequence numbers, and generate the names of the resulting output files.

LOAD: Load data files into memory and perform one or more of the following: Subtract a black image (an “image” collected with the lens covered); divide by a flat-field image [an “image” collected without a lens on the camera, with the charge-coupled device (CCD) array exposed to a uniform light field]; scale the image by an exposure time or by the number of pulses over which the integration was performed; and/or apply a threshold value below which image data are considered to be indistinguishable from the background. Because of the use of image ratios in Eq. (1), flat-field corrections are usually not necessary.

REGISTER: Find (to subpixel precision) and identify all of the visible registration targets in the image and determine the resulting mapping transformation between 3D model coordinates and 2D image coordinates, as expressed by Eq. (4). Two tasks typically performed along with image registration are the calculation of the location of visible pressure taps (for use with in-situ calibrations) and the removal of registration targets and other artifacts by patch-interpolation.

ALIGN: Given the image coordinates of registration targets in a set of wind-off and wind-on images, determine the coefficients of the image alignment transformation from Eq. (5) and apply the transformation to align the two images. This alignment is only needed for intensity-based PSP measurements and is to compensate for the shift in model position that occurs as a result of sting deflection.

CONVERT: Calculate the ratio from Eq. (1), either between two images or between two sets of data on the same 3D grid. Set the result to “undefined” for points that do not have a valid value in both sets; then convert the ratios to pressure using Eq. (2), or to a pressure coefficient using Eq. (3). If an in-situ calibration is performed, the paint-derived pressure values are offset so as to achieve optimum agreement between the PSP values in the immediate vicinities of the pressure taps and the tap values themselves.

MAP: On the basis of Eq. (4), map 2D image data to the predefined 3D grid of the test article. To prevent mapping to occluded parts of the 3D grid, a z-buffer algorithm is used to determine visibility. If the same grid point is mapped by two or more cameras, the camera with the view most nearly normal to the surface is used or an average value is computed, as is described in Section 6.4.

SI-CORRECT: Perform the self-illumination correction from Eq. (6).

SAVE: Save intermediate or final data to the hard disk in 3D grid format. In addition to the pressure or pressure coefficient at every grid point, the saved file may contain additional values, such as the calculated uncertainties of the pressure data (See Section 6.5).

Figure 3 shows two processing sequences based on the eight processing steps above. Both sequences lead from two sets of raw image data (sets “1” and “2” in Fig. 3) to pressure coefficients on a 3D grid (set “3” in Fig. 3). The same steps are followed for both intensity-based and lifetime-based PSP. The primary difference between the two sequences is the point at which 2D image data are mapped to the 3D grid. In the second sequence, this mapping is performed prior to the conversion to pressure so that the SI correction from Eq. (6) can be performed. Alignment of the two sets of raw images is not needed in this case.

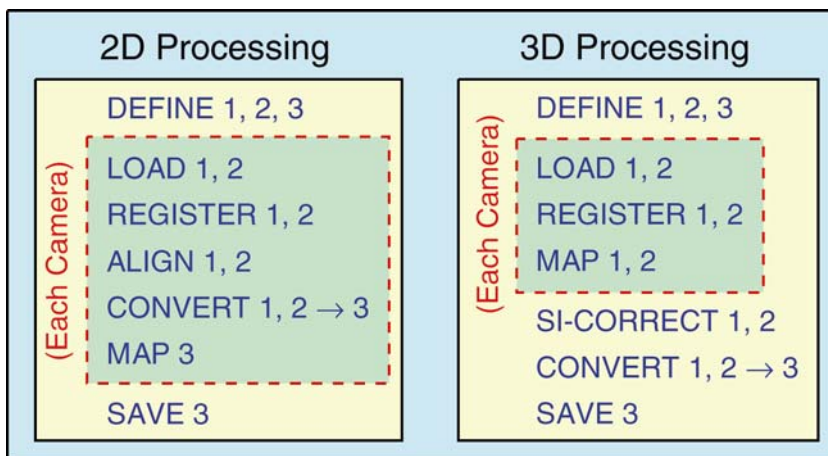


Figure 3. Basic Processing Sequences

Dashed lines are used in Fig. 3 to indicate which macros have to be performed for each of the eight cameras individually. This grouping of macros has implications for parallel processing, which is discussed in Section 2.6.3.

2.5 BENCHMARKS

Two data sets have been selected to serve as benchmarks for timing studies (see Table 1). These are small subsets from actual PSP tests on scale models of an F-16C fighter jet and NASA’s X-38 Crew Return Vehicle (see Fig. 4). Both tests were conducted in the 16-ft Transonic Wind Tunnel (16T) at AEDC, with eight cameras mounted in the test section, as shown in Fig. 5. (Only six cameras were used for the actual data reduction on the X-38.) In both tests, FIB-based paints were used (see Table 1) as the basis for an intensity-based measurement, while excitation of the PtTFPP fluorophore was accomplished with xenon arc lamps, which were filtered between 350 and 550 nm.

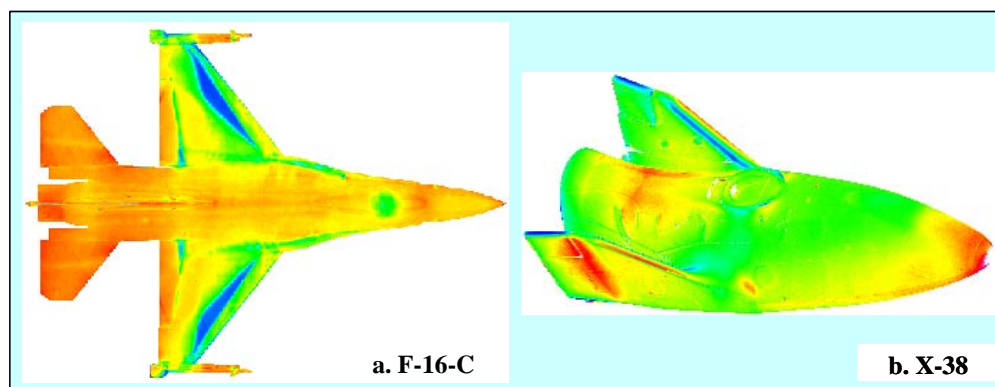


Figure 4. Examples of Processed Data for the Two Benchmark Cases

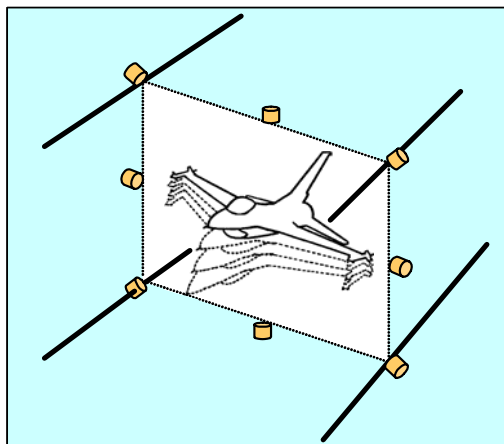


Figure 5. Schematic of Wind Tunnel Setup with Positions of the Eight Cameras Shown

In both benchmarks, four images are used per camera per data point (wind off and wind on, each with associated black images). Image sizes are 1024 by 1024 pixels, with 16-bit resolution per pixel. Both benchmarks contain four model attitudes, taken from an alpha sweep. The 3D geometry files for both tests are multizone, structured, Plot 3D grids with over 300,000 grid points each. In both cases, self-illumination corrections were performed at about 1/10 of this resolution, with about 30,000 cells per calculation. Further details are given in Table 1. Figure 6 shows an example of the effect of the SI correction on the X-38.

Table 1. Benchmark Data Sets

	F-16C (tf960)	X-38 (tf976)
Number of Data Points	4 ($\alpha = 0, 8, 18, 26$ deg)	4 ($\alpha = 4, 8, 16, 20$ deg)
Mach Number	0.8	0.6
Number of Cameras	8	6
Paint	PtTFPP in FIB7	PtTFPP in UniFIB
Images per Camera per Point	4	4
Image Size	1024×1024×16 bit	1024×1024×16 bit
Number of Registration Targets	102	36
Number of Pressure Taps	400	118
Number of Zones per Grid	379	264
Number of Points on 3D Grid	344,269	311,726
Number of Elements in A-Matrix	29,172	31,344
Size of A-Matrix File	230 MBytes	129 MBytes

2.6 SOFTWARE AND HARDWARE

2.6.1 Software

Since 1998, PSP data processing at AEDC has been accomplished with “Green Boot,” a program that was developed in the mid 1990s by McDonnell Douglas Aerospace (MDA) and NASA Ames. Since the program was acquired by AEDC, NASA Ames and AEDC have continued development of a government version of the code, while Boeing (upon acquiring MDA) has continued development of a proprietary version. The government version of the code (currently, Version Gb.2.17a) consists of about 92,000 lines of code, programmed 88 percent in C and 12 percent in Fortran. The program has an

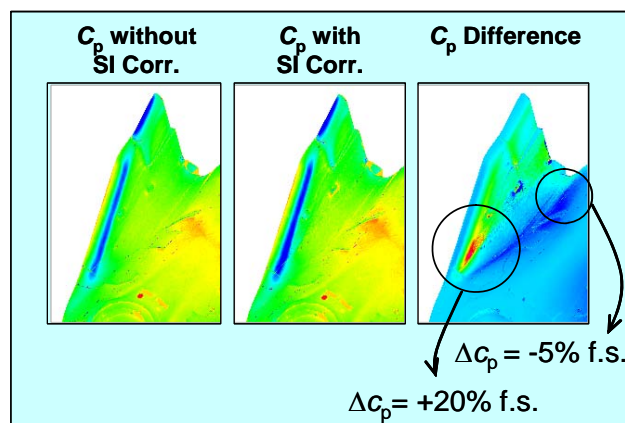


Figure 6. Illustration of Effect of Self-Illumination Correction on X-38 Tail Section

extensive graphical user interface (GUI) but also supports script-based processing. The program runs on either SGI Irix or Linux platforms. The program structure is essentially sequential, though some modifications have been made to support parallel processing, as described in Section 2.6.3.

Table 2 lists the principal support files for the Green Boot program. The SQL database file keeps track of all raw and processed images associated with a particular test, as well as associated parameters such as tunnel conditions and mapping coefficients. The targets file contains model coordinates, normal vectors, and (when applicable) diameters of each of the targets and pressure taps, as well as other points (“fiducials”) that need to be located in the image but that are not used for image registration. The camera file stores parameters that are required to accomplish automatic image registration. The setup file contains various program settings and maintains a list of most-recent commands. The wind tunnel data (WTD) files report tunnel conditions and aerodynamic coefficients, as well as pressure readings from pressure taps, if any, to be used for in-situ calibrations. The 3D grid file defines the geometry of the test article. The component file defines groupings of zones for load calculations on parts of the model (e.g., left upper wing, left lower wing, fuselage, etc.). The A-matrix file contains the precalculated SI coefficients from Eq. (6). Macro files define processing sequences such as those in Fig. 3. The log file and diagnostics files maintain a record of submitted inputs and outputs generated by the program.

Table 2. Support Files for Data Processing

	Input	Output	Calibration
SQL Database File	✓	✓	
Targets File	✓		
Camera File	✓		✓
Setup File	✓	✓	✓
WTD Files	✓		
3D Grid File	✓		
Component File	✓		
A-Matrix File	✓		
Macro Files	✓		
Log File		✓	
Diagnostics Files		✓	

Table 2 indicates whether the files are used for input, output, or both, and whether the files are used as part of the manual pretest calibration process, which has to be completed before fully automated processing can be accomplished in run mode.

2.6.2 Hardware

The Green Boot code has been run on a variety of Silicon Graphics workstations, from the now-obsolete Indigo 2 and O2, through the Origin 2000, the Octane, and Octane 2, with processors ranging from an IP22, R4400 for the Indigo 2 to a dual IP 30, R14000 for the Octane 2, and at processing speeds ranging from 195 MHz for the Indigo 2 to 600 MHz for the Octane 2.

Until recently, all PSP data acquisition (along with a large part of the data processing) was performed on an SGI Origin 2000, equipped with 1.3 GB of memory and with eight IP27, R10000 processors running at the (now slow) speed of 195 MHz.

Most recently, the Green Boot code has been transitioned to a Linux cluster. This system is configured to allow simultaneous data acquisition and data processing. It consists of a set of front-end, dual P4, Xeon processors running at 2.4 GHz and eight dual-processor slaves (also P4 Xeon), each running at 2.2 GHz. Communication between the master and the slaves is through an HP switch with a 1-Gbit Ethernet connection to the front end and 100-Mbit connections to each of the nodes. The front end has 2 GB of memory, while the nodes have 1 GB each. Both the master and the slaves run Linux Red Hat 7.3 as the operating system.

2.6.3 Implementation

Various configurations of the software have been employed, ranging from purely sequential processing (i.e., one camera at a time) to parallel processing, as shown in Fig. 7. The implementation shown in Fig. 7 is the latest and fastest, especially if a separate processor is available for each of the processes shown (i.e., one master process and up to eight slave processes).

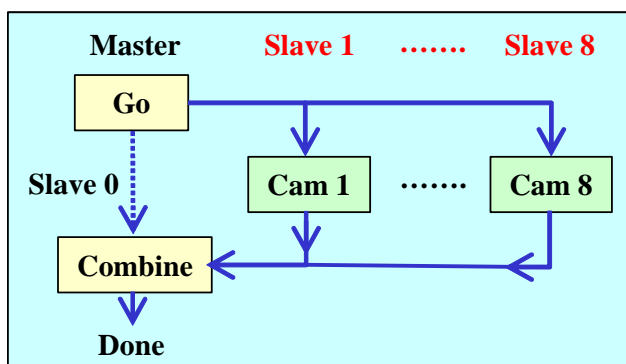


Figure 7. Parallel-Processing Implementation for the Processing Schemes from Figure 2.3

The implementation from Fig. 7 applies to both processing sequences from Fig. 3. In each case, macros in the dashed boxes in Fig. 3 are performed in parallel for each camera individually. Upon completion, partially processed data from all cameras are combined and processed to final data on the 3D grid.

Because the Green Boot code is not intrinsically parallel in nature, communication between the master process and the slave processes in Fig. 7 is accomplished via pipes and sockets (see Section 3): The master sends out a start signal by writing a run and sequence number into a signal file that is monitored continuously by the slave processes. At this point, the master process itself becomes a slave, waiting for a completion signal (as well as partially processed data) from each of the original slave processes, and also via the hard disk.

The newer software program (the so-called BlackBox code) accomplishes the same tasks by use of the Parallel Virtual Machine (PVM) paradigm. This newer program achieves greater efficiency for on-line processing by allowing more efficient data sharing between processors and by implementing only that functionality of the GreenBoot code that is essential for on-line processing per se (i.e., without implementing the substantial requirements for GUI support, pretest calibration functions, and posttest interrogation of the processed data).

2.7 TIMING RESULTS

Benchmark results for the data from Section 2.5 are presented in Tables 3 and 4. In these tables, the designations “2D” and “3D” refer to the processing schemes from Fig. 3. In each case, the highest possible optimization settings were used at compile time, i.e., the “-O3 -r12000” flags on the SGI machines and the “-O” flag on the Linux machines.

Table 3. Cumulative Single-Processor Times (in Seconds) for X-38 Data on SGI Octane 2

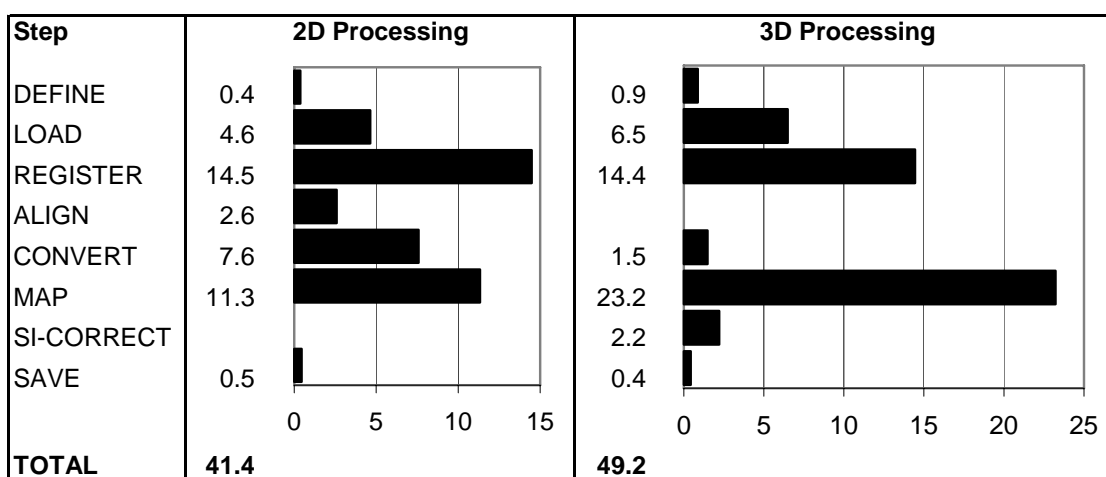


Table 4. Processing Times per Data Point in Seconds

	SGI Origin 2000 (8 Proc, 195 MHz)		SGI Octane 2 (2 Proc, 600 MHz)		Linux Cluster (9 Dual Proc, 2.2 GHz)	
	F-16C	X-38	F-16C	X-38	F-16C	X-38
2D, Seq	150	103	60	39	32	22
3D, Seq	193	121	74	48	41	28
2D, Par	27	22	30	22	7	6
3D, Par	41	31	38	28	10	8

Table 3 shows average processing times per processing step for the X-38 dataset on the SGI Indigo 2, when only a single processor was used. It is seen that the most time-consuming processing steps are image registration and mapping data to the 3D grid. Mapping times in the 3D case are twice those in the 2D case, which is consistent with the fact that twice as many images have to be mapped (i.e., wind-off and wind-on intensities, as opposed to pressure values).

Table 4 lists total processing times per data point for both the F-16C and X-38 datasets. Times are grouped by machine, by processing type (2D vs. 3D—see Fig. 3), and by sequential (“seq”) vs. parallel (“par”) processing. In the sequential case, only one processor is used per machine. This results in longer

times for the F-16C data than for the X-38 data, because of the use of eight cameras versus six. In the parallel case, either eight, two, or nine processors are used, as indicated by machine type. Times for the F-16C and X-38 are closer in this case. Most importantly, parallel processing times on the fastest machine (the Linux cluster) are well below 15 s per data point. This time (15 s) was the target for achieving on-line processing, in the sense that at this speed, one data point can be processed in full while the next data point is being acquired.

2.8 CONCLUDING REMARKS

With the implementation of parallel processing of PSP image data on a Linux cluster, a significant milestone was achieved—namely, the ability to reduce processing times sufficiently that one data point can be processed in full while the next data point is being acquired. Further improvements have been made, particularly the PVM-based program that enables more efficient sharing of data among multiple processors than was previously feasible with the Green Boot code.

The processing schemes employed can easily be extended to more general PSP measurements—for example, those that would employ a third (and possibly a fourth) gate for simultaneous measurement of pressure and temperature,¹⁰⁻¹³ or for a temperature-corrected PSP measurement.

Further reductions in data-processing times (with processing times moving below one second per data point) are probably not required for the study of steady-state flows. However, it is conceivable that further speed increases might become desirable for the study of unsteady flow phenomena such as buffet, flutter, limit-cycle oscillations, and other dynamic pressure phenomena. Such further improvements in data-processing times would probably call for both hardware and software improvements beyond those described here, or would use two-tier processing, with approximate data being generated in near-real time. More accurate processing would then be performed after the completion of the wind tunnel test.

3.0 MESSAGE PASSING FOR PARALLEL PROCESSING OF PRESSURE-SENSITIVE PAINT IMAGES[†]

3.1 ABSTRACT

A message-passing scheme is described that allows parallel processing of pressure-sensitive paint images on a machine with multiple processors or a cluster with multiple nodes. The scheme implements the use of forks and pipes in the former case and socket-based TCP/IP communications in the latter. The approach demonstrates how multiple copies of a nonparallel legacy code (in this case, NASA's Green Boot software) can be made to run in parallel in either a parent-child or a client-server configuration. Results are presented for benchmark data from wind tunnel tests of an F-16C fighter jet model and NASA's X-38 Crew Return Vehicle.

3.2 INTRODUCTION

Pressure-sensitive paint (PSP) has established itself as an important test and evaluation tool for measuring full-field pressure distributions on test articles in aerodynamic test facilities, particularly transonic wind tunnels.¹ At the AEDC, these pressure distributions are obtained by processing image data from up to eight digital cameras in the test section of the wind tunnel (see Fig. 5). Final data are presented to the customer on a three-dimensional (3D) grid of the test article. Processing steps include automatic target detection, image registration, image alignment, reflected-light correction, conversion of signal ratios to pressure, and mapping of image data to the 3D grid.^{23,24}

Data processing is accomplished with Green Boot, a code that was developed originally by NASA Ames Research Center and McDonnell Douglas Aerospace (MDA). The code consists of some 90,000 lines of C (with some Fortran), offers extensive graphical user interface (GUI) support, and has provisions for script-based processing. It has always been possible to run multiple copies of the code as separate processes. However, management of the required databases and script files has proven to be cumbersome and an impediment to achieving automated processing in near-real time (i.e., within 15 s of taking data).

3.3 PARALLELIZATION APPROACH

Figure 8 illustrates how data-processing requirements naturally suggest a master-slave implementation of parallel processing PSP image data: a master process initiates a request to process a data point, whereupon up to eight slave processes (one for each camera) perform partial processing of image data from a particular camera—the result being processed data that are mapped to the 3D grid. The master process then collects this mapped data from the slaves, merges the data onto a single 3D grid, and completes processing of the data. These steps are described in detail in Ref. 24. The present section focuses on the message-passing scheme that was developed to implement this concept.

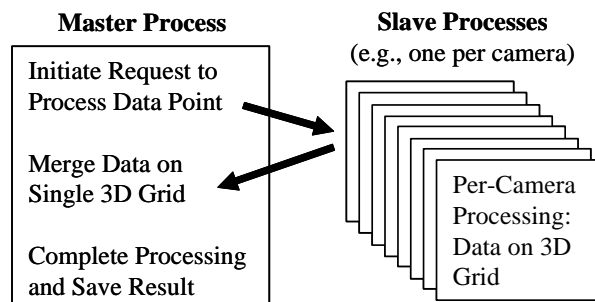


Figure 8. Master-Slave Approach to PSP Data Processing

[†]W. Ruyten and W. E. Sisson, "Message Passing for Parallel Processing of Pressure-Sensitive Paint Images," DoD HPCMP Users Group Conference, Williamsburg, Virginia, June 7-11, 2004. (Also published by IEEE in bound Proceedings, ISBN 0-7695-2259-9, pp. 308-312).

Figure 9 lists a typical macro that is executed by the master process: It defines the names of the to-be-processed images and the final 3D data file on the basis of run and sequence numbers of the data points. It then instructs each of the slave processes in Fig. 8 to execute the script `slave_macro` for a particular camera, merges the returned data onto the 3D grid, and saves the final result in Plot-3D (or other) format. The `INSTRUCT` and `MERGE_3D` commands are built into the Green Boot code, whereas `_define` and `_save` are script files that are defined by the user in terms of native Green Boot commands. The variable `$P3D` is set by the script `_define`.

In Figure 9, the instruction “`INSTRUCT $CAM ...`” causes the script “`slave_macro $1 $2 $CAM`” to be executed on the slave process assigned to camera `$CAM`. (Here, `$1` and `$2` represent the run and sequence numbers of the data point.) Figure 10 lists a typical realization of `slave_macro`. It loads the reference and run images from the specified camera; finds the registration targets; registers the images by determining the mapping transformation from 2D image space to 3D model space; aligns the two images (to account for small rotations and/or shifts between the two); ratios the images; converts the ratio to a pressure or pressure coefficient (based on a calibration equation); maps the resulting pressure to the 3D grid; and sends this information back to the master process. The variables `$REF`, `$RUN`, and `$P3DCAM` in Fig. 10 are each set by the script “`_define`.” All scripts prefaced with an underscore are defined by the user.

The processing sequences from Figs. 9 and 10 can be used both with intensity-based PSP (in which a reference image is obtained with the tunnel at atmosphere) and with lifetime-based PSP, in which both the reference and the run images are obtained at the run condition. Variations on these scripts are possible. For example, in order to perform a correction for reflected fluorescent light, the reference and run images both have to be fully mapped to the 3D grid before conversion to pressure can take place. In this case, the master macro performs `MERGE_3D` on two sets of images, performs the reflected-light correction, and only then performs the `_convert` macro before saving the final result.

```
_define $1 $2                                // $1, $2 define data point
foreach CAM (01 02 ... 08)                  // Loop over all cameras
  INSTRUCT $CAM slave_macro $1 $2 $CAM      // Process $CAM on Slave $CAM
end                                           // End of loop
MERGE_3D $P3D                               // Combine data on 3D grid
_save $P3D                                 // Save final result
```

Figure 9. Typical Master Macro Script

```
_define $1 $2 $3                            // $1, $2, $3 define data point, camera
_load $REF $3                               // Load reference image (e.g., wind-off)
_load $RUN $3                               // Load run image (e.g., wind-on)
_register $REF                             // Find targets and register ref image
_register $RUN                             // Find targets and register run image
_align $RUN $REF                           // Align the run image to the ref image
_convert $RUN $REF                         // Ratio images and convert to pressure
_map $RUN $P3DCAM                         // Map pressure data to 3D grid for this camera
_send $P3DCAM                             // Send result back to master process
```

Figure 10. Typical Realization of `slave_macro` in Figure 3.2

3.4 IMPLEMENTATION

The master-slave communications scheme from Fig. 8 has been implemented in two ways. In the first approach, the master process is forked repeatedly before X-window support is requested, and write and read pipes are established from the parent process (the master) to the resulting child processes (the slaves). In the second approach, slave processes are started up in server mode on one or more host

machines at preselected ports, and the master process acts as a client that requests a socket-based TCP/IP connection to each slave.²⁵ In both cases, a set of file descriptors is established on each process (`fdw[]` for writing, `fdr[]` for reading), as illustrated in Fig. 11. This allows the program to communicate between processes by performing system-defined `WRITE` and `READ` calls on these file descriptors, as illustrated in Fig. 12 for a set of data contained in a buffer, `buf`. The `while` loop in Fig. 12 ensures that data packets are received in full, even if more than one set of write/read operations is required. Typically, 0.9 to 1.4 MB of data are returned to the master process per slave process per data point. These data are buffered in packets of up to 10,000 bytes, a size that appears to work well for both the pipe and the socket implementations.

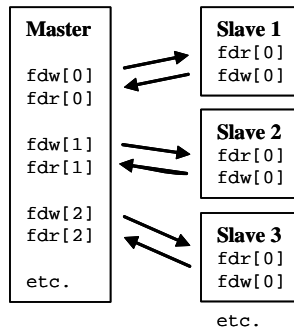


Figure 11. Implementation of Master-Slave Communication Through File Descriptors

```

int len = sizeof(buf);                // Length of data in buf
write(fdw[0], &len, sizeof(len));      // Write length of data
write(fdw[0], buf, len);               // Write data

int len, nr=0;                        // Initialize num bytes read
read(fdr[s], &len, sizeof(len));       // Read length of data from "s"
while(nr!=len)                        // Loop until all data read
    nr+=read(fdr[s], &buf[nr], len-nr); // Read data from slave "s"

```

Figure 12. Interprocess Communication via System-Level `WRITE` and `READ` Calls

Figures 13 and 14 show partial source code for the establishment of the file descriptors in the two scenarios. The fork/pipe implementation in Fig. 13 is straightforward and requires separate pipes for writing and reading. The socket implementation from Fig. 14 is somewhat more involved, but it allows both reading and writing on a single socket. Byte swapping, if required, is performed by the master process only. (For example, in Fig. 12, the variable `len` would be byte-swapped prior to the first write operation.)

```

for (int s=0; s<N; s++) {              // Request N slave processes
    int MS[2], SM[2], pid;
    if (pipe(MS)<0 || pipe(SM)<0) error... // Create the pipes
    if ((pid=fork())<0) error...          // Fork the main process
    if (pid==0) {                        // Parent process (master)
        fdw[s]=MS[1]; close(MS[0]);      // Set file descriptors
        fdr[s]=SM[0]; close(SM[1]);
        continue;
    }
    else if (pid>0) {                    // Child process (slave)
        fdw[0]=SM[1]; close(SM[0]);      // Set file descriptors
        fdr[0]=MS[0]; close(MS[1]);
        (enter slave mode...)            // Indefinite loop
    }
}

```

Figure 13. Fork-Pipe Implementation with Master and Slave Processes

```

Start slave process in server mode:
struct sockaddr_in sock;  int fd;
(populate sock: AF_INET, port number, INADDR_ANY)           // Specify port
int fd_tmp = socket(AF_INET,SOCK_STREAM,IPPROTO_TCP);        // TCP-IP socket
if (bind(fd_tmp,&sock,sizeof(sock))<0) error...
if (listen(fd_tmp,MAXQUEUE)<0) error...                      // Set queue size
if ((fd=accept(fd_tmp,NULL,NULL))<0) error...               // Connect client
fdr[0]=fdw[0]=fd; close(fd_tmp);                            // File descriptors
(enter monitoring mode...)

Start master process as client to slave s:
struct sockaddr_in sock; struct hostent *host;
if ((host=gethostbyname(hostname))!=NULL) error...          // Specify host
(populate sock: AF_INET, port number, host->h_addr)          // Specify port
int fd = socket(AF_INET,SOCK_STREAM,IPPROTO_TCP);            // TCP-IP socket
if (connect(fd,&sock,sizeof(sock))<0) error...              // Connect server
fdr[s]=fdw[s]=fd;                                           // File descriptors
(continue with main program...)

```

Figure 14. TCP/IP Implementation with Master and Slave Processes

The fork/pipe approach is particularly suited to a single machine with multiple processors, such as an SGI architecture. It has the advantage that the resulting slave processes are tied directly to the master process, so that separate management of the slave processes is not required. The socket approach is intended for use on a cluster of machines in which multiple processors communicate via an Ethernet connection. In this case, one must exercise care to ensure that the slave processes are running and communicating when the master requests that a data point be processed. In either case, the resulting scheme is much more robust than the one that was used in the prototype version described in Ref. 3, which relied on the use of instruction files that were written to and read from a common file system. In particular, conflicts that arose when one process was trying to read from the file system while another was in the process of writing to it (or vice versa) are avoided with both the fork/pipe and socket approaches, which perform buffering and synchronization of read and write operations implicitly. Master and slave processes still access a common database for tracking information related to the raw and processed image data. This is a commercially available SQL database designed specifically to synchronize access by multiple processes.

To facilitate management of the slave processes on a cluster, a Green-Boot-specific daemon process is registered on each node of the cluster under the super-daemon `inetd`.²⁵ This allows a Green Boot slave process to be started, polled, and shut down remotely from the node on which the master process is executed (typically, the front end of the cluster).

Some further details on the operational modes of the improved Green Boot code are presented in Section 3.6.

3.5 RESULTS

Correct functioning of the code was verified on several platforms, including an SGI Octane 2 (with dual IP30, R14000 processors running at 600 MHz), an older SGI Origin 2000 (with eight IP27, R10000 processors running at 195 MHz), and a Linux cluster consisting of a front end and eight nodes. The Linux cluster (running Red Hat Linux 7.3) is powered by dual P4 Xeon processors on both the front end and the nodes, running at 2.4 GHz and 2.2 GHz, respectively. Communication between the front end and the nodes is through an HP switch with a 1-Gbit/s Ethernet connection to the front end and 100-Mbit/s connections to each of the nodes. Measured transfer rates on the cluster (with one master process and eight slave processes on the nodes) exceed 80 Mbit/s.

When the code was run on a single multiprocessor machine, no significant difference in total processing time was found between the fork/pipe and socket implementations. This is consistent with the fact that interprocess communication requires far less CPU time than does the actual processing of the data. As expected, best performance was obtained on the Linux cluster, which has the highest processing speed among the platforms tested. Total processing times per data point for two benchmark datasets (involving an F-16C fighter jet and NASA's X-38 Crew Return Vehicle) are detailed in Section 2.7 and in Ref. 24 for the three machines quoted above, and are shown in Table 5, for both "2D" processing (without a reflected-light correction) and "3D" processing (with a reflected-light correction). In the F-16C case, image data from eight cameras were processed on a master process supported by eight slave processes; for the X-38 case, image data from six cameras were processed on a master process supported by six slaves. In both cases, four 1024×1024×16-bit images are used for each camera (wind-off and wind-on images, each with an associated black image that is subtracted as part of the `_load` macro in Fig. 10), and final data are mapped onto a 3D grid with more than 300,000 grid points. Figure 4 shows sample results for the two benchmarks, with color representing the value of the measured pressure. (Red represents high pressure; blue represents low pressure.)

From a performance perspective, the results in Table 5 are particularly significant in that a single data point can be processed in well under 15 s on the Linux cluster. This was the AEDC goal for achieving near-real-time processing of PSP test data.

Table 5. Parallel Processing Times per Data Point in Seconds

	SGI Origin 2000 (8 Proc, 195 MHz)		SGI Octane 2 (2 Proc, 600 MHz)		Linux Cluster (1+8 Proc, 2.2 GHz)	
	F-16C	X-38	F-16C	X-38	F-16C	X-38
2D (w/o refl)	27	22	30	22	7	6
3D (w/ refl)	41	31	38	28	10	8

3.6 CONCLUSION

It has been successfully demonstrated that it is possible to parallelize an intrinsically nonparallel legacy code, particularly one that lends itself to a master-slave configuration in which the master process initiates a request to process a data point, slave processes perform partial processing of the data, and the master process completes processing of the data after combining the results from the slaves. Communication between the master and the slaves can be accomplished either across pipes by repeatedly forking the main process (on a multiprocessor machine) or (on a cluster) by establishing socket-based TCP/IP communications between master and slaves, with each slave running as a server process on a node, and the master process running as a single client on the front end of the cluster. This approach to parallelization may be applicable to data processing schemes other than those used here for pressure-sensitive paint.

3.7 APPENDIX 3A: GREEN BOOT RUN MODES

The improved Green Boot code can be run in four modes, depending on the presence of an optional master-slave argument on the command line:

(1) "\$PATH/gb config": Start a single process on the specified configuration files (i.e., a collection of data files with different extensions, each of which has "config" as the root name of the file. (This is the original Green Boot mode.)

(2) "\$PATH/gb config -forkN": Start a master process that will fork N slave processes. The slaves are terminated upon exiting the master process.

(3) “\$PATH/gb config –portP &”: Start (in background mode) a slave process that will, upon being contacted by a master client process, establish a TCP/IP connection to the master process on (slave) port number P. This command can be performed either manually on the machine upon which the slave process is to be run, or automatically, as the slave process can be spawned by the `inetd` super server, when the super server receives a remote request from the master process. The slave process is terminated when the server receives the built-in Green Boot command “QUIT” from the master process.

(4) “\$PATH/gb config -serv”: Start a master process that will request that a series of slave processes be spawned remotely, depending on the contents of a setup file. The setup file contains, for each camera, the hostname and port number of the node that is to run a slave process for that camera in server mode, as well as the paths to the database files and the Green Boot executable on the node. When the master process is able to verify that all the slaves are in listening mode (see Fig. 14), the socket connections are established. When the user exits the master process, the master sends a QUIT command to each of the slave processes.

3.8 ACKNOWLEDGMENTS

The Linux cluster was purchased with funds provided by the High-Performance Computing Modernization Program Office.

4.0 AUTOMATIC IMAGE REGISTRATION FOR OPTICAL TECHNIQUES IN AERODYNAMIC TEST FACILITIES[‡]

4.1 OVERVIEW

A mathematical model is described for automatic registration of digital images of sting-mounted test articles in aerodynamic test facilities. The model is based on three premises: the use of registration targets on the test article; approximate knowledge of the attitude angles of the test article with respect to the test facility at each measurement point; and the ability to calibrate the cameras with respect to the test facility. Registration of individual images proceeds in three steps: first, initial predictions are calculated for the image coordinates of all visible registration targets; then template-based searches are performed to locate the targets to subpixel accuracy; finally, an exact mapping between 2D image coordinates and 3D model coordinates is established. The math model includes deflection of the sting under air loads. Sample results are presented for several windtunnel tests.

4.2 INTRODUCTION

A variety of optical techniques are used to study aerodynamic flows in test facilities and their effects on vehicle performance. These techniques include pressure- and temperature-sensitive paints (PSP, TSP), optical model deformation measurement, particle-imaging velocimetry (PIV), Doppler global velocimetry (DGV), laser-induced fluorescence (LIF), and others (see any of the proceedings of the International Congress on Instrumentation in Aerospace Simulation Facilities, e.g., Ref. 13). A common challenge for these optical techniques is to establish the correspondence between 2D image coordinates and the corresponding coordinates in 3D space. For example, in the case of PSP, it is customary to map measured pressures to a 3D grid of the test article.¹

Photogrammetry is a well-established technique used to determine the required mapping transformations between 2D image coordinates and 3D spatial coordinates and is based on the use of registration targets.^{14,15,20,26-28} The 3D coordinates of these targets are measured before the test, for example, using a coordinate-measuring machine. The challenge, then, is to locate these targets in the hundreds or thousands of images that are acquired as part of the diagnostic employed, while the test article is moved about the test facility. The purpose of Section 4.0 is to describe a scheme that has been developed at the Arnold Engineering Development Center (AEDC) to automate this image registration process for digital images of sting-mounted test articles. Parts of this image registration scheme have been described elsewhere, including the use of photogrammetry,^{15,28} the initial predictions of target location in images,^{15,16} the use of template-based searches to determine the actual target locations in an image to subpixel accuracy (see Section 5.0),^{17,29} and the resulting capability to perform on-line processing of luminescent-paint data (see Section 2.0).²⁴ The purpose of Section 4.0 is to address those aspects that pertain to image registration per se in a comprehensive fashion, and to document several aspects of this process that are not covered in prior publications or in other sections of the present report. These are the use of a sting deflection model to deal with the displacement of a test article caused by bending of the sting under the effect of air loads in a wind tunnel (Section 4.4); the implementation of the template-based search scheme (Section 4.6); aspects of the resulting image registration algorithm (Section 4.8); and selected results (Section 4.9). First, the use of photogrammetry is reviewed in Section 4.3.

4.3 REVIEW OF PHOTOGRAMMETRY

In its most basic form, imaging by a camera is described as a projective transform, whereby the spatial coordinates x_i^* of a target i give rise to a pair of image coordinates (u_i, v_i) , given by (see Fig. 15):

[‡]W. Ruyten, "Automatic Image Registration for Optical Techniques in Aerodynamic Test Facilities," AIAA Paper 2004-2400, 24th AIAA Aerodynamic Measurement Technology and Ground Testing Conference, Portland, Oregon, June 28-July 1, 2004 (outstanding paper award).

$$u_i^{(0)} = u_c - f_c \frac{U_i}{W_i}, \quad v_i^{(0)} = v_c - f_c \frac{V_i}{W_i}. \quad (7)$$

Here u_c and v_c denote the image coordinates of the optical axis of the camera, f_c is the effective focal length of the camera, and U_i , V_i , and W_i are the components of a vector, U_i , that is given by

$$\mathbf{U}_i = \mathbf{R}_c^* (\mathbf{x}_i^* - \mathbf{x}_c^*). \quad (8)$$

The vector \mathbf{x}_c^* and matrix \mathbf{R}_c^* denote the position and orientation of the camera and may be expressed as

$$\mathbf{x}_c^* = (x_c^*, y_c^*, z_c^*), \quad \mathbf{R}_c^* = \mathbf{R}_c^*(\phi_c^*, \kappa_c^*, \omega_c^*). \quad (9)$$

As indicated, the orientation matrix \mathbf{R}_c^* depends on three Euler angles. The exact choice of angles is not of particular importance (see, e.g., Refs. 14 or 15) so long as the rows of the matrix \mathbf{R}_c^* correspond to an orthonormal set of vectors $\{u_c^*, v_c^*, w_c^*\}$ in 3D space that defines the orientation of the image plane and the viewing direction of the camera. As indicated in Fig. 15, the convention followed here is that the origin of the image coordinate system is in the bottom left corner of the image. Alternatively, the image origin might be defined as being in the upper left-hand corner, which would require a reversal of the directions of the vectors v_c^* and w_c^* (see Fig. 1 of Ref. 15).

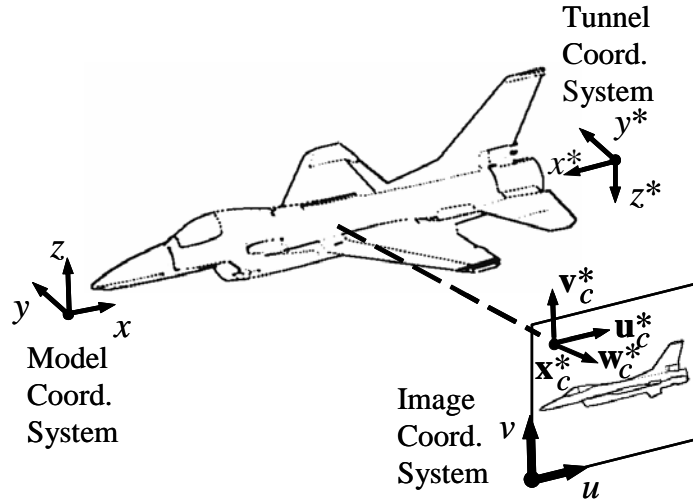


Figure 15. Schematic of Imaging Process

The superscripts “(0)” in Eq. (7) indicate that deviations from perfect imaging are not yet included. For example, radial lens distortion (quantified by a factor K_{1c}) produces distorted image coordinates that are given in terms of the undistorted coordinates from Eq. (7) by

$$u_i = u_i^{(0)} - \delta_{ui}, \quad v_i = v_i^{(0)} - \delta_{vi}, \quad (10)$$

where

$$\delta_{ui} = K_{1c} \Delta_{ui} (\Delta_{ui}^2 + \Delta_{vi}^2), \quad \delta_{vi} = K_{1c} \Delta_{vi} (\Delta_{ui}^2 + \Delta_{vi}^2), \quad (11)$$

and

$$\Delta_{ui} = u_i^{(0)} - u_c, \quad \Delta_{vi} = v_i^{(0)} - v_c. \quad (12)$$

Higher order distortion terms can be included as well.¹⁴

The reason for the use of asterisks in Eqs. (8) and (9) is to distinguish tunnel coordinates (*with* asterisks) from the corresponding model coordinates, denoted *without* asterisks. Tunnel coordinates are measured with respect to the test *facility*; model coordinates are measured with respect to the test *article*. Model coordinates of registration targets, denoted \mathbf{x}_i , are initially known only with respect to the model coordinate system. In Section 4.4, the task is undertaken to estimate the corresponding tunnel coordinates \mathbf{x}_i^* as the test article is moved about the test facility. Assuming that both the exterior parameters (x_c^* , y_c^* , z_c^* , ϕ_c^* , κ_c^* , ω_c^*) and the interior parameters (f_c , u_c , v_c , K_{1c}) of the camera have been calibrated, it is then possible to estimate the resulting image coordinates (u_i , v_i) of visible registration targets (Section 4.5); to find the exact locations of the targets using template-based correlation matching (Section 4.6); and to complete the image registration process (Sections 4.7 and 4.8).

4.4 STING MODEL

Neglecting effects of model deformation, the relation between the model coordinates \mathbf{x}_i of a registration target and its corresponding tunnel coordinates \mathbf{x}_i^* may be written as

$$\mathbf{x}_i^* = \mathbf{x}_k^* + \mathbf{R}_k^* \mathbf{x}_i, \quad (13)$$

where \mathbf{x}_k^* and \mathbf{R}_k^* denote the position and orientation of the test article at an attitude setting k , in terms of three position values, x_k^* , y_k^* , z_k^* and three Euler angles, α_k^* , β_k^* , ϕ_k^* according to

$$\mathbf{x}_k^* = (x_k^*, y_k^*, z_k^*), \quad \mathbf{R}_k^* = \mathbf{R}_k^*(\alpha_k^*, \beta_k^*, \phi_k^*). \quad (14)$$

As is the case in Eq. (9), different definitions of the pitch, yaw, and roll angles (i.e., α_k^* , β_k^* , and ϕ_k^*) are possible (see, e.g., Ref. 30).

For a pitch-roll mechanism such as that in AEDC's transonic wind tunnel, the calculation of \mathbf{x}_k^* and \mathbf{R}_k^* is described in Ref. 15 for the case of no-sting deflection under air loads. To incorporate such sting deflection, the assumption is made that the sting deforms into a circular arc in the pitch plane of the model. This situation is depicted (in exaggerated fashion) in Fig. 16 for the case of zero model yaw, zero model roll, and zero prebend angle (i.e., the x -axis of the model is aligned with the sting). In this case, the sting deflection angle is given by $\Delta\alpha_S = \alpha - \alpha_S$, where α and α_S are the pitch angles of the model and the sting, respectively, as reported by the wind-tunnel data system. Based on the assumption of a circular arc, the radius of curvature of the sting is given by $R = L/\Delta\alpha_S$, where L is the effective length of the sting over which bending takes place. The displacements Δx_S and Δz_S of the model resulting from sting deflection, measured along and perpendicular to the sting, respectively (see Fig. 16), are given by

$$\Delta x_S = L - R \sin \Delta\alpha_S \cong \frac{1}{6} L \Delta\alpha_S^2, \quad (15)$$

and

$$\Delta z_S = R - R \cos \Delta\alpha_S \cong \frac{1}{2} L \Delta\alpha_S. \quad (16)$$

The small-angle approximations assume that $\Delta\alpha_S$ is expressed in radians, and these approximations are justified because $\Delta\alpha_S$ is typically less than 3 deg in magnitude.

Figure 17 illustrates the resulting displacements, Δx_k^* and Δz_k^* , measured along the tunnel x^* - and z^* -axes for a PSP test of an F-16C model at 0.9 Mach number.³ Solid symbols represent model position measurements based on fully processed image data from eight cameras (see Ref. 8).

The continuous curves in Fig. 17 are curve fits based on the small-angle approximations from Eqs. (15) and (16), giving an effective sting length, L , of 63 ± 1 in. This, indeed, is the approximate length of the sting in this particular wind tunnel test.

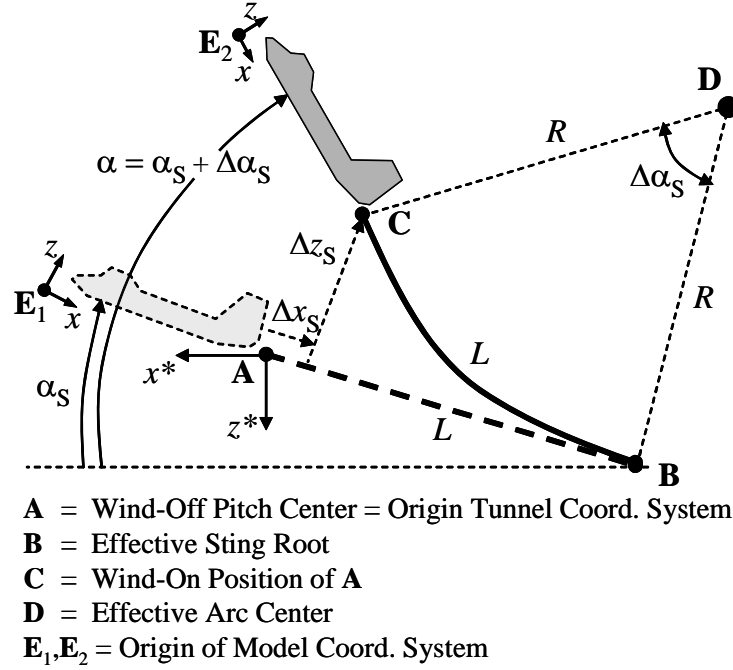


Figure 16. Schematic of Sting-Deflecting Model

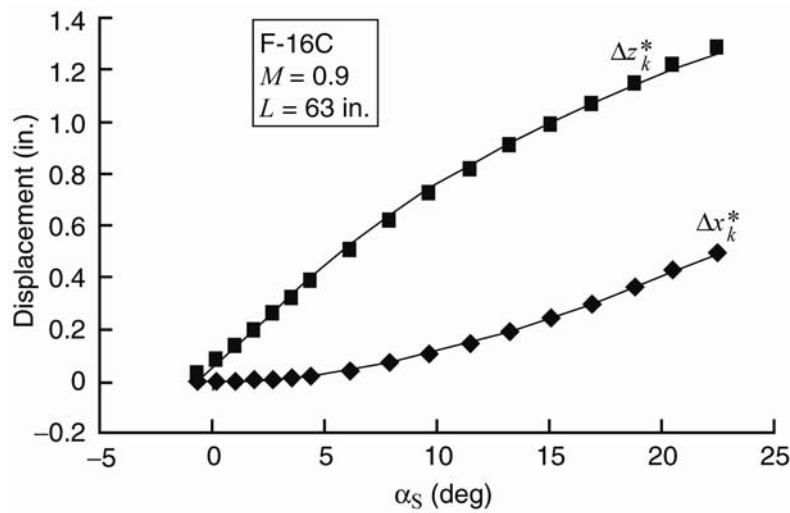


Figure 17. Sting Deflection of F-16C Model Under Air Loads

More generally, the effects of mounting the model at a prebend angle α_0 and the effects of rolling the sting by an amount ϕ_S must be included. So far it appears that, as far as the initial prediction of the resulting image coordinates of registration targets is concerned, the effects of out-of-plane bending caused by sideslip forces can be ignored, at least up to yaw angles of 8 deg relative to the wind vector. The sting bend angle $\Delta\alpha_S$ can then be estimated according to

$$\Delta\alpha_S = \alpha - \alpha_0 - \tan^{-1}(\cos \phi_S \tan \alpha_S). \quad (17)$$

If the origin of the tunnel coordinate system is chosen to be at the wind-off pitch-roll center of the sting mechanism (point A in Fig. 16), the resulting position vector \mathbf{x}_k^* and model orientation matrix \mathbf{R}_k^* from Eq. (13) are given by

$$\mathbf{x}_k^* = \mathbf{R}_y(\alpha_S) \mathbf{R}_x(\phi_S) [\Delta \mathbf{x}_S + \mathbf{R}_y(\alpha_0 + \Delta \alpha_S) \mathbf{x}_m] \quad (18)$$

and

$$\mathbf{R}_k^* = \mathbf{R}_y(\alpha_S) \mathbf{R}_x(\phi_S) \mathbf{R}_y(\alpha_0 + \Delta \alpha_S) \mathbf{R}_m. \quad (19)$$

Here \mathbf{R}_y and \mathbf{R}_x are pitch and roll matrices about y - and x -axes, respectively, by the angles indicated. The displacement vector, $\Delta \mathbf{x}_S$, is given in terms of the components from Eqs. (15) and (16) by

$$\Delta \mathbf{x}_S = -(\Delta x_S, 0, \Delta z_S). \quad (20)$$

The minus sign in Eq. (20) is required because of the particular choice of tunnel coordinates, with an x^* -axis pointing upstream and a z^* -axis pointing downstream (see Fig. 16).

Finally, \mathbf{x}_m and \mathbf{R}_m in Eqs. (18) and (19) describe the position and orientation of the test article at the wind-off reference condition, i.e., at zero pitch, yaw, and roll. Typically, it is adequate to express \mathbf{x}_m and \mathbf{R}_m as

$$\mathbf{x}_m = (x_m, 0, z_m), \quad \mathbf{R}_m = \mathbf{D}(-1, +1, -1), \quad (21)$$

where x_m and z_m are the horizontal and vertical positions of the origin of the model coordinate system and \mathbf{D} is a diagonal matrix with elements as indicated. As is the case in Eq. (20), the minus signs in Eq. (21) are a result of the choice of coordinate system in Fig. 16.

4.5 RESULTING PREDICTION MODEL

In combination, Eqs. (7) through (21) constitute a complete set of equations for the prediction of a set of image coordinates (u_i, v_i) from a set of model coordinates \mathbf{x}_i , based on four sets of parameters: a set of exterior camera parameters $\mathbf{p}_c^* = \{x_c^*, y_c^*, z_c^*, \phi_c^*, \kappa_c^*, \omega_c^*\}$; a set of interior camera parameters $\mathbf{q}_c = \{f_c, u_c, v_c, K_{Ic}\}$; a set of variable sting angles $\mathbf{a}_k = \{\alpha, \alpha_S, \phi_S\}$; and a set of fixed tunnel parameters $\mathbf{t} = \{\alpha_0, x_m, z_m, L\}$. Symbolically, the resulting transformation may be written in terms of a mapping function, F , as

$$(u_i, v_i) = F(\mathbf{x}_i; \mathbf{p}_c^*, \mathbf{q}_c, \mathbf{a}_k, \mathbf{t}). \quad (22)$$

Of course, the mere fact that a set of image coordinates (u_i, v_i) can be calculated for a target i does not guarantee that the target will, in fact, be visible in the image. Three additional conditions must be met to ensure such visibility:

- (1) The predicted image coordinates must fall within the bounds of the image.
- (2) For the usual case of an opaque model, the surface normal of the target must point toward the camera.
- (3) The target must not be occluded by other parts of the test article or tunnel mounting structure.

The first of these conditions can easily be verified based on the known size of the image, i.e., by requiring that

$$1 + s < u_i < N_u - s, \quad 1 + s < v_i < N_v - s. \quad (23)$$

Here $(1, 1)$ and (N_u, N_v) represent the coordinates of the bottom left and upper right corners of the image. The skirt width, s (typically, a few image pixels), is applied to eliminate from consideration targets that may, in fact, be wholly or partially outside the image.

The second visibility condition can also be verified easily if a target normal, \mathbf{n}_i , is specified for each target, i . If \mathbf{n}_i is expressed in model coordinates, then $\mathbf{R}_k^* \mathbf{n}_i$ is the orientation of the target in tunnel space. The second visibility condition can thus be expressed as

$$\left[(\mathbf{x}_i^* - \mathbf{x}_c^*) \bullet \mathbf{R}_k^* \mathbf{n}_i \right] < 0. \quad (24)$$

The third visibility condition (that a target not be occluded) is more difficult to ascertain for a complex 3D test article, but it can nevertheless be checked if a detailed 3D geometry grid of the test article is available. (This is typically the case in luminescent paint measurements.) In particular, reinterpret Eqs. (7) through (21) as applying to grid points g , as opposed to target points, i . It is then possible to compute a set of values $\{u_g, v_g, -W_g\}$ for each grid point g , where u_g and v_g are projected image coordinates from Eq. (10) and $-W_g$ is the negative of the third component of the vector \mathbf{U} from Eq. (8). This value, $-W_g$, may be interpreted as the distance from a grid point \mathbf{x}_g^* to the focal plane of the camera.

The values $\{u_g, v_g, -W_g\}$ can be arranged in a depth buffer (usually called a z-buffer³¹), in which each pixel (p, q) holds a value, W_{buf} , that represents the distance from the camera to the part of the test article that is viewed by that pixel. If such a depth buffer, $W_{\text{buf}}(p, q)$, can be computed, the third visibility condition for a target i can be written as

$$-W_i < W_{\text{buf}}(p_i, q_i) + \varepsilon_W, \quad (25)$$

where (p_i, q_i) are the projected coordinates of target i rounded to the nearest pixel value, $-W_i$ is the distance value for target i , and ε_W is a tolerance parameter that prevents the rejection of legitimate targets because of small discrepancies between grid coordinates and target coordinates. If the depth buffer is calculated from a closed surface grid, Eq. (25) implies Eq. (24).

4.6 TEMPLATE-BASED TARGET SEARCH

Using the model from Sections 4.3, 4.4, and 4.5, it is possible to predict the image coordinates (u_i, v_i) of all registration targets that should be visible in an image. The next step is to find the actual target locations within some search radius from the initial predictions and to determine the exact locations of the targets to subpixel accuracy. Two techniques are widely used for such searches: blob-finding and template-based correlation matching. Blob finders typically do not take into consideration the shape of the registration target. Instead, they isolate a contiguous set of pixels that contrasts strongly with the background. The center of the blob is calculated by centroiding, i.e., by performing an intensity-weighted average of individual pixel locations in the blob,³² following subtraction of the background signal.

By contrast, template-based techniques employ a search template (see Fig. 18) that matches the shape, size, and orientation of the desired image feature. This allows for more robust searching than is possible with a blob finder and reduces the probability that legitimate image features will go undetected and that unwanted artifacts will be mistakenly identified as targets.

A typical search template consists of an array of numbers between 0 and 1 (see Fig. 19) in which each value represents the fraction of the corresponding image pixel that falls inside the projected outline of the desired registration target. This template is stepped across the image in one-pixel increments to find a point of maximum correlation.³³ Subpixel centering can be achieved by subjecting the resulting array of correlation values, in turn, to a centering determination (for example, by sampled correlation interpolation).³⁴

A new variation of template-based correlation matching is described in Refs. 17 and 29, in which the conventional search template (such that as in Fig. 19) is augmented by two additional arrays (denoted here by f_u and f_v —see Fig. 20), which represent the derivatives of the occupied pixel fractions f_0 with

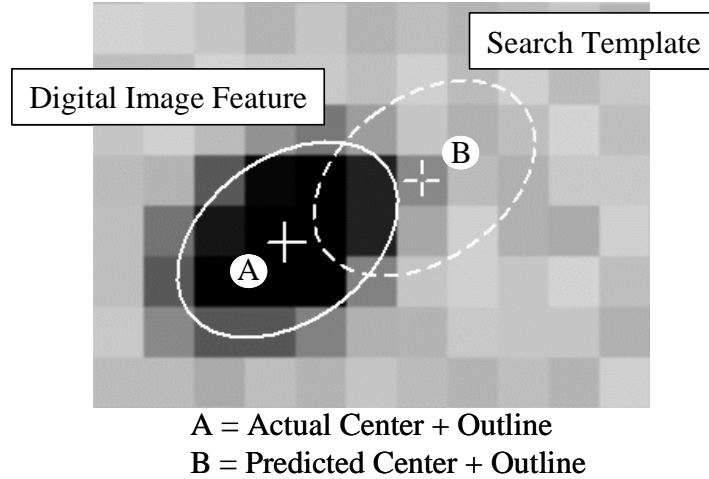


Figure 18. Illustration of Use of Search Template

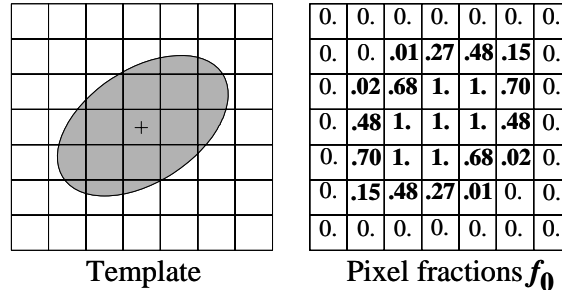


Figure 19. Example of Conventional Search Template

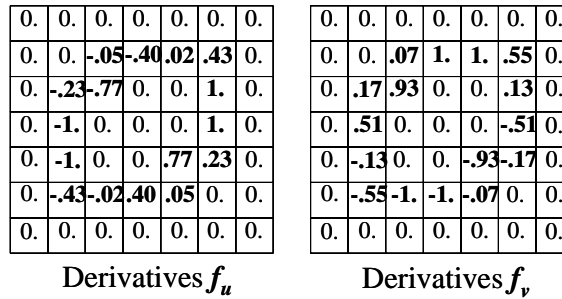


Figure 20. Augmented Templates Corresponding to Figure 4.5

respect to subpixel shifts of the search template along the image axes. It is shown in Ref. 17 that incorporation of the derivative templates allows for more accurate subpixel centering of registration targets than is possible with either blob finding or conventional template matching and that augmentation of the search template produces higher correlation values than does the nonaugmented case.

Below, the implementation of both conventional and augmented template matching is reviewed for use with image registration.

4.6.1 Calculation of the Search Template

Let $\{\mathbf{x}_{ij}\}$ denote a set of n points (with $j = 1, \dots, n$) on the perimeter of a registration target i that has passed the visibility tests from Eqs. (23) through (25). In particular, for a solid, circular target with radius r_i and position x_i in model space, the set of points $\{x_{ij}\}$ may be calculated as

$$\mathbf{x}_{ij} = \mathbf{x}_i + r'_i \left[\mathbf{l}_i \cos\left(\frac{2\pi j}{n}\right) + \mathbf{m}_i \sin\left(\frac{2\pi j}{n}\right) \right], \quad j = 1, \dots, n. \quad (26)$$

Here \mathbf{l}_i and \mathbf{m}_i are unit tangents that are calculated from the surface normal \mathbf{n}_i , with $\mathbf{n}_i = \mathbf{l}_i \times \mathbf{m}_i$, and r'_i is essentially the target's radius r_i , with a small correction that renders the area of the resulting n -sided polygon equal to that of the circular target:

$$r'_i = r_i \left[\frac{2\pi/n}{\sin(2\pi/n)} \right]^{1/2}. \quad (27)$$

The assumption is made that the surface is flat on the scale of the target. Using Eq. (22), a corresponding set of image coordinates (u_{ij}, v_{ij}) may be calculated. By interpolation, this set of projected perimeter points can be expanded into a K -sided polygon (with $K > n$), such that each line segment is contained inside a single image pixel (see Fig. 21). Let (u_{k-1}, v_{k-1}) and (u_k, v_k) be the end points of the k -th line segment for some target i , with $(u_0, v_0) = (u_K, v_K)$, and let (p_k, q_k) denote the indices of the pixel in which the k -th line segment is contained. The partial contributions of line segment k to the occupied pixel fractions $f_0(p_k, q)$ of a column of pixels that extends downward from the pixel (p_k, q_k) is then given by

$$\Delta f_{0k}(p_k, q) = \begin{cases} (u_{k-1} - u_k) \left(\frac{v_k + v_{k-1}}{2} - q_k \right), & q = q_k, \\ u_{k-1} - u_k, & q_{\min} \leq q < q_k. \end{cases} \quad (28)$$

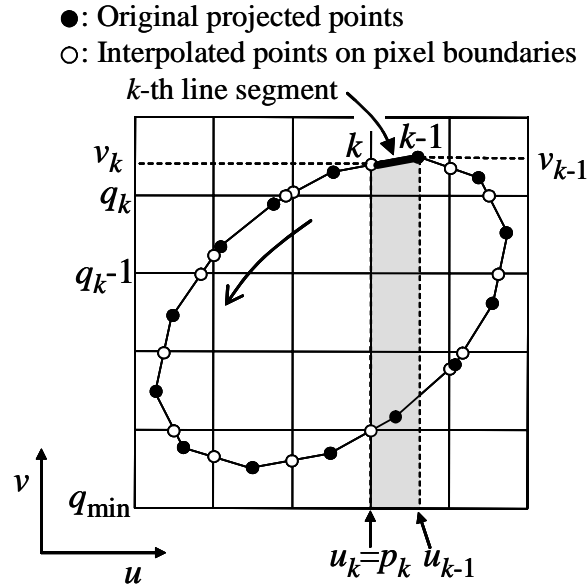


Figure 21. Calculation of Template from Polygonal Curve

Here q_{\min} is the lowest value of q_k in the template. Individual contributions Δf_{0k} can be either positive or negative. However, when contributions from all line segments k are added, the resulting template values will be in the range $0 \leq f_0 \leq 1$, provided that the projected outline of the template is traversed in a counter-clockwise direction.

To calculate the derivative templates that are required for augmented template matching, observe that the change in the value Δf_{0k} for a pixel (p_k, q_k) caused by an infinitesimal shift δu of the template along the u -axis is equal to $(v_k - v_{k-1}) \delta u$; observe also that the change in Δf_{0k} caused by an infinitesimal shift δv along the v -axis is equal to $(u_{k-1} - u_k) \delta v$. The partial contributions of line segment k to the derivative templates f_u and f_v can thus be calculated as

$$\Delta f_{uk}(p_k, q_k) = v_k - v_{k-1}, \quad \Delta f_{vk}(p_k, q_k) = u_{k-1} - u_k. \quad (29)$$

When the partial contributions Δf_{uk} and Δf_{vk} of all k line segments are summed, the resulting arrays of values of f_u and f_v are in the range from -1 to $+1$ for each pixel (see Fig. 20). Inclusion of a skirt with zero values of f_0 , f_u , and f_v along the edges of the template (as shown in Figs. 19 and 20) has been found to improve the performance of the template search.

4.6.2 Conventional Template Matching

In conventional template matching, a perfect match between an array of template values f_0 and an image feature (represented by an array of intensity values g) is obtained if there exists a set of integer shifts $(\Delta p, \Delta q)$ that renders the image values $g(p + \Delta p, q + \Delta q)$ exactly equal to the scaled template values $b + cf_0(p, q)$, where b is the image background value outside the template, c is a contrast term (which can be positive or negative), and p and q are pixel indices in the template. More generally, a measure of the match between the image feature and the template is provided by the normalized correlation

$$J_{fg}(\Delta p, \Delta q) \equiv \frac{S_{fg}^2}{S_{ff} S_{gg}} \quad (\text{with } 0 \leq J_{fg} \leq 1), \quad (30)$$

where

$$S_{ff} \equiv \sum_{p,q} [f_0(p, q) - \langle f_0 \rangle]^2, \quad (31)$$

$$S_{fg}(\Delta p, \Delta q) \equiv \sum_{p,q} [f_0(p, q) - \langle f_0 \rangle][g(p + \Delta p, q + \Delta q) - \langle g \rangle], \quad (32)$$

$$S_{gg}(\Delta p, \Delta q) \equiv \sum_{p,q} [g(p + \Delta p, q + \Delta q) - \langle g \rangle]^2. \quad (33)$$

$$\langle f_0 \rangle \equiv \sum_{p,q} f_0(p, q) / \sum_{p,q} 1, \quad (34)$$

and

$$\langle g(\Delta p, \Delta q) \rangle \equiv \sum_{p,q} g(p + \Delta p, q + \Delta q) / \sum_{p,q} 1. \quad (35)$$

The sums in Eqs. (31) through (35) extend over all pixels (p, q) in the template and hence over the equivalent region of the image, as determined by the shifts Δp and Δq .

Perfect correlation between the template and the image is signified by a value $J_{fg} = 1$ for some set of integer shifts $(\Delta p, \Delta q)$. In practice, the template is stepped across the image by varying the integer shifts

Δp and Δq until a point of maximum and sufficient correlation is found (i.e., a value J_{fg} above some threshold J_{\min} , with $J_{\min} < 1$).

4.6.3 Augmented Template Matching

Assume that a conventional template match, as described in Section 4.6.2, has been performed in the vicinity of a predicted target location (u_i, v_i) , resulting in the tentative identification of the desired registration target at a location $(u_i + \Delta p, v_i + \Delta q)$ for some set of integer shifts Δp and Δq . Now imagine that the template is shifted by a further, subpixel set of shifts $(\Delta u, \Delta v)$. To first order, this is equivalent to replacing the occupied pixel fractions $f_0(p, q)$ with the values $f_0(p, q) + f_u(p, q)\Delta u + f_v(p, q)\Delta v$, where f_u and f_v are the derivative terms computed in Section 4.6.1 and Δu and Δv are the to-be-determined subpixel shifts. Substitution of this first-order Taylor expansion for the template into Eqs. (30) through (35) leads to an optimization problem with respect to the unknown subpixel shifts Δu and Δv , namely, to maximize the resulting value of J_{fg} . Seven additional correlation sums arise (see Fig. 22) and are denoted by S_{uu} , S_{uv} , S_{vu} , S_{vv} , S_{fu} , S_{fv} , $S_{ug}(\Delta p, \Delta q)$ and $S_{vg}(\Delta p, \Delta q)$. These sums are defined analogously to Eqs. (30) through (35) with, in this case, $\langle f_u \rangle = \langle f_v \rangle = 0$.

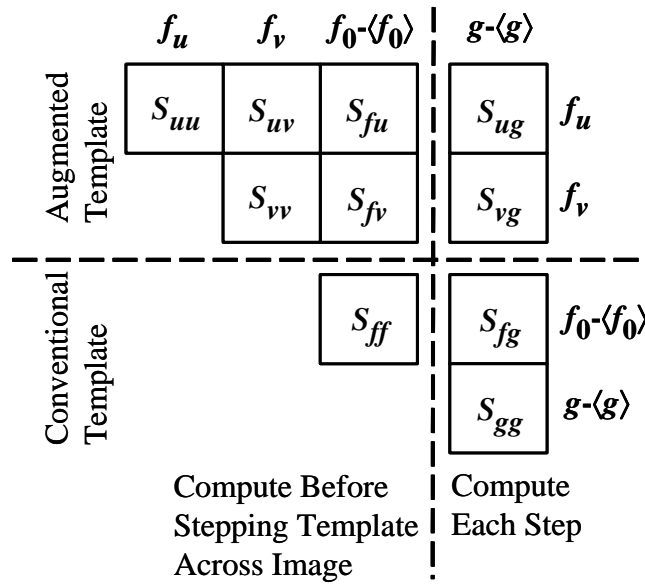


Figure 22. Correlation Sums Arising in Augmented Template Search

For the special case in which the derivative templates f_u and f_v are orthogonal to the occupied pixel fractions f_0 (i.e., the case in which $S_{fu} = S_{fv} = 0$), the solution of the resulting optimization problem is obtained for subpixel shifts Δu and Δv given by (see Ref. 17):

$$\begin{pmatrix} \Delta u \\ \Delta v \end{pmatrix} = \frac{S_{ff}}{S_{fg}} \begin{pmatrix} S_{uu} & S_{uv} \\ S_{uv} & S_{vv} \end{pmatrix}^{-1} \begin{pmatrix} S_{ug} \\ S_{vg} \end{pmatrix}. \quad (36)$$

In terms of these subpixel shifts, the best estimate for the center of the registration target is now given by $(u_i + \Delta p + \Delta u, v_i + \Delta q + \Delta v)$. The associated augmented normalized correlation value, J_{fg}^* , is given in terms of the conventional value J_{fg} , from Eq. (30), by

$$J_{fg}^* = J_{fg} + \frac{S_{fg}}{S_{ff} S_{gg}} [S_{ug} \Delta u + S_{vg} \Delta v] \geq J_{fg}. \quad (37)$$

For circular registration targets, a simple way to ensure that the condition $S_{fu} = S_{fv} = 0$ is satisfied is to shift, in Section 4.6.1, the polygonal outline of the projected target such that its center is located at either an integral or a half-integral position in both the u and v directions. More generally, Eqs. (36) and (37) may be replaced with somewhat more involved formulas (quadratic in Δu and Δv) that include the nonzero sums S_{fu} and S_{fv} (see Section 3.1 of Ref. 17).

By iterating the calculation of the search template (this time, without shifting the projected target center to an integral or a half-integral location) and recomputing the subpixel shifts Δu and Δv , even more accurate centering of the template with respect to the image is possible (see Ref. 17). Also, Ref. 29 (see Section 5) addresses the extension of the augmented template technique to poorly rendered image features, for which the implicit assumption of uniform values of background and contrast breaks down. In Refs. 17 and 29 it is also shown how the precision of the augmented centering determination can be estimated from the achieved correlation values.

4.7 COMPLETION OF THE IMAGE REGISTRATION TASK

With all (or nearly all) of the registration targets found that were deemed visible in the image, the task remains to complete the image registration process. The exact form in which this is to be accomplished depends on the application. For example:

(1) The discrepancy between the predicted and measured image coordinates (u_i, v_i) is attributed to the position vector \mathbf{x}_k^* and orientation matrix \mathbf{R}_k^* from Eq. (14) being different from the prediction from Eqs. (15) through (21). This calls for a nonlinear least-squares fit of the measured image coordinates (u_i, v_i) using Eqs. (7) through (14), with $x_k^*, y_k^*, z_k^*, \alpha_k^*, \beta_k^*$, and ϕ_k^* as fit parameters. This produces an updated mapping transformation between 2D image and 3D model coordinates, as well as a measurement of the actual location and attitude of the test article. A useful measure of the agreement between measured (“exp”) and fitted (“fit”) image coordinates is provided by the root-mean-square difference, σ , between the two, defined as

$$\sigma \equiv \left[\frac{1}{N} \left\{ \left[u_i^{(\text{exp})} - u_i^{(\text{fit})} \right]^2 + \left[v_i^{(\text{exp})} - v_i^{(\text{fit})} \right]^2 \right\} \right]^{1/2}, \quad (38)$$

where N is the number of registration targets in the image.

(2) To improve the accuracy of an optical model attitude determination, data from two or more calibrated cameras can be combined in a single least-squares fit, defined, again, in terms of a set of to-be-determined parameters $x_k^*, y_k^*, z_k^*, \alpha_k^*, \beta_k^*$, and ϕ_k^* . This approach, including the estimation of the uncertainties of the resulting position and attitude determination, is discussed in more detail in Ref. 15.

(3) At the outset of a wind tunnel test, it is necessary to calibrate the exterior and interior parameters of the cameras, as well as some of the parameters that are used in the sting model from Section 4.3, most notably the offsets x_m and z_m in Eqs. (21) and the effective sting length, L , in Eqs. (15) and (16). See, e.g., Refs. 14 and 15. During this calibration, it typically is necessary for the user to select a number of registration targets manually when setting images.

(4) A high rms error in Eq. (38) may indicate that the assumption of rigid-body motion is invalid and that some amount of model deformation occurs. Nevertheless, to achieve an accurate mapping between 2D image coordinates and 3D spatial coordinates, additional parameters must be introduced. A simple approach (though without a clear theoretical justification) is to replace the projective transform equations from Eqs. (7) and (8) with a direct linear transform of the form^{14,15,20}

$$u_i^{(0)} = \frac{L_1 x_i + L_2 y_i + L_3 z_i + L_4}{L_9 x_i + L_{10} y_i + L_{11} z_i + 1}, \quad v_i^{(0)} = \frac{L_5 x_i + L_6 y_i + L_7 z_i + L_8}{L_9 x_i + L_{10} y_i + L_{11} z_i + 1}, \quad (39)$$

and leave all the parameters $L_1 \dots L_{11}$ variable. [When interpreted as a projective transform, the same 11 coefficients are constrained to only nine degrees of freedom, corresponding to the six exterior camera parameters from Eq. (8) and the three interior camera parameters u_c , v_c , and f_c from Eq. (7).] Because of the two additional degrees of freedom, a lower rms value is obtained in Eq. (38), giving a (potentially) improved mapping between the 2D and 3D coordinates. In a more sophisticated approach, additional terms corresponding to specific deformation modes of the test article are included, such as bending and twisting of a wing.^{26,27} However, a detailed treatment of such model deformation issues is beyond the scope of the present study.

4.8 IMPLEMENTATION OF ALGORITHM AND ITS USE

Figure 23 illustrates a possible implementation of the theory from Sections 4.3 through 4.7 to perform automatic image registration by (1) estimating the position \mathbf{x}_k^* and attitude matrix \mathbf{R}_k^* of the test article with respect to the test facility; (2) calculating the resulting mapping coefficients for transformation of 3D model coordinates to 2D image coordinates; (3) calculating initial predictions of the locations of all visible registration targets, including search templates; (4) finding the exact locations of the targets; and (5) updating the resulting mapping coefficients—for example, by calculating updated values of \mathbf{x}_k^* and \mathbf{R}_k^* .

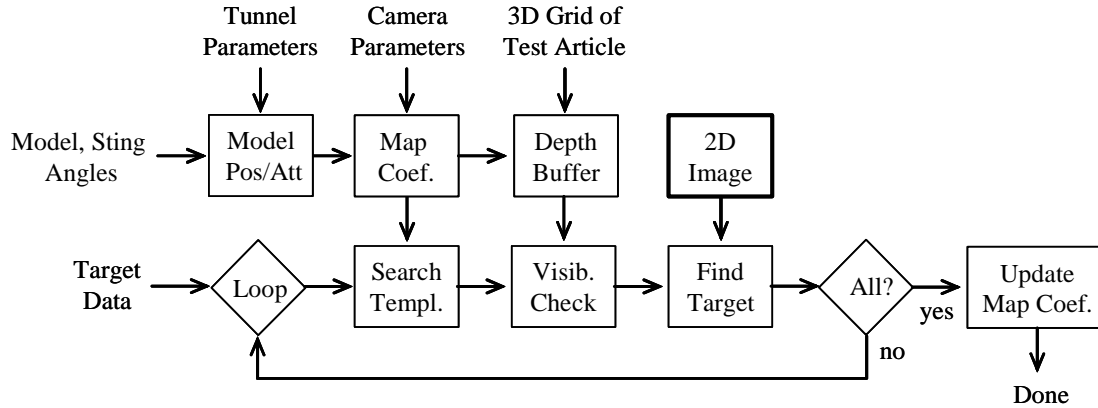


Figure 23. Image Registration Flow Diagram

Four sets of input are required: (1) a list of model coordinates \mathbf{x}_i , normals \mathbf{n}_i , and target diameters d_i for all registration targets; (2) exterior parameters $\mathbf{p}_c^* = (x_c^*, y_c^*, z_c^*, \phi_c^*, \kappa_c^*, \omega_c^*)$ and interior parameters $\mathbf{q}_c = \{f_c, u_c, v_c, K_{1c}\}$ for each camera; (3) a set of fixed tunnel-related parameters $\mathbf{t} = \{\alpha_0, x_m, z_m, L\}$; and (4) a set of angles $\mathbf{a}_k = \{\alpha, \alpha_s, \phi_s\}$ for each data point. Optionally, a 3D grid of the test article can be provided as a fifth input, if z-buffer visibility checks are to be performed based on Eq. (25). Additional parameters that have to be specified are listed below.

- (1) The parameters s , N_u , N_v , and ε_w from Eqs. (23) and (25), which are used to verify target visibility.
- (2) The number of points n from Eq. (26), used to calculate the search templates. (A typical value is $n = 90$, though smaller values would probably suffice.)
- (3) Minimum acceptable correlation values J_{\min} and J_{\min}^* for the nonaugmented and augmented correlation values, respectively (typical values are $J_{\min} = 0.5$ and $J_{\min}^* = 0.75$), and a maximum acceptable value for the magnitudes of the subpixel shifts Δu and Δv from Eq. (35) (typically, 0.7 pixels each).
- (4) The magnitude of the search radius around the initial target prediction within which the actual target is to be found (typically, 5 to 10 pixels).
- (5) A minimum acceptable fraction of targets (found versus predicted) at the end of a correlation search (typically 0.9 if a z-buffer is used to ascertain target visibility).

(6) A maximum acceptable deviation δs_{\max} between measured and fitted image coordinates (u_i, v_i) for individual targets i in Eq. (38) to help flag outlier points (typically, $\delta s_{\max} = 2$ pixels).

(7) A maximum acceptable rms fit error for all targets combined in Eq. (37) (typically, 1 pixel).

Selection of these various parameters depends on the test being performed and usually requires some empirical optimization. (Quoted values are typical for PSP testing in AEDC's 16-ft Transonic Wind Tunnel 16T.)

4.9 SAMPLE RESULTS

The image registration algorithm described in Sections 4.3 through 4.8 has been used extensively as the enabling step for automatic processing of thousands of PSP images from Tunnel 16T (see, especially, Ref. 24). Performance results of the template-based search algorithm are documented in Ref. 29. Use of the augmented template technique typically results in 99 percent or more of visible registration targets being found correctly.²⁹ (For poor lighting conditions, this requires extension of the augmented template technique as described in Ref. 29.) As a single example, Fig. 2 shows a registered image from a PSP test of an F-16C, with closeups of some of the registration targets. Target diameters in Fig. 2 (at about two image pixels) were smaller than ideal (about five pixels), but they still allowed target centers to be determined to accuracies of about 0.07 image pixels in both the u - and v -directions.

The most critical element of the automatic image registration scheme is the prediction model from Section 4.4. (Without good initial predictions for the target locations, the simple yet powerful search scheme from Section 4.6 becomes much harder to implement; see, e.g., Ref. 16.) An important figure of merit, therefore, is the worst-case rms prediction error for visible target locations in an image, defined analogous to Eq. (37), but with predicted image coordinates taking the place of fitted coordinates. Table 6 lists such maximum prediction errors for three tests in Tunnel 16T, involving an F-16C jet, NASA's X-38 Crew Return Vehicle, and a Joint Strike Fighter model. The maximum rms prediction errors are 2.4, 3.1, and 3.7 image pixels, respectively, assuming that all fixed parameters (such as camera focal lengths and effective sting length) have been optimized. Average prediction errors are even smaller, at around one image pixel for all three tests. Also shown in Table 6 are the maximum rms prediction errors that result if sting deflection is not taken into account, giving maximum rms errors of 7.8, 3.8, and 9.2 image pixels, respectively. Inclusion of a droop term (to account for bending of the sting under the force of gravity, typically on the order of 0.3 deg or less) has also been implemented, but this did not result in a significant reduction of the maximum prediction errors. Alternate sting positioning models are also possible. For example, some use a yaw head or a knuckle-sleeve system that compensates for vertical motion of the test article.

4.10 CONCLUSION

An efficient technique for registration of digital images of sting-mounted test articles undergoing rigid-body motion has been implemented at AEDC specifically to accomplish automatic data reduction of PSP images. The technique relies on the initial prediction of the location of all registration targets that should be visible in an image, the use of an augmented template search to find the actual target locations to subpixel accuracy, and a nonlinear, least-squares fitting algorithm to establish the exact mapping transformation from 3D model coordinates to 2D image coordinates. In the process, an accurate measurement of the position and attitude of the test article is obtained. Two elements of the technique, in particular, are key to its successful implementation and are believed to be novel. These are the use of a sting deflection model under air loads and the use of an augmented template scheme for correlation-based target finding. Results indicate that initial prediction of target locations is possible to within about five image pixels and that the final accuracy of target localization is better than one-tenth of an image pixel. The technique has been used successfully on thousands of images acquired in Tunnel 16T and should be applicable to optical testing in other test facilities.

Table 6. Selected Data from Three Wind Tunnel Tests

	F-16C	X-38	JSF
Number of Cameras	8	8	5
Number of Images	400	1560	1130
Targets per Image (Avg.)	34	12	17
Mach Number Range	0 to 0.9	0 to 1.4	0 to 0.9
α_0 , deg	1	3	8
L , in	63	88	38
α Range, deg	0 to 26	4 to 20	-8 to 24
β Range, deg	0	-4 to 4	-8 to 8
α_s Range deg	-1 to 25	1 to 17	-16 to 16
ϕ_s Range, deg	0	-21 to 21	-46 to 45
$\Delta\alpha_s$ Range, deg	2.4	0.7	1.5
Max Rms Error w/o Defl, pix	7.8	3.8	9.2
Max Rms Error w/ Defl, pix	2.4	3.1	3.7
Average Rms Error w/ Defl, pix	0.9	1.3	1.2

4.11 ACKNOWLEDGMENTS

Marvin Sellers and Daryl Sinclair provided helpful discussions on the subject matter.

5.0 EXTENSION OF SUBPIXEL-AUGMENTED TEMPLATE MATCHING TO IMPERFECTLY RENDERED BINARY TARGETS[§]

5.1 OVERVIEW

In a previous publication (Ref. 17) a new method was introduced for correlation matching of binary targets (e.g., a light, uniform target on a dark, uniform background). This new method, which is summarized in Section 3.6, is based on the use of an augmented search template that contains not only the occupied pixel fractions of the synthetic reference that is being located, but also the derivatives of these pixel fractions with respect to shifts of the template along the image axes. In this section, the augmented template technique is extended to cases in which a binary target is used for image registration but is not rendered as a binary image feature because of experimental artifacts such as specular reflection, mixed image contrast, or partial occlusion. It is shown that subpixel localization of the target can still be accomplished, by extending the concept of a single augmented template to a composite template, a method that consists of overlapping three-by-three subtemplates. Examples of noncomposite and composite augmented template matching are demonstrated experimentally.

5.2 INTRODUCTION

Many engineering disciplines require the (automatic) detection of synthetic references (SRs) in digital images for machine vision, image registration, optical diagnostics, metrology, etc. A common approach is the use of search templates and correlation matching.^{33, 35, 36} Typically, the search template is stepped across the scene in one-pixel increments. Detection of the SR occurs when the chosen similarity measure exceeds a threshold value. To achieve subpixel resolution, sampled correlation interpolation (SCI) may be used,^{34,37-39} or multiple search templates may be used, each calculated for a different subpixel placement of the SR.^{34,40-42} In Ref. 17 a new approach is explored, based on the insight that it is possible to achieve subpixel resolution by using, in the search template, not only the occupied pixel fractions (as is done in conventional correlation matching), but also the derivatives of the occupied pixel fractions with respect to shifts of the template along the image axes. This approach has two advantages over conventional correlation matching. First, it produces larger correlation values for unfavorable subpixel displacements between SR and scene, thereby causing fewer SRs to go undetected.³³ Second, the new approach allows the subpixel location of the SR to be determined more precisely than is possible with either SCI or centroiding.^{43,44} In Ref. 17, these properties of augmented template matching are demonstrated for strict use of normalized correlation as the similarity measure. Pertinent highlights from Ref. 17 are summarized in Sections 5.3 and 5.4 (as well as in Section 3.6). In Sections 5.5 through 5.7 the theory from Ref. 17 is applied in practice and is generalized for situations in which experimental artifacts preclude the use of normalized correlation in its conventional form.

5.3 REVIEW OF CONCEPT

Let the term J_{fg} denote a suitable similarity measure between a template f and a scene g . For example, J_{fg} might be the normalized correlation (Sections 5.4 and 5.5) or a more general measure (Sections 5.6 and 5.7). Typically, the template is calculated for a fixed relative placement of the SR, e.g., with the SR centered on a pixel. A search is then performed by stepping the template across the scene in one-pixel increments. An array of values $J_{fg}(m,n)$ is thus obtained, where m and n are integers. Detection of the SR occurs when J_{fg} exceeds a threshold value J_{\min} .^{33,35,36} In Ref. 17 subpixel resolution is achieved by

[§]Previously published as "Extension of Subpixel Augmented Template Matching to Imperfectly Rendered Binary Targets," in *Optical Engineering*, Vol. 43, No. 3, March 2004, pp. 639-647.

expanding the search template as a first-order Taylor series in terms of a set of to-be-determined subpixel shifts Δx and Δy according to

$$f = f_0 + f_x \Delta x + f_y \Delta y. \quad (40)$$

Figure 24 (see also Figs. 19 and 20) shows an example of such an augmented template (AT) for a binary SR, i.e., an SR that is chosen to yield a high-contrast image feature with roughly uniform foreground and background signals. (Contrast with this the use of the term “binary template” to denote a template that consists of only ones and zeros.⁴⁵) For a binary SR in the current sense (with $0 \leq f_0 \leq 1$), the f_x and f_y terms can be obtained as occupied height and width differences at opposite sides of a pixel, as is illustrated in Fig. 25.

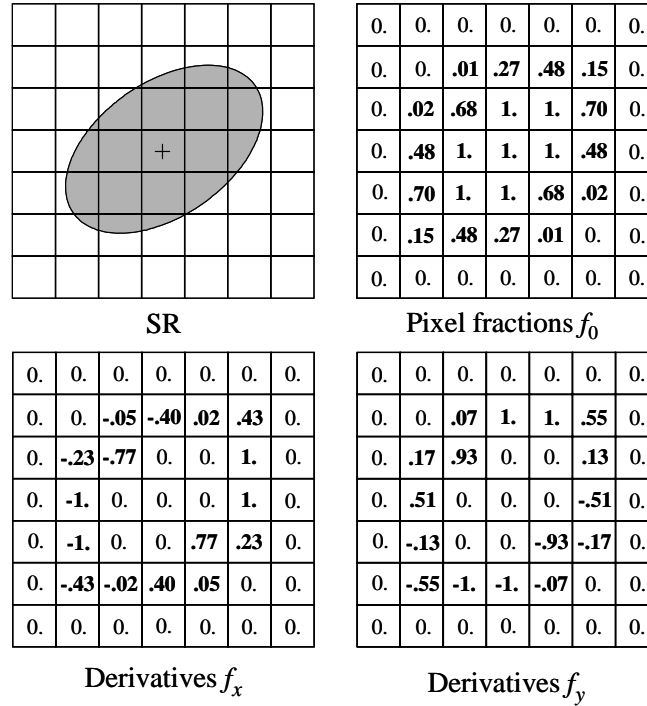


Figure 24. Example of Augmented Template

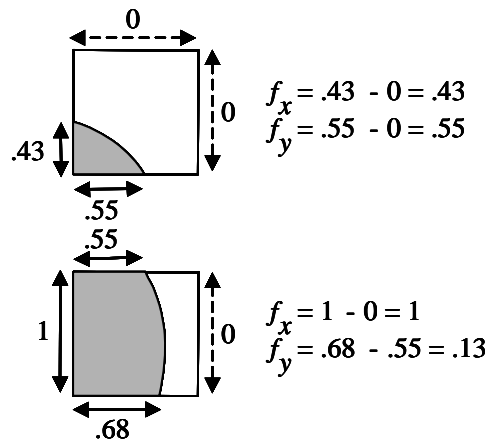


Figure 25. Determination of AT Derivative Terms

When Eq. (40) is substituted into the chosen similarity measure, the discretely sampled $J_{fg}(m,n)$ becomes a function of the shifts Δx and Δy , i.e., $J_{fg} = J_{fg}(m+\Delta x, n+\Delta y)$. The role of the AT can now be defined as follows: for a given set of integer shifts (m,n) , find the additional shifts $(\Delta x, \Delta y)$ that maximize $J_{fg}(m+\Delta x, n+\Delta y)$. This maximized correlation value is denoted with an asterisk, as shown below.

$$J_{fg}^*(m,n) \equiv \max_{\Delta x, \Delta y} [J_{fg}(m+\Delta x, n+\Delta y)]. \quad (41)$$

This augmented correlation still needs to be optimized as a function of the integer shifts (m,n) , as is the case in conventional correlation matching. Figure 26 gives a typical implementation of this concept: an initial placement (x_0, y_0) of the SR is selected, and the AT is calculated (Steps 1 and 2). A standard correlation search is then performed (Steps 3 through 5), until J_{fg} exceeds a preset threshold J_{\min} . At this point, the AT is invoked (Steps 6 through 9) to calculate shifts Δx and Δy . A check is performed (Step 7) to verify that the magnitude of the shift is below a threshold value Δs_{\max} , typically one pixel. Definitive detection of the SR, at a location $(x_0+m+\Delta x, y_0+n+\Delta y)$, is flagged when the AT-based correlation J_{fg}^* exceeds a threshold value J_{\min}^* (which is set higher than J_{\min}). The SR being found, the AT is recalculated and recentered iteratively (Steps 10 through 14) until the magnitudes of the subpixel shifts $(\Delta x, \Delta y)$ are smaller than their respective precisions. Examples of this approach are given in Sections 5.4 through 5.7, below.

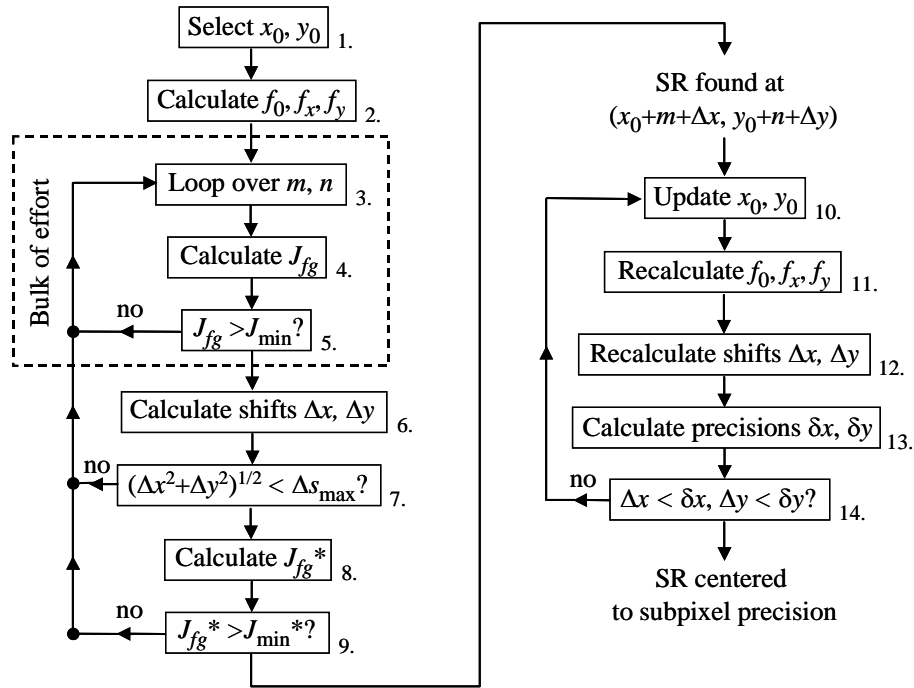


Figure 26. Flow Diagram for Augmented Template Search and Centering

5.4 REVIEW OF THEORY FOR BINARY SCENE

When scene and template are related by a strict gray-level transformation, i.e., $g = b + cf$, where the background b and contrast c are constants, a suitable similarity measure is provided by the normalized correlation^{35,36}

$$J_{fg} = [\Sigma(f - \langle f \rangle)(g - \langle g \rangle)]^2 / [\Sigma(f - \langle f \rangle)^2][\Sigma(g - \langle g \rangle)^2] \equiv S_{fg}^2 / S_{ff} S_{gg}. \quad (42)$$

When the AT expansion from Eq. (40) is substituted into Eq. (42), additional correlation sums arise, namely S_{fx} , S_{fy} , S_{xx} , S_{xy} , S_{yy} , S_{xg} , and S_{yg} (see Fig. 22). For example, $S_{fx} \equiv \Sigma(f_0 - \langle f_0 \rangle)(f_x - \langle f_x \rangle)$, with $\langle f_x \rangle = 0$. As is shown in Ref. 17, maximization of the ensuing J_{fg} with respect to the subpixel shifts Δx and Δy is facilitated by initial placement of the SR such that the derivative terms f_x and f_y are orthogonal to the pixel fractions f_0 , in the sense that $S_{fx} = S_{fy} = 0$. In this case, the shifts Δx and Δy that maximize J_{fg} are given by¹⁷:

$$\begin{pmatrix} \Delta x \\ \Delta y \end{pmatrix} = \frac{S_{ff}}{S_{fg}} \begin{pmatrix} S_{xx} & S_{xy} \\ S_{xy} & S_{yy} \end{pmatrix}^{-1} \begin{pmatrix} S_{xg} \\ S_{yg} \end{pmatrix} \equiv \frac{S_{ff}}{S_{fg}} \mathbf{S}^{-1} \mathbf{s}_g. \quad (43)$$

The sums S_{ff} and S_{fg} in Eq. (43) are to be computed using the pixel fractions f_0 . The sums S_{xg} and S_{yg} determine the magnitudes of the subpixel shifts and thus play a role somewhat similar to Sobel or Prewitt edge operators.⁴⁰ (See also an older paper in which the gradients of the search template are used for subpixel searches of image features.⁴⁶) Given the shifts Δx and Δy from Eq. (43), the augmented normalized correlation is given in terms of the nonaugmented value from Eq. (42) by:

$$J_{fg}^* = J_{fg} + \frac{1}{S_{fg}} (\mathbf{s}_g \bullet \mathbf{S}^{-1} \mathbf{s}_g) \geq J_{fg} \quad [\text{because } \text{Det}(\mathbf{S}) \geq 0]. \quad (44)$$

In the presence of noise, the rms variance of the shifts Δx and Δy may be estimated from the computed maximum correlation values as:¹⁷

$$\delta x^2 = \frac{S_{ff}}{N-1} (1 - J_{fg}^*) (\mathbf{S}^{-1})_{xx}, \quad \delta y^2 \text{ likewise}, \quad (45)$$

where N is the number of pixels in the template. Note that perfect correlation ($J_{fg}^* = 1$) implies perfect centering. The results from Eqs. (43) through (45) can be generalized for $S_{fx} \neq 0$, $S_{fy} \neq 0$ (see Ref. 17), as is the case during the iterative centering loop of Steps 10 through 14 in Fig. 42.

5.5 APPLICATION TO BINARY SCENES

In this section the discussion turns from the material in Ref. 17 to discuss the application of AT-based template matching to image data taken in large-scale, transonic wind tunnels at AEDC and at NASA Ames Research Center. In both facilities, subscale models of flight vehicles are tested that are nominally 6 ft in size. Cameras are mounted at a distance of about 8 ft. Data from three tests are considered here (see Table 7). The first two are pressure-sensitive paint (PSP) tests; the third is a model attitude test.

Table 7. Parameters for Wind Tunnel Tests Considered in This Study

	Test I	Test II	Test III
Type of Test	PSP	PSP	Model Attitude
Test Article	F-16C	F-16C	Model Sting
Test Center	AEDC	NASA Ames	AEDC
Imaged SR Definition	Good	Good	Various
Avg. Imaged SR Diameter, pixels	2.6	5	13
Number of SRs in Study	1163	479	3009
Detected SRs using AT, percent	96.4	92.9	74
Detected SRs using CAT, percent	> 99.7	> 99.7	> 99.7

5.5.1 Pressure-Sensitive Paint Tests

Figure 27 shows a sample CCD image from Test I.³ Images from such a PSP test are converted to surface pressure maps by exploiting the principle of oxygen quenching of fluorescence from a dye in the painted surface.¹ Processed data from up to eight cameras are mapped to a 3D grid of the test article. To accomplish this, small, circular targets are applied to the test article. Automatic image registration is used to track these targets with subpixel accuracy.¹⁶

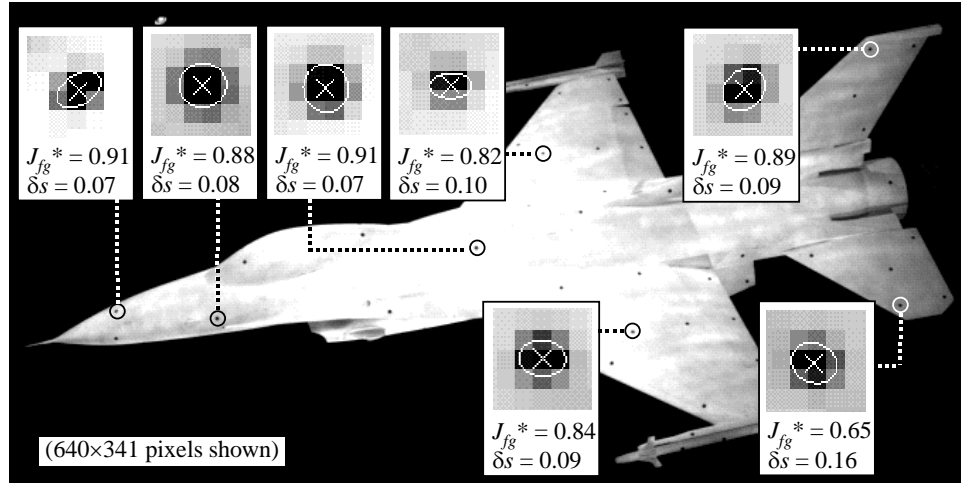


Figure 27. Demonstration of AT-Based SR Detection and Centering for Test I of Table 7

At the heart of the tracking algorithm, AT search templates are computed for each SR based on the following five pieces of information (see Section 4.5): (1) the physical coordinates of the SR at a reference orientation of the test article, as measured using a coordinate-measuring machine; (2) the physical diameter of the SR; (3) the surface normal of the SR at the chosen reference orientation; (4) the estimated position and orientation of the test article based on the tunnel-supplied pitch and roll angles of the model; and (5) the calibrated positions and orientations of the cameras with respect to the wind tunnel, as well as their internal parameters. Photogrammetry is used to relate 2D image coordinates to 3D physical coordinates.^{15,28} Insets in Fig. 27 show some of the detected SRs for Test I along with augmented correlation values J_{fg}^* and estimated centering precisions $\delta s \equiv (\delta x^2 + \delta y^2)^{1/2}$ from Eq. (45), in image pixels.

In the wind tunnel application, actual accuracies of the SR centering determinations are known only as rms deviations between measured and fitted SR centers for all SRs combined (see Section 5.10). These deviations are typically in the range from 0.3 to 0.8 pixels rms but include effects of model deformation under air loads, errors in initial measurement of the physical coordinates of the SRs, and camera calibration errors, if any. Even so, use of the AT technique in Tests I and II resulted in successful detection of 96 and 93 percent, respectively, of the imaged SRs. (For Test I, an earlier search algorithm based on centroiding achieved only a 92-percent success rate.) Best performance of the AT algorithm was obtained, particularly for small SRs, by including a one-pixel-wide skirt around the minimum bounding box of a projected SR, as shown in Fig. 24.

Figure 28 shows average convergence rates for the AT-based centering loop from Fig. 26 (steps 10 through 14) for Tests I and II. The plotted quantity is the ratio of the calculated step size, $(\Delta x^2 + \Delta y^2)^{1/2}$, to the computed precision, $(\delta x^2 + \delta y^2)^{1/2}$, at each iteration. (Iteration zero corresponds to the initial search step on the left side of Fig. 26; the calculation of the precision for this initial step is not shown in Fig. 26.) Figure 28 shows that a few iterations of the centering loop suffice to determine the subpixel location of an SR to within the achievable resolution, given the noise level of the data.

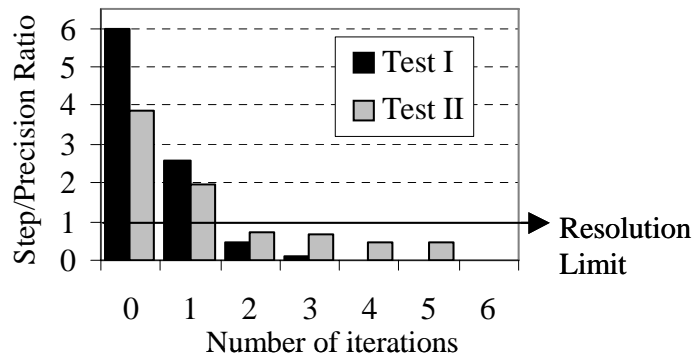


Figure 28. AT-Based Convergence Rates of Centering Loop in Fig. 26

5.5.2 Model Attitude Tests

Figure 29 shows an image taken from Test III in which both black and retroreflecting targets were used as SRs. From the perspective of image registration, Test III differs from Tests I and II primarily in the fact that imaged SRs suffer from a range of deviations from pure binary imaging because of specular reflection, mixed image contrast, and occlusions. Using the AT scheme, only 74 percent of SRs were detected. Sections 5.6 and 5.7 demonstrate how the AT technique can be extended to handle such cases more effectively.

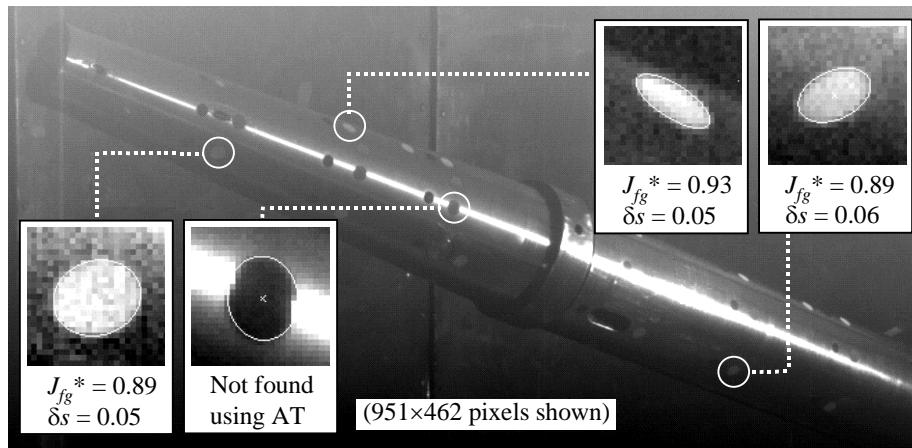


Figure 29. Image from Test III of Table 7, with SRs Detected by the AT Scheme

Figure 30 shows an image of an 18-in. calibration plate that was used as part of Test III. For this plate, physical coordinates of the SRs were known with high accuracy (better than 0.1 mm), and model deformation is not an issue. In this case, rms deviations between measured (i.e., AT-based) image coordinates and fitted coordinates are about 0.05 image pixels (see Table 8). Table 8 also shows good agreement between the predicted precisions from Eq. (45) and the rms fit errors from Section 5.10. This result shows (as is also seen in Section 5.7) that Eq. (45) is, indeed, a useful measure of the accuracy of SR image coordinates at the end of the centering loop in Fig. 26.

5.6 EXTENSION TO NONBINARY SCENES: THEORY

To apply the AT technique to imperfectly rendered binary SRs, allowance must be made for the fact that there is no single gray-level transformation for the SR as a whole.⁴⁷ However, the template may be

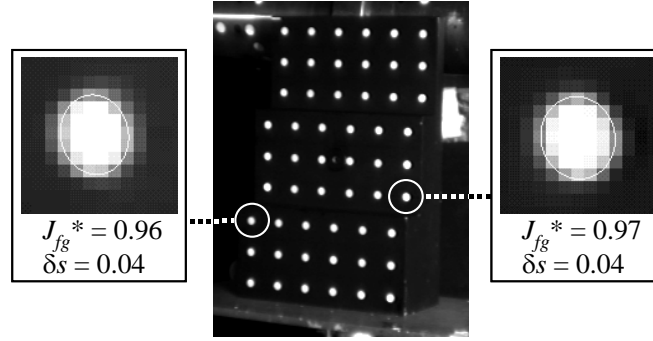


Figure 30. Image of Calibration Plate in Test III with SRs Detected by the AT Scheme

Table 8. Comparison of Centering Errors for Calibration Plate in Test III of Table 7

	Camera 1	Camera 2
Avg. Image Contrast (% of Peak Signal)	High (76%)	High (95%)
Avg. Imaged SR Diameter, pixels	6	9
Avg. Predicted Precision (x, y combined), pixels	0.06	0.06
Avg. Rms Fit Error (x, y combined), pixels	0.05	0.04

divided into subtemplates (see Fig. 31), each of which satisfies (at least approximately) a gray-level transformation. Now a composite sum of squared differences (CSSD, cf. Ref. 48) between template and scene can be defined as follows (see Section 5.11):

$$\text{CSSD} \equiv \sum_k (S_{kff} S_{kgg} - S_{kfg}^2), \quad (46)$$

where the sum over k extends over each of the subtemplates that make up the template as a whole. The correlation sums S_{kff} , S_{kfg} , and S_{kgg} are defined as in Eq. (42), but for each subtemplate k individually. For example, $S_{kfg} \equiv \Sigma (g - \langle g \rangle_k)^2$, where averaging and summation extend only over that part of the scene that corresponds to a particular subtemplate. From Eq. (46), the composite normalized correlation can be computed as

$$J_{fg} \equiv 1 - \text{CSSD} / \sum_k S_{kff} S_{kgg} = \sum_k S_{kfg}^2 / \sum_k S_{kff} S_{kgg}, \quad (47)$$

with $0 \leq J_{fg} \leq 1$. It is shown in Section 5.11 that the CSSD from Eq. (46) (and hence the ensuing correlation) is especially sensitive to pixels near the edge of the SR.

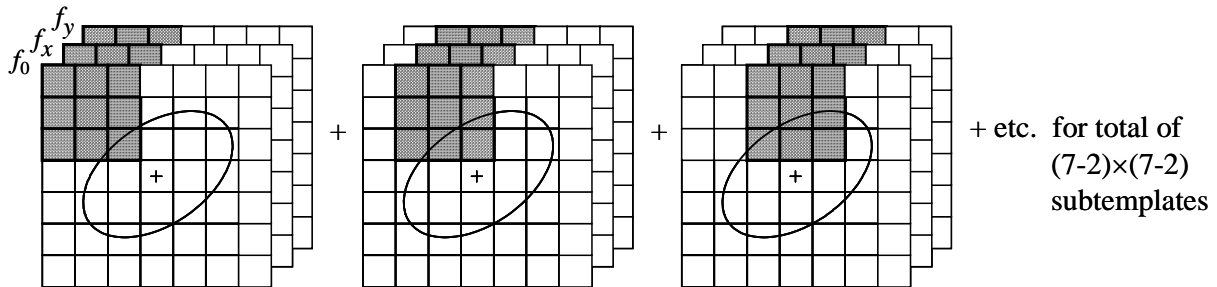


Figure 31. Division of Search Template into Subtemplates

To apply the AT concept to a composite template, it is possible to follow the approach taken in Section 5.4 and substitute the AT expansion from Eq. (40) directly into Eq. (47). However, a more tractable problem is obtained by substituting the AT expansion into Eq. (46) and minimizing the CSSD instead. This leads to subpixel shifts Δx and Δy given by

$$\begin{pmatrix} \Delta x \\ \Delta y \end{pmatrix} = - \begin{pmatrix} D_{xx} & D_{xy} \\ D_{xy} & D_{yy} \end{pmatrix}^{-1} \begin{pmatrix} D_{fx} \\ D_{fy} \end{pmatrix} \equiv -\mathbf{D}^{-1} \mathbf{d}_f, \quad (48)$$

where

$$D_{pq} \equiv \sum_k (S_{kpq} S_{kgg} - S_{kpg} S_{kqg}), \quad p = f, x, y, \quad q = x, y. \quad (49)$$

The subtemplate sums S_{kxg} , S_{kyg} , S_{kxx} , S_{kxy} , S_{kyy} , S_{kfx} , and S_{kfy} are defined analogously to their counterparts in Section 5.4, e.g., $S_{kfx} \equiv \sum (f_0 - \langle f_0 \rangle_k)(f_x - \langle f_x \rangle_k)$, with $\langle f_x \rangle_k \neq 0$ in this case. The augmented correlation value is now given in terms of the nonaugmented value from Eq. (47) by [cf. Eq. (44)]:

$$J_{fg}^* = J_{fg} + (\mathbf{d}_f \bullet \mathbf{D}^{-1} \mathbf{d}_f) / \sum_k S_{kff} S_{kgg} \geq J_{fg} \quad [\text{because } \text{Det}(\mathbf{D}) \geq 0]. \quad (50)$$

In the presence of noise, the rms variance of the shifts Δx and Δy may again be estimated from the augmented correlation values [cf. Eq. (45), though additional approximations are required in the present case], yielding:

$$\delta x^2 = \frac{\sum_k S_{kff} S_{kgg}}{N-1} (1 - J_{fg}^*) (\mathbf{D}^{-1})_{xx}, \quad \delta y^2 \text{ likewise}, \quad (51)$$

with N being the number of pixels in the template. To distinguish results based on the use of a composite template from those based on a noncomposite template, the acronym CAT (composite AT) is introduced for the former.

5.7 EXTENSION TO NONBINARY SCENES: PRACTICE

Different tiling strategies were investigated for subdividing search templates in cases where correlation matching based on the AT scheme from Sections 5.4 and 5.5 failed. Of these tilings, fully overlapping 3 by 3 subtemplates (the case shown in Fig. 31) were found to give a satisfactory compromise between ease of implementation and performance, though this tiling choice may not be optimal for all applications. Redundancy introduced by selecting overlapping subtemplates appeared to benefit detection of poorly defined SRs, though at the expense of higher computational cost as compared to nonoverlapping 3 by 3 subtemplates. Subtemplates of size 2 by 2 were found to give unsatisfactory performance for poorly rendered SRs.

Implementation of the CAT scheme was accomplished by a small modification of the flowchart from Fig. 26. Initially, the SR search is performed using the noncomposite AT scheme from Sections 5.4 and 5.5. Only if this scheme fails to detect the desired SR is the CAT scheme applied. This is done by repeating Steps 3 through 9 in Fig. 26, using the CAT-based correlation expressions for J_{fg} from Section 5.6. Once the SR is found, the centering loop in Steps 10 through 14 of Fig. 26 is performed for the scheme that successfully produced the SR, i.e., either AT or CAT. Typical values for the threshold parameters from Fig. 26 were $J_{\min} = 0.50$, $\Delta s_{\max} = 1$ (pixel), and $J_{\min}^* = 0.75$.

Applying the CAT scheme to the data from Table 7 increased the fraction of detected SRs to above 99.7 percent for each of Tests I, II, and III. Especially for Test III, this is a significant improvement over the AT scheme (which detected only 74 percent of all targets, as shown in Table 7). Figure 32 shows targets from Test III that were detected using the CAT scheme (but missed by the AT scheme), with associated correlation values and estimated localization precisions. Even an SR that is occluded almost

completely (Fig. 32d) is found correctly by the CAT algorithm. Likewise, Fig. 33 shows a few SRs from Tests I and II that were detected by CAT but missed by AT because of extremely oblique viewing angles. Convergence rates for CAT centering was found to be similar to the AT case in Fig. 28.

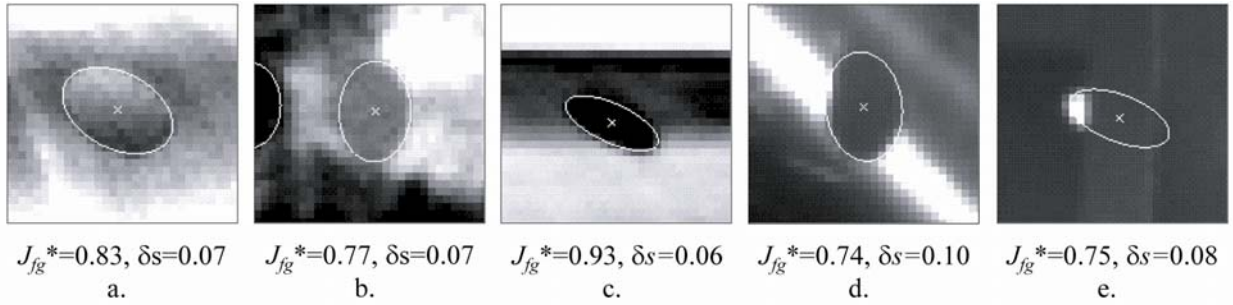


Figure 32. Detected SRs from Test III Found Using the CAT Scheme

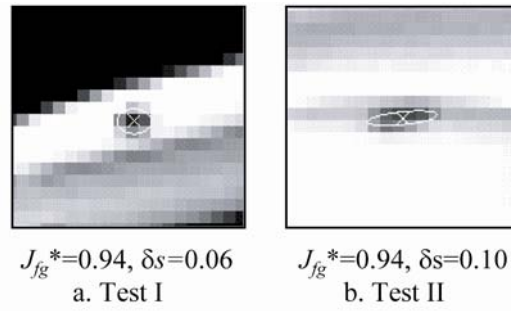


Figure 33. Detected SRs from Tests I and II Found Using the CAT Scheme

Figures 34 through 36 show further comparisons between AT and CAT for SRs that were detected using both schemes. Data points represent average values taken over all detected SRs. As expected (Fig. 34), CAT generally produces higher correlation values than does AT, particularly for imperfectly rendered SRs (for example, SRs with AT correlations below about 0.95). Still (see Fig. 35), the calculated precisions of the resulting centering determinations based on Eqs. (45) and (51) are roughly equal for the two schemes, indicating that the calculated precisions are mutually consistent.

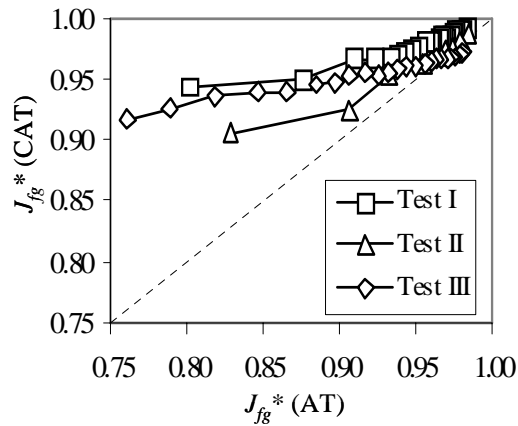


Figure 34. Comparison of AT and CAT Correlation Values

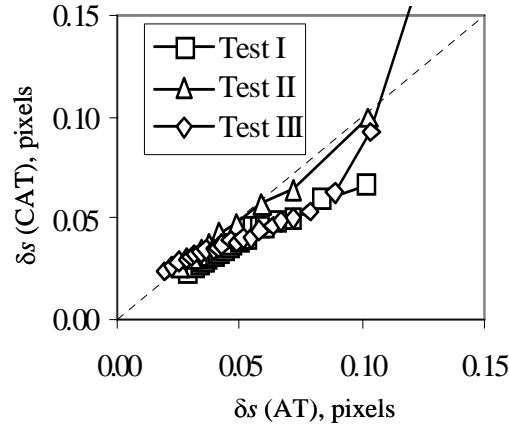


Figure 35. Comparison of Predicted Centering Precisions for Data from Fig. 34

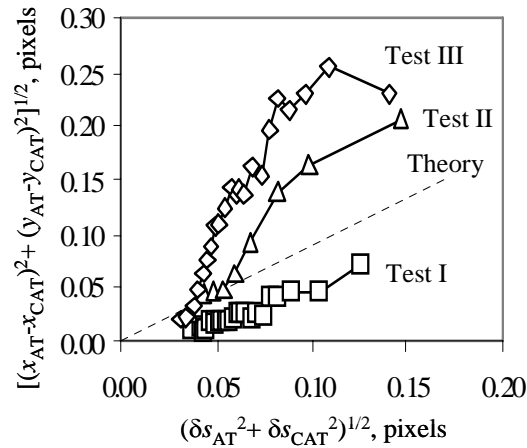


Figure 36. Comparison of Measured and Predicted Precisions for Data from Fig. 34

Actual (“truth”) image centers were not available. Nevertheless, to assess how well Eqs. (45) and (51) predict the actual centering errors, the magnitude of the difference between AT-based and CAT-based image centers is plotted in Fig. 36 as a function of the estimated rms difference based on those two equations. A theoretical simulation with Gaussian noise (the dashed line marked “Theory” in Fig. 36) suggests a slope of 0.885 between these two quantities. Observed slopes for Tests I, II, and III are roughly 0.5, 1.4, and 2.1, respectively. Figure 36 thus suggests that the predicted precisions based on Eqs. (45) and (51) provide a reasonable estimate of the actual accuracy of the calculated target centers.

5.8 CONCLUSION

The augmented template scheme, developed in Ref. 17 for binary image features, has been demonstrated successfully in practice, showing that it is possible both to find the centers of SRs to subpixel accuracy and to estimate the precisions of the computed center coordinates from the associated correlation values. In particular, it has been demonstrated that the AT technique can be extended to imperfectly rendered binary features by dividing the search template into a set of overlapping subtemplates, leading to a composite AT (i.e., a CAT) scheme. Using a combination of AT and CAT search templates, a detection rate of better than 99.7 percent was demonstrated for circular targets that are used for automatic image registration for pressure-sensitive paint measurements and model attitude measurements on scale models of flight vehicles in wind tunnels. This detection rate is particularly impressive for those cases in which experimental artifacts such as specular reflection, mixed image contrast, and occlusions preclude the use

of normalized correlation per se. The AT and CAT schemes should be broadly applicable in other applications in which synthetic references are used for optical tracking.

5.9 ACKNOWLEDGMENTS

Daryl Sinclair and Marvin Sellers provided assistance with aspects of this work. High Technology Corporation and NASA Langley Research Center made available the calibration plate shown in Fig. 30. Dr. Steven Chodos of Boeing-SVS, Inc., brought Ref. 46 to the author's attention.

5.10 APPENDIX A: GLOBAL RMS FIT ERROR

Let (x_i, y_i) denote one of N visible target locations in the image. To check whether the N image coordinates (x_i, y_i) are consistent with the corresponding rigid-body coordinates of the targets (which are measured initially using a coordinate-measuring machine), a projective transform fit of the N target locations is performed.¹⁵ Let (u_i, v_i) denote the fitted image coordinates. The rms fit error can now be defined as

$$\text{rms} \equiv \left\{ \frac{1}{N} \sum_{i=1}^N \left[(x_i - u_i)^2 + (y_i - v_i)^2 \right] \right\}^{1/2}. \quad (52)$$

This rms fit error (expressed in image pixels) serves as a figure of merit for all targets combined, though it includes the effects of imperfect pretest determination of the 3D rigid-body coordinates of the targets, deformation of the test article caused by air loads, and camera calibration errors, if any.

5.11 APPENDIX B: JUSTIFICATION OF COMPOSITE SIMILARITY MEASURE

To justify the use of Eq. (46) as a similarity measure, one can divide the template into a set of subtemplates k and assume that each is rendered by a strict gray-level transformation into the scene, according to $g - \langle g \rangle_k = c_k (f - \langle f \rangle_k)$, where c_k is the local contrast of the k -th subtemplate. The following (with W_k to-be-defined weight factors and pixel sums ij extending over subtemplates k individually) is then a measure of the mismatch between scene and template:

$$\begin{aligned} \text{CSSD} &\equiv \sum_k W_k \sum_{ij \in k} \left[g_{ij} - \langle g_{ij} \rangle_k - c_k (f_{ij} - \langle f_{ij} \rangle_k) \right]^2 \\ &= \sum_k W_k [S_{kgg} - 2c_k S_{kfg} + c_k^2 S_{kff}]. \end{aligned} \quad (53)$$

For fixed weights W_k , the CSSD from Eq. (53) is minimized when $c_k = S_{kfg}/S_{kff}$, leading to

$$\text{CSSD} \equiv \sum_k \frac{W_k}{S_{kff}} [S_{kff} S_{kgg} - S_{kfg}^2]. \quad (54)$$

To obtain an expression that, when substituting the AT expansion from Eq. (40), gives rise to a linear minimization problem in the subpixel shifts Δx and Δy , it is desirable to remove the factors S_{kff} from the denominators in Eq. (54). This is accomplished by setting the weights W_k equal to S_{kff} , leading to the CSSD from Eq. (46). This choice of weights has the additional advantage that the composite similarity measure from Eqs. (53) and (46) is weighted preferentially toward parts of the SR with large values of S_{kff} , (i.e., toward subtemplates near the edge of the SR).

6.0 IMPROVED DATA PROCESSING FOR PRESSURE-SENSITIVE PAINT MEASUREMENTS IN AN INDUSTRIAL FACILITY^{*}**

6.1 OVERVIEW

In this section, six improvements, which give rise to eleven benefits, are described that have been implemented at AEDC to improve the performance of the processing scheme from Section 2.0 of this report for data reduction of PSP images from AEDC's 16-ft Transonic Wind Tunnel (16T). The improvements involve a modification of the order of the main processing steps, improved mapping of 2D image data to the 3D grid of the test article, averaging camera views as opposed to selecting the best view, and the implementation of two additional diagnostics (pixel-based and camera-based) to assess the precision of the processed data. Results of the improvements are illustrated for a PSP test on a scale model of the NASA Space Shuttle in launch configuration, in which AEDC's new, eight-camera, lifetime-based PSP system was used to acquire the data.

6.2 INTRODUCTION

Pressure-sensitive paint (PSP) is a technology that is finding increased use for measuring full-field pressure distributions on test articles in wind tunnels. In short, a luminescent paint is applied to the test article, which is illuminated with short-wavelength (for example, blue) light and fluoresces at a longer wavelength (for example, red). Because of oxygen quenching of excited probe molecules in the paint, the luminescence signal is dependent on pressure, thereby forming the basis for a pressure measurement.

The principles of PSP have been reviewed extensively elsewhere (see, for example, Ref. 1), and the first book dedicated to the subject has recently appeared.⁴⁹ This is not to say that PSP has reached the end of its development cycle. Indeed, efforts are still ongoing around the world (e.g., in Canada,⁵⁰ Japan,^{51,52} Korea,⁵³ United Kingdom,⁵⁴ Germany,⁵⁵ France,⁵⁶ as well as in the U.S.⁵⁷⁻⁶¹) to improve the technique and expand its areas of applicability.

Among these efforts is the one described in this paper: to further improve data processing of PSP images from a large-scale facility such as Tunnel 16T at AEDC. Much progress has already been reported in this regard,^{18,62} but it is shown here that additional improvements have still been possible.

The organization of this section is as follows: In Section 6.3, the status of PSP data processing prior to the current effort is reviewed. Section 6.4 discusses six improvements to this prior status, giving a total of eleven new benefits, including two new diagnostic measures to judge the precision of a PSP measurement. Section 6.5 illustrates the results of these improvements for a PSP test on a scale model of the NASA Space Shuttle. Section 6.6 concludes with a discussion.

6.3 REVIEW OF PRIOR PROCESSING SCHEME

In essence, a PSP measurement consists of a measurement of two or more signals whose ratio or combination of ratios defines the pressure by way of an appropriate calibration function. In the case of the lifetime-based PSP system employed at AEDC, the two signals are both acquired following pulsed illumination of the paint, but they are acquired at different relative delays with respect to the illumination pulses.⁶³ Let the two signals be denoted S_1 and S_2 , with ratio [See also Eq. (1)]:

$$R \equiv S_1 / S_2 . \quad (55)$$

^{***}W. Ruyten and M. Sellers, "Improved Data Processing for Pressure-Sensitive Paint Measurements in an Industrial Facility," AIAA Paper 2006-1042, 44th AIAA Aerospace Sciences Meeting and Exhibit, Reno, Nevada, January 9-12, 2006.

The pressure, P , is then obtained from this ratio by means of a calibration function, $f(R)$, so that

$$P = f(R) = \sum_{k=0}^{K-1} f_k R^k . \quad (56)$$

Typically, as indicated, the calibration function f is a polynomial whose coefficients, f_k , are determined by either *a priori* or *in situ* calibration (or a combination of the two). Typical numbers of coefficients, K , are three to five. The coefficients f_k , in turn, depend on temperature and are computed on the basis of the best available estimate of the temperature of the surface of the test article.

Calculation of the signal ratios and conversion of the ratios to pressure by way of a polynomial calibration equation are mathematically simple, even given the fact that these calculations must be performed on images. Much harder is the challenge of automating the process whereby image data are mapped to a three-dimensional (3D) grid of the test article. However, significant progress has been made in this area, allowing online processing of PSP image data from up to eight cameras to be performed within ten seconds of acquiring the data.^{18,62}

Figure 37 illustrates key steps in the overall data reduction process: 1) Performing a smoothing operation on the raw image data; 2) taking the ratio of two images for each camera; 3) converting the ratio to a pressure by application of the calibration function from Eq. (56); 4) mapping the resulting pressure distribution to the 3D grid for each camera individually; and 5) merging data from multiple cameras to obtain the final result. In this merge process, the best (most normal) camera view is selected for each point on the surface, and calibration offsets are applied between cameras, to achieve optimum matching of calculated pressures along boundary lines between adjacent camera views.

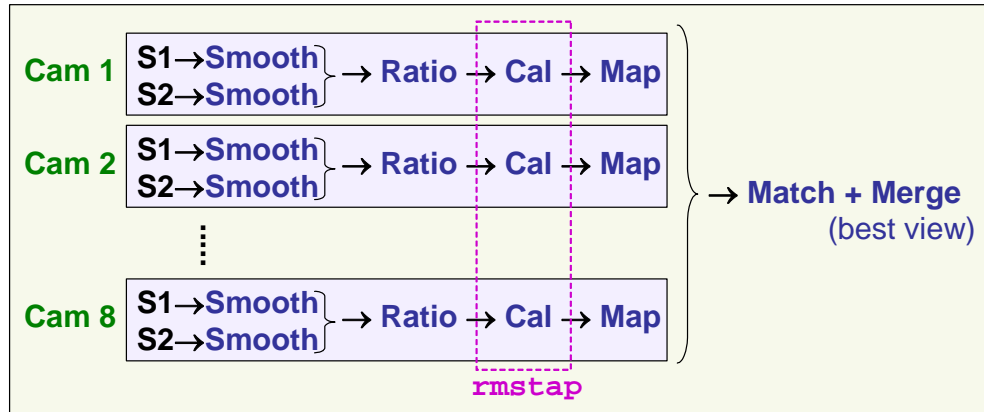


Figure 37. Key Processing Steps Prior to Improvements

Not shown in Fig. 37 are 1) subtraction of black images to adjust for nonzero signals at zero illumination; 2) thresholding of the signals before calculation of the image ratios; 3) image registration, whereby the mapping transformation is established between 2D image coordinates and 3D model coordinates; 4) interpolation of pressure data across areas of missing data (particularly across registration targets); 5) *in situ* correction of the measured PSP pressures based on measurements from discrete sensors embedded in the test article; and 6) self-illumination correction for reflected emission light.²¹

The reason these additional steps are not shown in Fig. 37 is not that they are not important, but rather to focus the present discussion on those steps in the processing sequence to which improvements were made, as discussed in Section 6.4.

Also indicated in Fig. 37 is the calculation of a diagnostic measure, “rmstap,” defined as the rms difference between the PSP image data in the vicinity of pressure taps and the pressures measured by the

taps. So far, this has been one of the few diagnostics available to judge the accuracy of a PSP measurement. Two additional diagnostics are introduced in Section 6.4.

6.4 IMPROVEMENTS TO PROCESSING SCHEME

Figure 38 shows the new processing sequence, showing, as in Fig. 37, only those steps to which changes were made relative to the scheme discussed in Fig. 37. The new sequence of steps is as follows: 1) Signal ratios are calculated prior to smoothing; 2) the ratios are mapped to the 3D grid prior to conversion to pressure, while smoothing the data by interpolation; 3) ratios from all cameras are merged onto a single 3D grid; and 4) the ratios on the 3D grid are converted to pressures based on the calibration function from Eq. (56). In addition, two additional diagnostics are computed in Fig. 38, and are denoted “rmspix” and “rmscam.”

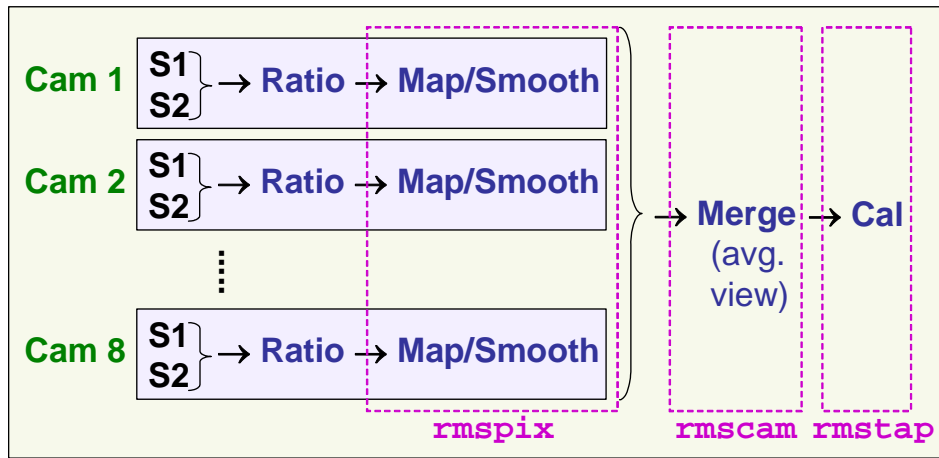


Figure 38. Improved Processing Sequence

The changes in processing between Figs. 37 and 38 constitute six improvements and provide a total of eleven benefits. These are explained in detail in the following paragraphs

Improvement #1: Smoothing After Ratioing

Typical smoothing operations in the past have involved taking a 3 by 3 or 5 by 5 pixel running average (with outlier rejection) on the black-subtracted images to reduce the effects of photon shot noise. This process was satisfactory for the old intensity-based PSP system,³ but it was found to introduce additional noise for the current lifetime-based system. The reason for this seems to be that the current cameras (see Section 6.5) have significant pixel-to-pixel gain variations. Improvement #1 accrues the following benefit:

Benefit #1: Ratioing before smoothing compensates more fully for pixel-to-pixel gain variations of the cameras, and thus reduces the noise level in the processed data (by about a factor of three).

Improvement #2: Smoothing as Part of Mapping

Rather than performing the smoothing operation immediately following calculation of the signal ratios, smoothing is now implemented in the form of an interpolation scheme that is an integral part of the mapping process. This scheme is explained in Fig. 39, which shows a small part of the 3D grid projected (for a given camera view) onto the 2D array of image pixels. To obtain the mapped image value (in the case of Fig. 38, a signal ratio) at a grid point g , the values from pixels surrounding the projected grid point g are interpolated onto the grid point, as explained in Section 6. This improvement accrues the following benefits:

Benefit #2: Smoothing at the mapping stage is faster than smoothing image data prior to mapping because there are typically fewer points on the 3D grid than there are pixels in the images.

Benefit #3: Smoothing at the mapping stage in the form of interpolation preserves subpixel resolution of the mapped data, as explained in Section 6.8.

Benefit #4: Smoothing at the mapping stage allows the use of depth-buffer masking to exclude image pixels that are close to a projected grid point in 2D image space, but not in 3D model space. (A depth buffer is calculated as an integral part of the mapping transformation even in the old processing scheme.) In particular, depth-buffer masking prevents interpolation across the edges of the test article in the image.

Benefit #5: While not yet implemented, smoothing at the mapping stage should allow for optimum matching of the projected grid resolution to the pixel spacing in the image. That is, a coarse grid (in projection) would justify a larger number of pixels in the smoothing operation than would a fine grid.

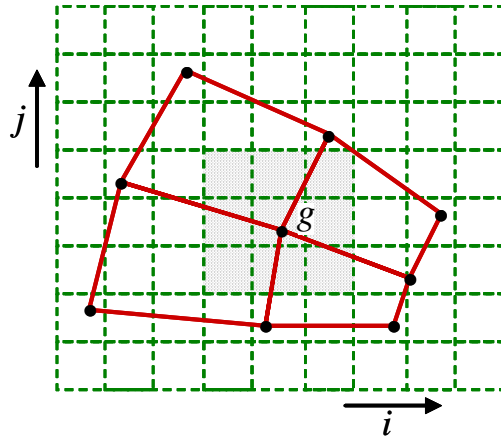


Figure 39. Schematic of Mapped Grid Projected onto Image

Improvement #3: Calibration After Mapping During Merge

In Fig. 38, the conversion of signal ratios to pressures by way of the calibration function from Eq. (56) is not performed until after the data (in this case, signal ratios) have been mapped to the 3D grid for each camera, and ratios from multiple cameras have been merged onto a single 3D grid. This improvement accrues the following benefits:

Benefit #6: The problem of performing *in situ* calibrations for camera views that involve few or no pressure taps is avoided.

Benefit #7: A single calibration can be applied for the entire surface of the test article. In particular, there is no need to calculate calibration offsets for overlapping cameras, as is indicated in Fig. 37 by the term “match.”

Improvement #4: Average vs. Best View in Merging

When parts of the test article are imaged by more than one camera, the question arises of how data from multiple cameras need to be handled. Traditionally, data from only a single view has been retained, namely the one most normal to the surface. In the case of the AEDC PSP system, this is a significant issue because eight cameras are typically employed in the test section, as shown in Fig. 40. This means that many parts of the test article are viewed by three or four cameras.

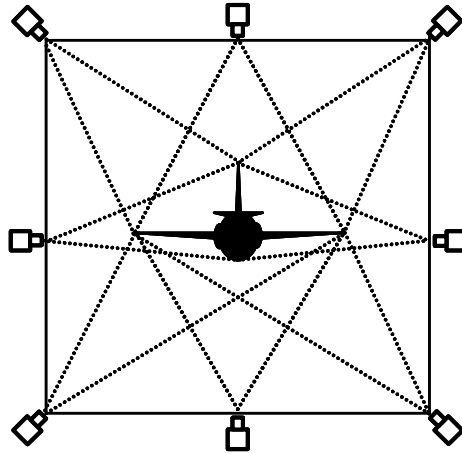


Figure 40. Schematic of Eight-Camera PSP System

In the new scheme, data from overlapping cameras are averaged on the basis of viewing angle, as explained in Section 6.9. From this improvement accrue the following benefits:

Benefit #8: The effects of photon shot noise are reduced because, effectively, more photons are collected in the measurement scheme.

Benefit #9: Systematic errors in camera overlap regions (though small—see Section IV) are smoothed out, practically removing the appearance of seams from the mapped data.

Improvement #5: Pixel-Based Measurement Precision

As mentioned at the end of Section 6.3, the sole diagnostic that has typically been reported for PSP data in the past is the rms difference between the PSP image data in the vicinity of pressure taps and the pressures measured by the taps. In Fig. 38, two additional diagnostics are indicated. The first of these is a measure of the effect of pixel-to-pixel noise in the images. Section 6.8 explains how this pixel-based diagnostic, rm_{spix} , is computed. This additional diagnostic accrues the following benefit:

Benefit #10: The rm_{spix} diagnostic provides a measure of the precision of the PSP data. In particular, it reveals how closely the noise level approaches the theoretical limit, as determined by photon shot noise. This is discussed further in Section 6.5.

Improvement #6: Camera-Based Measurement Precision

The second additional diagnostic in Fig. 38 involves the calculation of the level of disagreement between multiple camera views for those points on the surface of the test article that are viewed by more than one camera. Section 6.9 explains how this camera-based diagnostic, rm_{scam} , is computed. This additional diagnostic accrues the following benefit:

Benefit #11: The rm_{scam} diagnostic provides a check on the implicit assumption in PSP measurements that the physical process by which excitation light is converted to emission light does not have a view-angle dependence, and that no other view-dependent effects (such as a combination of specular reflection of excitation light and spectral leakage in the measurement process⁶⁴) remain unaccounted for.

Before moving on to a discussion of experimental results in Section 6.5, it should be noted that all of the improvements discussed in Section 6.4 might be applied, in principle, to an intensity-based PSP measurement. However, one of the practical limitations of an intensity-based system is that the test article experiences a model shift between wind-off and wind-on measurements because of sting bending under

aerodynamic loads.⁶⁵ This limitation necessitates a separate alignment step between the two images that make up the ratio in Eq. (55). Even then, residual errors remain because a model shift produces changes in the illumination distribution. By contrast, in the current lifetime-based PSP system, the image pairs that make up the signal ratios in Eq. (55) are both obtained at run conditions, and the complications caused by model shifts are avoided.

A final comment pertaining to the changes in processing scheme concerns the software that was used to implement the changes. Prior to this effort, most PSP data processing at AEDC was performed by Green Boot, a program developed jointly by NASA Ames and McDonnell-Douglas Aerospace (i.e., before MDA's acquisition by Boeing). Currently, however, most processing of PSP data at AEDC is performed by the AEDC-developed program BlackBox, so named for its ability to process data with minimal (if any) user interaction, after some initial calibrations have been performed. All of the changes described in Section 6.4 were made in BlackBox. However, the changes described are not really software specific and should be amenable to other software packages.

6.5 SAMPLE RESULTS FOR NASA SPACE SHUTTLE TEST

Most of the improvements in processing methodology described in Section 6.4 were implemented to support a lifetime-based PSP test of a three-percent scale model of the NASA Space Shuttle in launch configuration (i.e., with external tank and solid rocket boosters). This test was performed in October 2004 in the 16-ft Transonic Wind Tunnel at AEDC. Results of this test have been reported elsewhere.⁶⁶ Here we report only on those elements of the test that highlight the improvements in processing methodology.

Image data were acquired with eight Photometrics CoolSNAP K4 interline transfer cameras, each with a spatial resolution of 2048 by 2048 image pixels and a gray-scale resolution of 12 bits, i.e., 0 to 4095 counts per pixel. (For an interesting discussion of camera selection for a PSP measurement system, see Ref. 67.) Processed data were mapped to a 3D grid consisting of 332 zones and 643,555 grid points. More than 1,100 pressure taps were available to compare results from the PSP analysis to conventional measurements. PtTFPP in FIB was used as the paint.⁹ Pulsed illumination was provided by banks of LEDs emitting at 464 nm, pulsing every 600 μ s, and luminescence was filtered at 650 nm. Images were acquired by integrating up to 30,000 pulses at each gate. About 70 circular registration targets were applied to the test article to perform image registration. Data were processed on a Linux cluster consisting of a master and eight slaves, each with two processors. Processing times were on the order of six seconds per test condition. Further details on the AEDC lifetime-based PSP system are discussed in Ref. 68.

Figure 41 shows an example of a processed data point for the test condition indicated. The display color represents pressure, ranging from low (blue) to high (red).

Figure 42 shows the corresponding pixel-based precision r_{mspix} , calculated as shown in Section 4.4. Blue indicates small values of this rms error, while red indicates high values. The distributions in Figs. 41 and 42 are clearly correlated, with better precisions corresponding to low-pressure areas on the model (i.e., areas where the emission signal is the highest). This is the expected behavior for a measurement system in which photon shot noise is the limiting factor.

Figures 43 and 44 show, again for the same data from Figs. 41 and 42, the number of camera views and the camera-based precision r_{mscam} , calculated as shown in Section 6.9. (Recall that r_{mscam} is a measure of the disagreement between multiple camera views for a given point on the test article.)

The distribution in Fig. 44 is essentially the same as that in Fig. 42, though spottier (note that the r_{mscam} diagnostic cannot be computed for points that are viewed by only a single camera). The similarity of the distributions in Figs. 42 and 44 indicates, again, that the main source of error in the data is photon shot noise. In particular, the similarity of the distributions in Figs. 42 and 44 indicates that there are no unexplained view-angle dependencies in the illumination-excitation-emission-detection chain of processes that forms the basis for a PSP measurement.

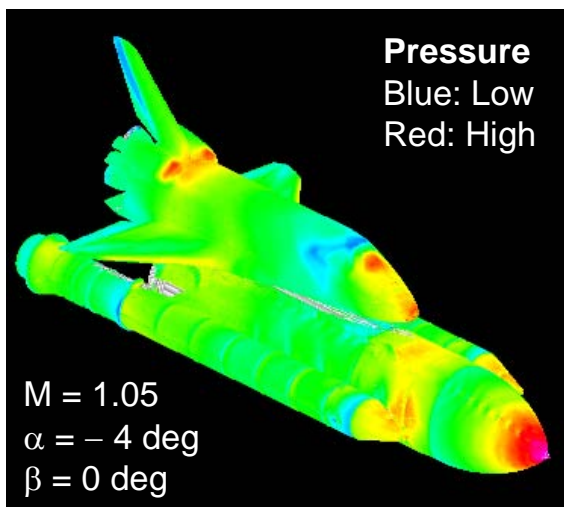


Figure 41. Mapped Pressure Distribution on Space Shuttle Model

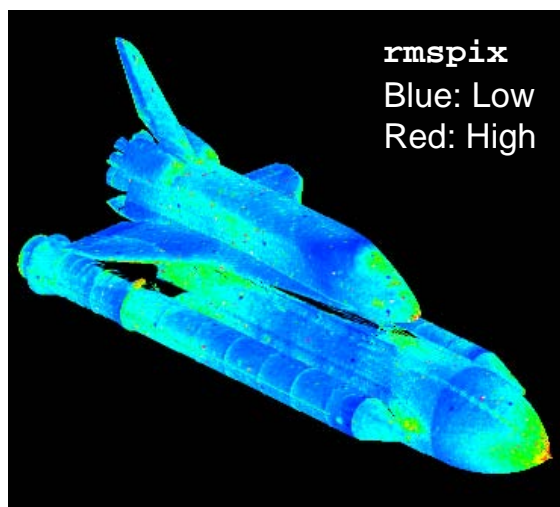


Figure 42. Pixel-Based Precision Associated with Fig. 41

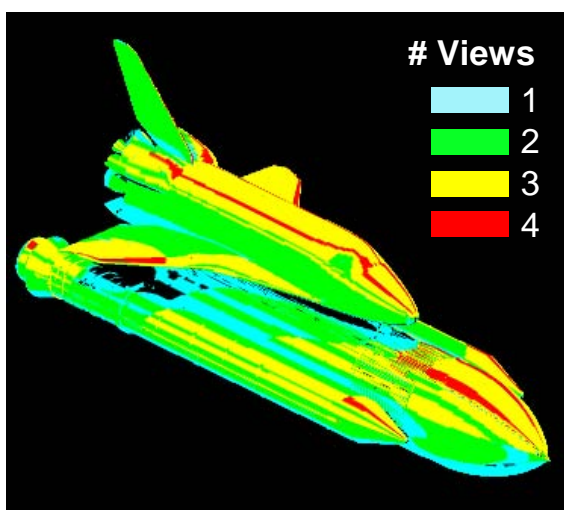


Figure 43. Number of Camera Views for Fig. 41

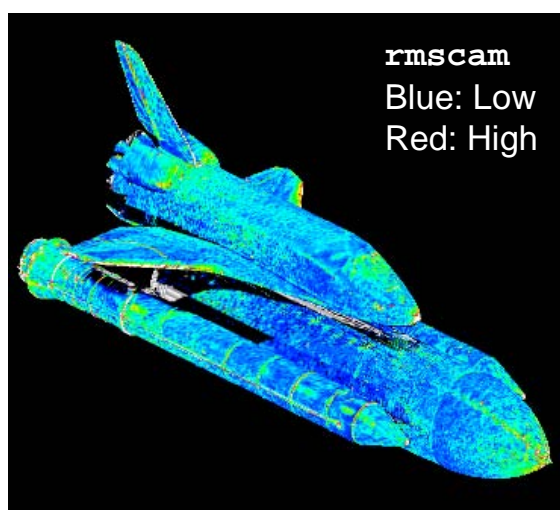


Figure 44. Camera-Based Precision Associated with Fig. 41

Overall, the ratios between the three diagnostic measures employed was found to be on the order of

$$\text{rmspix} : \text{rmscam} : \text{rmstap} \cong 3 : 4 : 8. \quad (57)$$

This result makes sense qualitatively: the pixel-based error should be the smallest because it is essentially a measure of photon shot noise and is least affected by systematic errors such as view factors, uncompensated temperature errors, and other effects. On the other hand, the comparison between paint values and tap values captures all random and systematic errors in the measurement scheme.

As to why the rmstap measure is three times as large as the rmspix value, the reason for this is not clear at this point, but it is suspected that this ratio is uncommonly high because of the geometrical complexity of the test article and the fact that many taps are located in or near corners, where it is not easy to assign a PSP-based pressure value. Indeed, if the rmstap diagnostic is calculated for the best 75 percent of all data (i.e., the PSP data that best match the available taps), the new value of rmstap is on

the order of rm_{scam} . This is a more significant improvement in rm_{spix} than would be expected if the PSP-tap differences were normally distributed (which would leave a new ratio of 5 : 8 vs. 4 : 8 for $rm_{stap} : rm_{scam}$). In other words, the PSP-tap differences are not normally distributed.

Absolute values for rm_{stap} are quoted in Ref. 66 (see, e.g., Fig. 9 in Ref. 66). These values range from 0.5 kPa to 1.3 kPa, depending on test conditions.

Finally, Fig. 45 shows a comparison between the old method of processing data (as described in Section 6.3) and the new method from Section 6.4. This comparison shows that a seam along the boundary line between adjacent camera views in the old scheme is no longer visible in the new result. This is because the new processing scheme employs a weighted camera average rather than selection of a best view, and because per-camera calibration offsets are no longer required since converting signal ratios to pressures does not take place until after the ratios have been mapped onto the 3D grid.

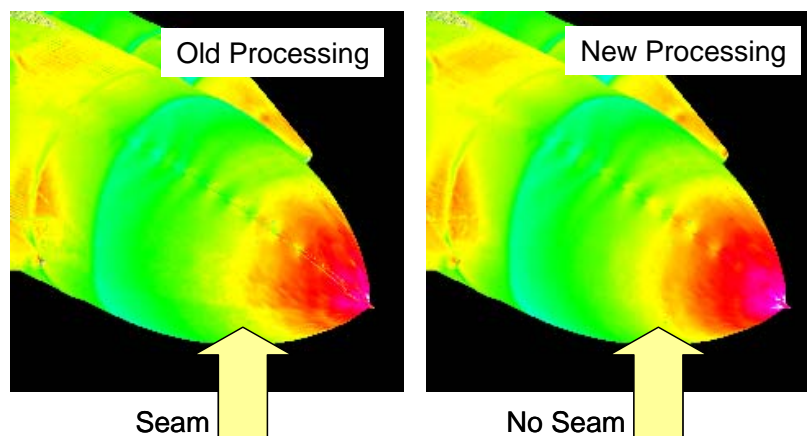


Figure 45. Example of Elimination of Seam Resulting from Improved Processing

6.6 DISCUSSION

It has been shown that AEDC's new lifetime-based PSP system is capable of producing high-quality test data and that these data can be delivered to the test customer in near real time during the PSP test. It has also been shown that a number of improvements in processing methodology have still been possible, with regard to both quality and speed. These changes involve a modification of the order in which the principal processing steps are executed, improved mapping of 2D image data to the 3D grid, and averaging data from multiple camera views as opposed to selecting a best view. In particular, converting signal ratios to pressure only *after* the data have been mapped to the 3D grid has been shown to both simplify the analysis process and improve the final results (for example, the elimination of seams in the processed data where adjacent camera views overlap).

It has also been shown that additional diagnostic information (beyond the conventional comparison of PSP results to pressure taps) may be extracted as part of the image-processing task. In particular, two diagnostic measures, rm_{spix} and rm_{scam} (which measure the precision of the processed data on a per-pixel and a per-camera basis, respectively), have been implemented. These statistics confirm that the precision of the processed data for the current lifetime-based PSP system is governed essentially by photon shot noise. (This statement would not be true for the old intensity-based system.) The important implication of this observation is that it should be possible to further improve the precision and accuracy of the lifetime-based PSP system by increasing the radiant flux of the excitation light. Indeed, plans are in progress to replace the current LED banks with higher brightness LED's that have recently become commercially available.

6.7 ACKNOWLEDGMENTS

This work was funded, in part, by the Test and Evaluation Program of the Air Force Office of Scientific Research, managed by Drs. Neil Glassman and John Schmisser.

6.8 APPENDIX 6A: IMPROVED MAPPING SCHEME

In Fig. 39, assume that the pixel values in the image [representing the signal ratio from Eq. (55)] are given by R_{ij} , where i and j are indices along the axes of the image. Furthermore, assume that the (floating point) coordinates of the projected grid point g are given by (u_g, v_g) and that the coordinates of the centers of the pixels in the vicinity of (u_g, v_g) are given by (u_i, v_j) . Assignment of a mapped value to grid point g may now be thought of as an interpolation scheme among the surrounding pixel values.

To first approximation, the image values $R(u, v)$ for a set of coordinates (u, v) in the vicinity of (u_g, v_g) may be approximated by a bilinear slope of the form

$$R(u, v) = a + b(u - u_g) + c(v - v_g), \quad (58)$$

where a , b , and c are coefficients to be obtained by performing a least-squares fit of Eq. (58) to the measured values, R_{ij} , at the locations (u_i, v_j) . Equation (58) is structured in such a way that the coefficient a yields the desired mapped value with, in principle, subpixel resolution.

Solution of the least-squares problem leads to the linear system

$$\begin{pmatrix} S_1 & S_u & S_v \\ S_u & S_{uu} & S_{uv} \\ S_v & S_{uv} & S_{vv} \end{pmatrix} \begin{pmatrix} a \\ b \\ c \end{pmatrix} = \begin{pmatrix} S_r \\ S_{ur} \\ S_{vr} \end{pmatrix}, \quad (59)$$

where $S_1 = \sum 1$, $S_u = \sum(u_i - u_g)$, $S_v = \sum(v_j - v_g)$, $S_{uu} = \sum(u_i - u_g)^2$, $S_{uv} = \sum(u_i - u_g)(v_j - v_g)$, $S_{vv} = \sum(v_j - v_g)^2$, $S_r = \sum R_{ij}$, $S_{ur} = \sum(u_i - u_g)R_{ij}$, and $S_{vr} = \sum(v_j - v_g)R_{ij}$. All of the sums extend over the same set of pixels (for example, the shaded set of pixels in Fig. 39) to obtain the mapped value (i.e., the value a) at grid point g .

The unbiased sample variance of the bilinear fit may be calculated as

$$\sigma_g^2 = \frac{1}{N-3} \sum_{i,j} [R(u_i, v_j) - R_{ij}]^2 = \frac{1}{N-3} (S_{rr} - aS_r - bS_{ur} - cS_{vr}), \quad (60)$$

where $S_{rr} = \sum R_{ij}^2$ and $N = S_1 = \sum 1$ (i.e., the number of pixels in the sum). The factor $N-3$ reflects the fact that there are three fit coefficients in Eq. (58).

In conjunction with Eq. (56), the variance from Eq. (60) allows the `rmspix` diagnostic from Fig. 38 (for grid point g) to be calculated as

$$(\text{rmspix})_g = \left| \sum_{k=1}^{K-1} k f_k a^{k-1} \right| \sigma_g. \quad (61)$$

For best results, the number of pixels N should not be too small. (For the 2048 by 2048 images used in this work, 5 by 5 regions of pixels were found to give good results.) For completeness it should be noted that other types of mapping are possible, for example, texture mapping.⁶⁹

6.9 APPENDIX 6B: OVERLAPPING CAMERA VIEWS

In the old mapping scheme from Section 6.3, the best view for a grid point g from among multiple camera views c was selected on the basis of the cosine of the viewing angle, given by

$$w_{cg} = (\hat{n}_c \bullet \hat{n}_g) . \quad (62)$$

Here n_c is a normal vector along the line of sight for camera c , and n_g is the surface normal at grid point g . In the old scheme, the view with the largest value of w_{cg} was selected. In the new scheme from Section 6.4, a weighted average is calculated in the case of multiple camera views, according to

$$\bar{R}_g = \sum_c w_{cg}^2 R_{cg} / \sum_c w_{cg}^2 , \quad (63)$$

where the sum is over all camera views c that can include grid point g , and R_{cg} is the signal ratio for grid point g as measured by camera c .

The degree to which the individual ratios R_{cg} vary from the calculated average is another measure of the variance, already expressed in Eq.(60). In the present case, this variance may be computed according to

$$\sigma_g^2 = \frac{1}{N_c - 1} \sum_c w_{cg}^2 [R_{cg} - \bar{R}_g]^2 / \sum_c w_{cg}^2 , \quad (64)$$

where N_c is the number of camera views. The variance from Eq.(64) may be substituted into Eq.(61), this time to obtain the camera-based diagnostic rmscam from Fig. 38.

7.0 ASSIMILATION OF PHYSICAL CHEMISTRY MODELS FOR LIFETIME ANALYSIS OF PRESSURE-SENSITIVE PAINT^{††}

7.1 OVERVIEW

Lifetime analysis techniques from the physical chemistry literature are assimilated for use with lifetime-based PSP measurements. Effects of finite pulse duration and residual fluorescence, typically avoided in physical chemistry, are included through the use of an Excitation Response Function. Three models are reviewed and applied to the fluorescence decay of PtTFPP in FIB, which is the current industry standard for large-scale PSP testing in the U.S. These are the Discrete Exponential Model, the Förster Decay Model, and the Maximum Entropy Model. It is shown how these models invite the reconstruction of the decay rate distribution of the paint from time-resolved measurements of the fluorescence response. Results of the analysis suggest that the decay-rate distribution (and hence the lifetime spectrum) of the paint is bimodal, with each component obeying a linear Stern-Volmer dependence.

7.2 INTRODUCTION

Over the last decade, significant interest has developed in the use of luminescent paints for aerodynamic testing.^{1,2,6} This is particularly true for the use of pressure-sensitive paints (PSPs), which rely on oxygen-quenching of fluorescence to produce a pressure-dependent luminescence signal. To lowest order, this process is described by a Stern-Volmer relation that expresses the fluorescence decay rate, γ , in terms of the pressure, P , as

$$\gamma \equiv \frac{1}{\tau} = \frac{1}{\tau_0} + \kappa_{SV} P. \quad (65)$$

Here τ is the lifetime in air, τ_0 is the lifetime in vacuum, and κ_{SV} is the bimolecular quenching constant in air. Higher order terms are frequently included in Eq. (65), though their origin is usually not well understood.⁷⁰⁻⁷²

In most PSP measurements neither the decay rate, γ , nor the lifetime, τ , is measured directly. Instead, a ratio is formed between images at “wind-off” and “wind-on” conditions when continuous illumination is used, or between images acquired at separate gates following the illumination pulse in the case of pulsed illumination. These two techniques are referred to as intensity-based PSP and lifetime-based PSP, respectively. In both cases, the signal ratio is expressed as a function of pressure by means of a Stern-Volmer-type relation. To use this relationship as the basis for a pressure measurement, one does not necessarily have to have a thorough understanding of the nature of the relationship (for example, linear vs. nonlinear); as long as a suitable calibration can be performed. This approach has been fruitful since the early days of PSP measurements.⁷³⁻⁷⁴

A longstanding complication in PSP measurements is that the signal ratios depend not only on pressure, but also, to some extent, on temperature.^{8,75-77} Recent work on lifetime-based PSP suggests that this unwanted temperature dependence may be turned to an advantage by extending the standard two-gate measurement scheme to one that employs three or four gates.^{10,12,13,51} This allows two signal ratios to be formed. Under suitable conditions, this allows measurement of both pressure and temperature (see Section 9.0).

^{††}Previously published as “Assimilation of Physical Chemistry Models for Lifetime Analysis of Pressure-Sensitive Paint,” *AIAA Journal*, Vol. 43, No. 3, March 2005, pp. 465-471. An earlier (and longer) version of this paper was presented as AIAA Paper 2004-0880, 42nd AIAA Aerospace Sciences Meeting and Exhibit, Reno, NV, January 5-8, 2004.

Questions remain on how to bring such a P - T measurement scheme to fruition. However, it is clear that the fluorescence response of the paint must *not* be single-exponential: multiple measurements on a single-exponential decay would merely recover the same γ or τ in different ways, leaving the P - T ambiguity unresolved. As it turns out, nonsingle-exponential fluorescence decay of PSPs appears to be the rule, rather than the exception (see Refs. 12, 13, 75, and 78 and Section 7.4 of this report). Even so, most PSP analysis to date has been based on single-exponential behavior.^{3,78,79} This approach falls short if the optimization of a multigate, lifetime-based measurement scheme is to be approached from fundamental principles. Instead, it is desirable to start out from the known lifetime characteristics of the paint or (in the case of paint development) from the desired paint characteristics. In particular, it is desirable that these lifetime characteristics be cast in the form of a mathematical model that can serve as the basis for optimization of the operational parameters of a lifetime-based PSP system, for derivation of suitable calibration equations, and for analysis of PSP measurements in general. Such lifetime analysis models have been in use for some time in physical chemistry and associated fields (chemical physics, analytical chemistry, sol-gel physics, and biophysics). The purpose of Section 7.0 is to assimilate some of these models for use with PSP (Section 7.3) and (in Section 7.4) to demonstrate the use of these models for PtTFPP in FIB [Pt(II) meso-tetra(Pentafluorophenyl)porphine in fluoro-isopropyl-butyl], which is the current industry standard for PSP testing in the U.S.^{1,3-5,8,9,80,81}

7.3 LIFETIME MODELS FROM PHYSICAL CHEMISTRY

In Section 7.3.1, the notion of paint as a microheterogeneous system is introduced, leading to a general formulation for the response of such a system to delta-function excitation. In Sections 7.3.2, 7.3.3, and 7.3.4, three specific realizations of this general model are described. Section 7.3.5 deals with the situation in which the width and repetition rate of the excitation pulse can not be neglected. Section 7.3.6 discusses numerical aspects of the reconstruction of the lifetime spectrum of the paint from a time-resolved measurement of the fluorescence signal.

7.3.1 Paint as a Microheterogeneous System

A central notion in the description of quenched fluorophore systems is that not all fluorophore molecules experience the same interaction with the quenching species (in the case of current PSPs, this would be oxygen) and that this heterogeneity exhibits itself on a microscopic scale.⁸²⁻⁸⁶ Such a system may be described by partitioning the fluorophore density, n_f , with respect to the resulting distribution of decay rates, γ , as

$$n_f \rightarrow \int_0^\infty \frac{dn_f}{d\gamma} d\gamma \equiv \int_0^\infty n'_\gamma(\gamma) d\gamma = n_f. \quad (66)$$

That is, n_f is replaced by a distribution function $n'_\gamma(\gamma)$ that has n_f as its area. Equivalently, this partitioning may be described with respect to the lifetime, τ , where $\tau \equiv 1/\gamma$.⁸⁰ The fluorescence response of such a system to delta-function excitation may be expressed as the Laplace transform

$$S_\delta(t) = \int_0^\infty n_\gamma(\gamma) e^{-\gamma t} d\gamma, \quad (67)$$

where $n_\gamma(\gamma)$ is the distribution function $n'_\gamma(\gamma)$ from Eq. (66), multiplied by a constant:

$$n_\gamma(\gamma) \equiv C n'_\gamma(\gamma). \quad (68)$$

The constant C may be written (see Section 7.6) as the product of the area viewed by the detector, the effective thickness of the sample, the excitation photon flux at the surface, the optical cross section for excitation, the quantum efficiency for population of the fluorescing state, the rate of fluorescence decay, the efficiency of detection of emitted fluorescence photons, the detection time, and the number of

excitation pulses over which the signal is integrated.⁸⁰ Implicit in Eq. (68) is the assumption that the excitation process is linear (see Section 7.7).

From Eqs. (66) through (68), it follows that the area under the distribution $n_\gamma(\gamma)$ is given by

$$A \equiv \int_0^\infty n_\gamma(\gamma) d\gamma = S_\delta(0) = C n_f. \quad (69)$$

This area should be independent of quenching, a principle that might be paraphrased as “conservation of implied fluorophore density.”

7.3.2 Discrete Exponential Model

When a single exponential (with to-be-determined amplitude and decay rate) fails to produce a satisfactory fit to fluorescence decay data, it is common practice to add a second, third, and (in rare cases) a fourth term.^{12,51,75} This model is known as the Discrete Exponential Model (DEM) and may be expressed as

$$S_{\delta, \text{DEM}}(t) = \sum_{k=1}^K a_k \exp(-\gamma_k t). \quad (70)$$

The number of components, K , may be assigned on the basis of an *a priori* model (for example, when the components are associated with different fluorophore molecules), or chosen empirically, to get a satisfactory fit to the data. Figure 46 illustrates the associated decay rate distribution for the case $K = 3$. The “area” under this distribution is given by the relation

$$A_{\text{DEM}} = \sum_{k=1}^K a_k. \quad (71)$$

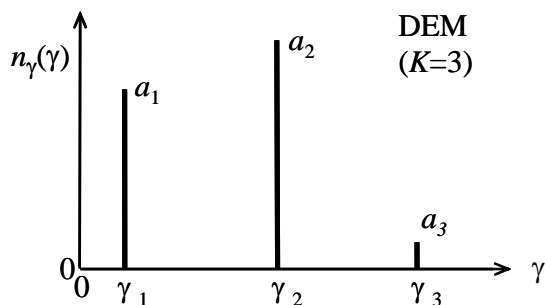


Figure 46. Illustration of DEM Decay Rate Distribution

7.3.3 Förster Decay Model

If the range of interaction distances between fluorophore molecules and quenchers is given by a power-law distribution, the delta-function response of the system may be written as⁸⁷⁻⁹⁰

$$S_{\delta, \text{FDM}}(t) = S_0 \exp(-at - bt^{1/2}), \quad (72)$$

where S_0 is the peak signal, a is the Stern-Volmer quenching rate from Eq. (65) with $a = \gamma = 1/\tau$, and b is a measure of the heterogeneity of the quenching process. The exponent $1/2$ in Eq. (72) results for a three-dimensional environment. Exponents $1/3$ and $1/6$ apply to two dimensions and one dimension, respectively.⁹⁰ Sometimes the exponent itself is used as a fitting coefficient.⁹¹ Of particular interest to PSP research is work by Draxler et al.,^{88,89} who found that the oxygen quenching of Ru(dpp) in a series of

polymers (i.e., a PSP-like system) could be described better by the Förster Decay Model (FDM) from Eq. (72) than by the DEM from Eq. (70).

Taking the inverse Laplace transform of Eq. (72), it follows (see Ref. 92) that the associated Förster decay rate distribution is given by:

$$n_\gamma(\gamma) = \frac{4S_0}{\sqrt{\pi}b^2} G\left(\frac{b}{2\sqrt{\gamma-a}}\right), \quad (73)$$

where $G(x) \equiv x^3 \exp(-x^2)$, and $n_\gamma(\gamma) = 0$ for $\gamma \leq a$. Figure 47 illustrates this distribution, which peaks at $\gamma = a + b^2/6$ and has an approximate height $0.925S_0/b^2$ and an approximate full width at half maximum given by $0.45b^2$. The area under this distribution, defined by Eq. (69), is precisely equal to the amplitude S_0 , i.e., $A_{\text{FDM}} = S_0$.

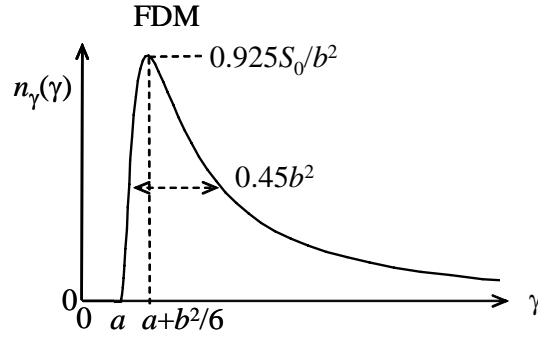


Figure 47. Illustration of FDM

7.3.4 Maximum Entropy Model

A model that is formally equivalent to the DEM is one in which the decay rate distribution, $n_\gamma(\gamma)$, is represented by a histogram of preselected decay rates, γ_μ , with bin widths $\Delta\gamma_\mu$ and to-be-determined bin areas a_μ (see Fig. 48).

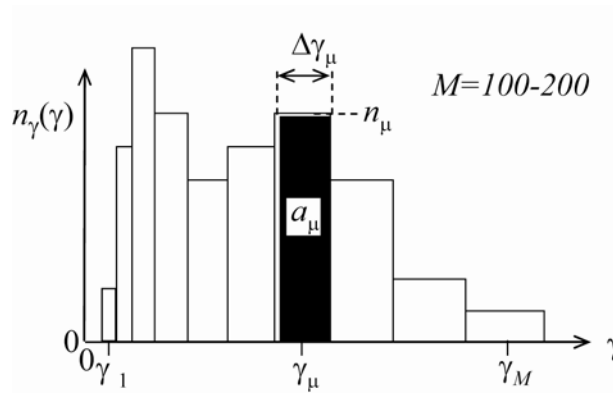


Figure 48. Illustration of MEM Decay Rate Distribution

The delta-function response of such a system can be written as [cf. Eq. (70)]:

$$S_{\delta, \text{MEM}}(t) = \sum_{\mu=1}^M a_\mu \exp(-\gamma_\mu t), \quad (74)$$

where M is the number of bins in the histogram. Typical values of M are in the range from 100 to 200. Fitting Eq. (74) to a measured fluorescence response is a linear problem (because the γ_μ values are preselected), but one that is highly ill conditioned.^{84,92-94} To obtain bin areas, a_μ , that are physically realistic (not negative and not strongly oscillatory), it is necessary to impose a constraint. In the Maximum Entropy Model (MEM), this constraint is taken to be the Shannon-Jaynes entropy⁹²⁻¹⁰⁰

$$E \equiv -\sum_{\mu=1}^M (a_\mu / A) \ln(a_\mu / A), \quad (75)$$

where A is the actual or estimated area under the distribution, given by [cf. Eq. (71) for the DEM]:

$$A_{\text{MEM}} = \sum_{\mu=1}^M a_\mu. \quad (76)$$

The discretized values of the distribution function $n_\gamma(\gamma)$ are given, in terms of the bin areas a_μ and the bin widths $\Delta\gamma_\mu$, by $n_\gamma(\gamma_\mu) = a_\mu/\Delta\gamma_\mu$.

7.3.5 Excitation Response Function

In physical chemistry, lifetime studies of quenched fluorophore systems typically are performed using short-pulsed lasers so that the assumption of delta-function excitation is satisfied. However, in PSP studies this may not be the case (for example, when pulsed LEDs are used as the excitation source). Moreover, to minimize PSP measurement time, the optimum pulse repetition frequency may be such that small amounts of residual fluorescence (from prior pulses) are tolerated. Both of these complications can be accounted for by convolving the presumed delta-function response of the paint [from Eq. (67), (70), (72), or (74)] by the normalized excitation pulse shape, $p(t)$, to arrive at the measured signal, $S(t)$, according to

$$S(t) = \int_{-\infty}^t p(t_0) S_\delta(t - t_0) dt_0. \quad (77)$$

The lower limit of the integral is set to $-\infty$ to indicate that the measured fluorescence response at time t extends over the entire excitation history of the system, including residual fluorescence from prior pulses.

By combining Eqs. (67) and (77), one can write the signal $S(t)$ as

$$S(t) = \int_0^\infty n_\gamma(\gamma) s_\gamma(t; \gamma) d\gamma, \quad (78)$$

where $s_\gamma(t; \gamma)$ is the Excitation Response Function (ERF) for monoexponential decay at a rate γ , given by

$$s_\gamma(t; \gamma) \equiv \int_{-\infty}^t p(t_0) e^{-\gamma(t-t_0)} dt_0. \quad (79)$$

The ERF may be calculated analytically (see Section 7.8) for simple pulse shapes, pulse trains, and waveforms, including the case of continuous excitation, with $p(t) = 1$ and $s_\gamma(t; \gamma) = 1/\gamma$.⁸⁰ Alternatively, the ERF must be calculated by numerical convolution if the pulse shape $p(t)$ is measured experimentally and cannot be described adequately by a simple analytical expression.⁹¹

7.3.6 Reconstruction of Decay Rate Distribution from Fluorescence Response

From the foregoing it follows that fitting a measured fluorescence response can be interpreted as reconstructing the underlying distribution of fluorescence decay rates. To do so, assume that the fluorescence response $S(t)$ has been sampled to yield a set of N values for S_i and that the pulse shape $p(t)$

has been measured, with the result that the ERF from Eq. (79) can be calculated for any desired value of γ . Fitting the above lifetime models to the fluorescence response data can then be cast as a least-squares fitting problem, in which the quantity

$$\chi^2 \equiv \sum_{i=1}^N \left\{ [S_i - S_i^{(\text{fit})}] / \sigma_i \right\}^2 \quad (80)$$

is to be minimized. Here $S_i^{(\text{fit})}$ represents the fitted signal value at point i , and σ_i is the estimated uncertainty for this point, proportional to the square root of S_i if photon shot noise is assumed.

In the case of the DEM and FDM, standard nonlinear regression can be used to determine optimum values of the fit parameters.¹⁰¹ In the DEM from Eq. (70), these are the K amplitudes, a_k , and associated decay rates, γ_k ; in the FDM, these are the parameters S_0 , a , and b from Eq. (72). In the case of the MEM, the to-be-minimized quantity is $\chi^2 + \lambda E$, where χ^2 is given by Eq. (80), E is given by Eq. (75), and λ is a to-be-determined Lagrange multiplier. Because the number of to-be-determined bin areas, a_k , in Eq. (74) typically is in the range from 100 to 200, a special algorithm is required.⁹²⁻¹⁰⁰ [The original Maximum Entropy Method (MEM) algorithm was developed for image reconstruction in astrophysics¹⁰² and has since been adapted for lifetime analysis.⁹³]

Years of research in physical chemistry (beginning with a seminal paper by James and Ware¹⁰³) have made it clear that it can be difficult to select, on the basis of the magnitude of fitted residuals alone, the best model for a particular system. For example, even if the true dynamics are given by a Förster model, a two-component DEM can give a good fit to the data.⁸⁰⁻⁸⁸ For this reason, it is desirable to consider not only the magnitude of the residuals, but also the behavior of the fitted parameters as a function of quencher density. This is illustrated in Section 7.4.

7.4 LIFETIME ANALYSIS OF PtTFPP IN FIB

In this section, the theory from Section 7.3 is applied to fluorescence decay measurements on the pressure-sensitive paint PtTFPP in FIB, which was developed at the University of Washington⁹ and is marketed by Innovative Scientific Solutions, Inc.

7.4.1 Experiment

Painted aluminum coupons were mounted in a calibration chamber in which air pressure and sample temperature were precisely controlled. Shop air with a specified dewpoint of -50°F was used to avoid complications caused by humidity effects. Samples were illuminated at a 45-deg angle by a commercial array of blue LEDs with peak emission at 465 nm, resulting in excitation of the PtTFPP Soret band. The illumination level was held constant to better than one percent over the course of the measurements. Fluorescence from the triplet state, filtered at 650 nm using a 40-nm FWHM custom bandpass filter with 70-percent transmission, was measured by a fast photomultiplier tube (PMT). The observation direction was also at a 45-deg angle to the sample normals, opposite from the incident light direction.

The LED source was pulsed at 4.95 kHz, giving a train of nearly square light pulses spaced at 202 μs , each with a duration of approximately 10 μs . Output from the PMT was sampled at 0.1- μs intervals from $-0.5 \mu\text{s}$ to about +100 μs relative to the trigger input, resulting in 1002 samples per curve. Curves were summed over 100 pulses using a digital oscilloscope. Preprocessing of the data was performed to subtract a baseline value and to determine the precise start of the optical pulse. Calibrations were carried out over a matrix of 25 pressures (from 20 to 2100 psf), each at 10 temperatures in the range from 40 to 120°F.

Figure 49 shows the measured optical pulse shape, $p(t)$, which has a rise time of about 0.5 μs and is followed by a small-amplitude tail (0.6 percent of peak signal) that extends about 13 μs beyond the main cutoff.

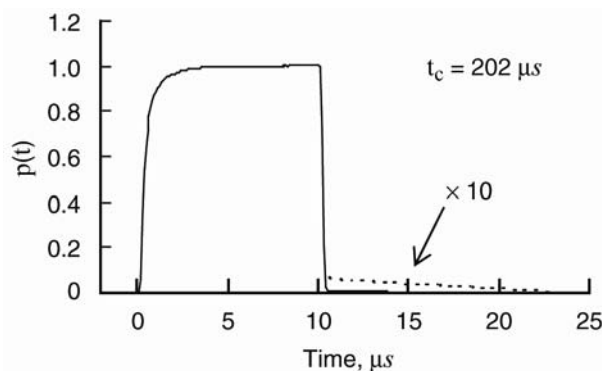


Figure 49. Normalized Illumination Pulse Shape

Figure 50 shows the measured fluorescence signal, $S(t)$, for several pressures at room temperature. Data are plotted on both a linear and a log scale. From the decay part of the fluorescence in Fig. 50b, it is evident that the fluorescence response is not single-exponential. Close examination of the data at the lowest pressures (i.e., the data with the longest lifetimes) also reveals the effect of residual fluorescence from pulses prior to the trigger pulse, with a maximum relative contribution of four percent of the peak signal (see Fig. 3 in Ref. 81).

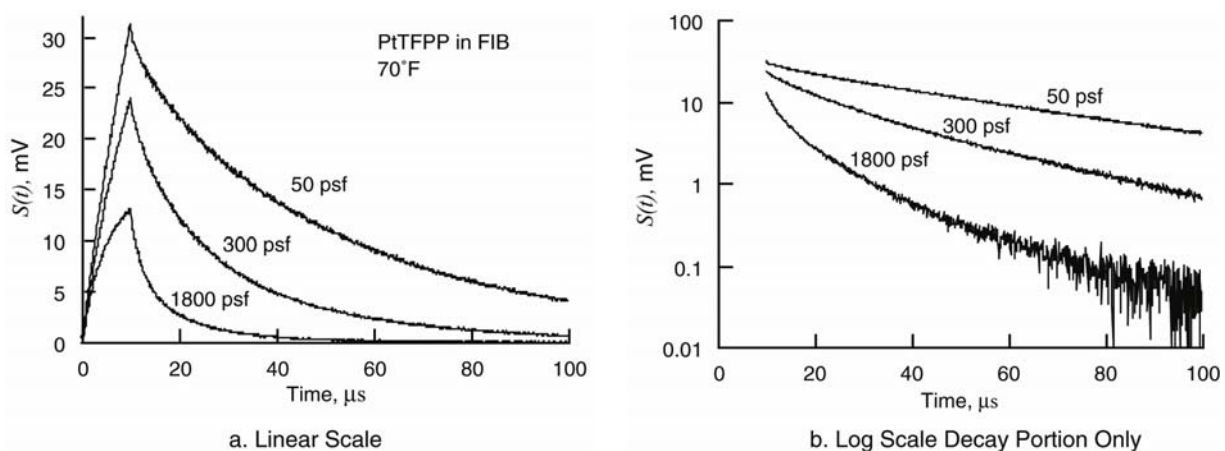


Figure 50. Selected Fluorescence Response Curves for PtTFPP in FIB

7.4.2 Data Analysis

All analysis was based on least-squares fitting of the measured fluorescence response curves, including the excitation phase (See Fig. 51). Numerical convolution was used to take into account the measured pulse shape and pulse repetition rate.⁸¹ Shot noise was assumed, with relative weights σ_i proportional to the square root of the signals S_i . A Levenberg-Marquardt algorithm (with explicit calculation of derivatives with respect to the fit parameters) was used for the DEM and FDM models. The MEM algorithm was adapted from Ref. 100, with some insights gleaned from Refs. 93 and 98. Convergence times for all three models were typically on the order of several seconds per data set on a 750-MHz Pentium-based processor. A simple peak-finding algorithm was used to identify peaks in the MEM distributions and to calculate the partial area fractions under the peaks relative to the total area under the distribution.

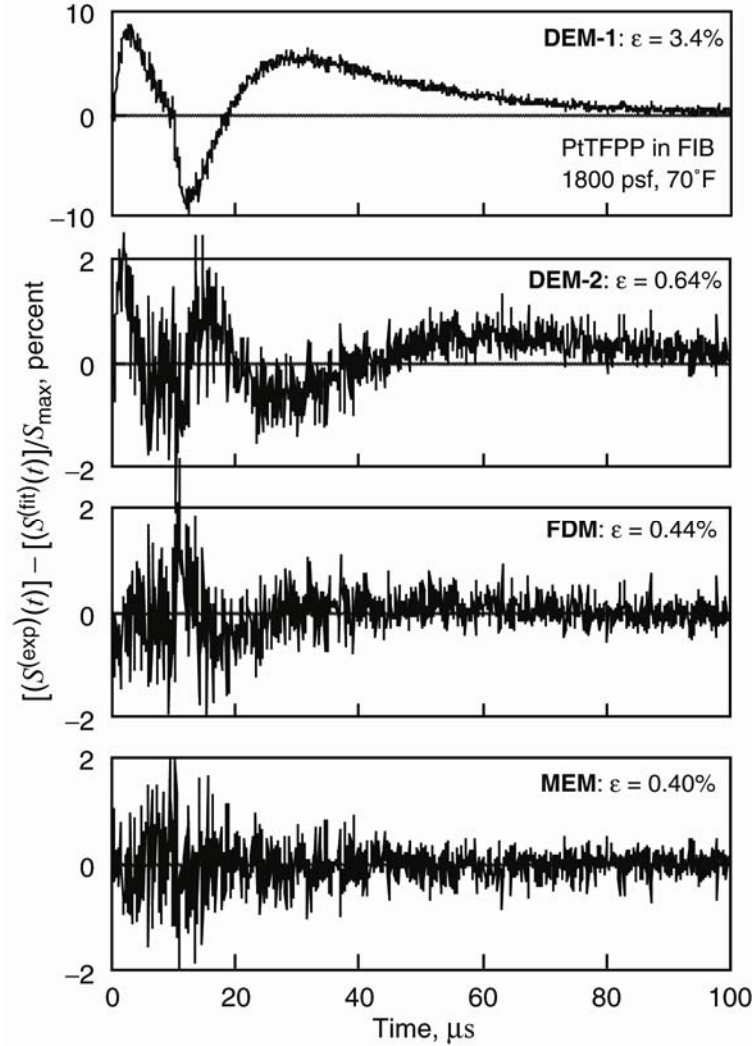


Figure 51. Fit Residuals for Data from Fig. 50 for Four Models

Of the three models tested, MEM consistently produced the best fit to the data. This is to be expected, because of the large number of adjustable parameters. Sample fit residuals, as a percentage of the peak signal (i.e., the signal at the end of the excitation pulse), are shown in Fig. 51. Insets also state the average RMS fit error, ϵ , as a percentage of the peak signal. Clearly, monoexponential decay (“DEM-1”) fails to fit the data. Differences between the two-component DEM (“DEM-2”), FDM, and MEM residuals are more subtle, with the MEM residuals showing the least structure.

Figure 52 shows the relative RMS error, ϵ , versus pressure. As stated, MEM consistently produces the smallest fit errors. Interestingly, for most pressures the three-parameter FDM fits produce lower residuals than the four-parameter DEM fits.

Representative decay rate distributions for the three models are shown in Fig. 53. The vertical axis of Fig. 53 has two sets of units: one for the DEM amplitudes and one for the FDM and MEM distributions. In the FDM case, the spectrum was obtained from Eq. (73) after the data were fitted using Eq. (72). While the FDM spectrum has only one peak, the MEM and (of course) two-component DEM spectra have two. For some data points, a small third peak was found in the MEM spectrum at small values of γ .⁸¹ More accurate measurements will be required to confirm that this third peak is not an artifact of the measurement and analysis schemes. Likewise, a three-component DEM fit produced only a marginal

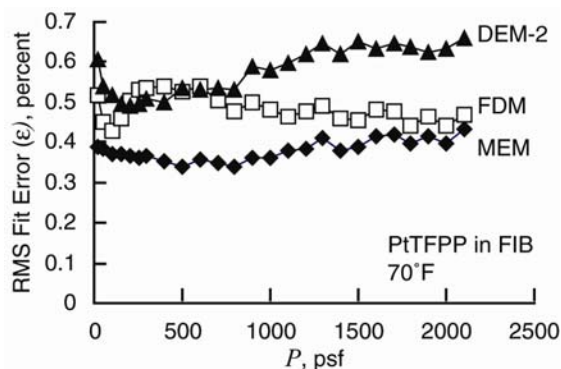


Figure 52. Rms Fit Residuals as a Function of Pressure

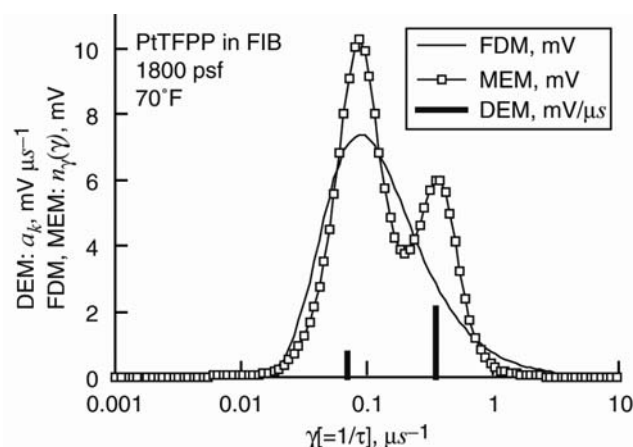


Figure 53. Implied Decay Rate Distributions for Data from Fig. 50

improvement over the two-component DEM, with no consistent placement of the third peak as a function of pressure. The two-peaked nature of the MEM spectrum, however, was consistent across all data points, even in cases in which the two peaks were not fully resolved.⁸¹

Figure 54 shows the areas, A , under the $n_\gamma(\gamma)$ distributions as a function of pressure for the three models. As argued following Eq. (69), these areas should, ideally, be independent of pressure, a reflection of the fact that the number of fluorophore molecules that participate in the excitation process is constant, regardless of quenching. Mild variations with pressure are found for each of the three models.

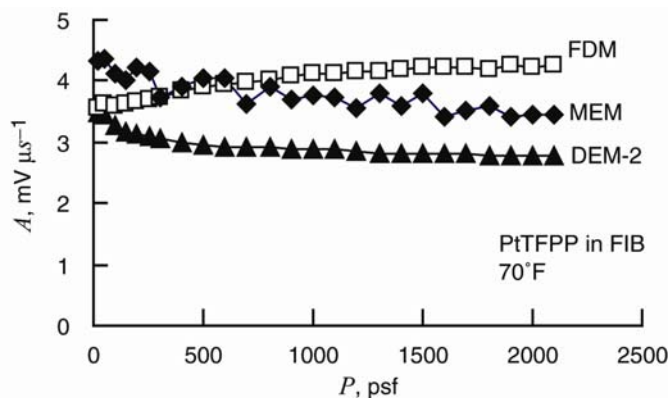


Figure 54. Areas Under Distribution Function as a Function of Pressure

Figure 55 shows the FDM parameters a and b from Eq. (72) as functions of pressure. Note the tendency of a towards negative values at large pressures. Figure 56 gives both the MEM and DEM peak positions as functions of pressure. The two sets of peak positions are in reasonable agreement, both suggesting a linear SV dependence as expressed by Eq. (65).

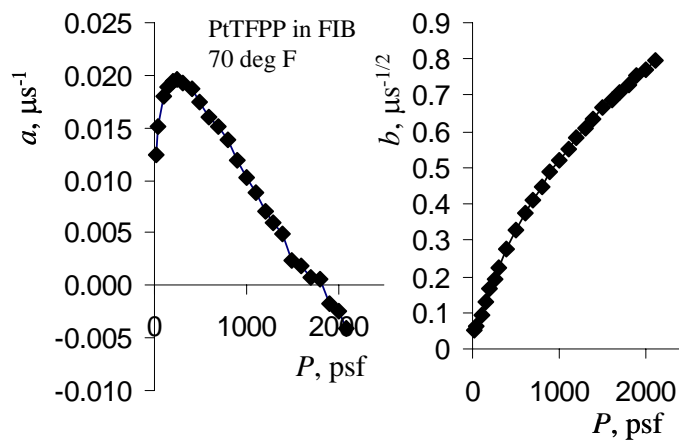


Figure 55. Förster Parameters a and b as a Function of Pressure

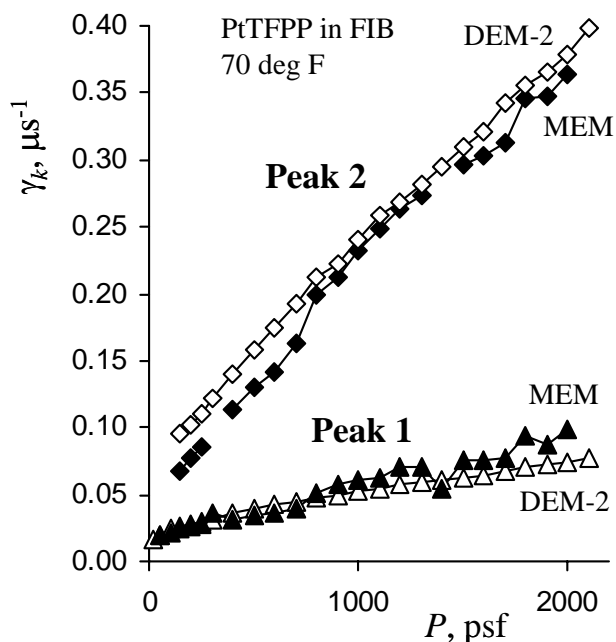
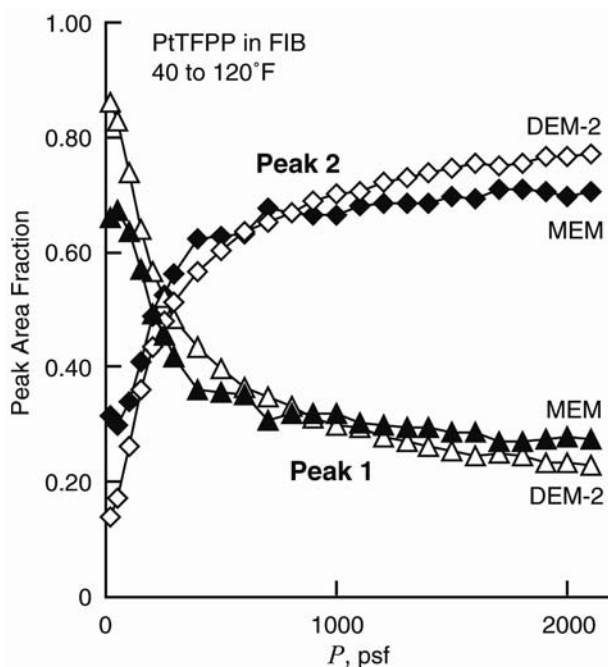


Figure 56. Stern-Volmer Diagram with Peak Positions vs. Pressure

Fitted values for the SV intercepts and slopes [expressed in the form of the vacuum lifetimes, τ_0 , and bimolecular quenching constant, κ_{SV} , from Eq. (65)] are listed in Table 9, which also lists the estimated uncertainties and fitted temperature sensitivities of these parameters. Finally, Fig. 57 gives the fractional contributions of the two peaks in the DEM and MEM distributions to the total area under the distribution. As is the case in Fig. 57, there is good agreement between the DEM and MEM results.

Table 9. Fitted Stern-Volmer Parameters for PtTFPP in FIB at 70°F

	Value	Slope (%/°F)
$\tau_0^{(1)}, \mu\text{s}$	51 ± 4	Unclear
$\tau_0^{(2)}, \mu\text{s}$	21 ± 5	Unclear
$\kappa_{SV}^{(1)}, \mu\text{s}^{-1}\text{Kpsf}^{-1}$	0.035 ± 0.004	$+ 0.11 \pm 0.04$
$\kappa_{SV}^{(2)}, \mu\text{s}^{-1}\text{Kpsf}^{-1}$	0.168 ± 0.015	$+ 0.22 \pm 0.02$

**Figure 57. Peak Area Fractions Associated with Fig. 56**

7.4.3 Interpretation of Results

Despite the fact that the FDM tends to produce better fits to the data than does the DEM, it does not appear that the FDM is a physically plausible model for the fluorescence decay of PtTFPP in FIB. In particular, the dependence of the SV parameter a in Fig. 55 is opposite the *rise* with pressure that is expected, and was found by Draxler et al., for the oxygen-quenching of Ru(dpp) in a series of polymers.⁸⁸ Also, unlike what was found by Draxler et al., the parameter b in Fig. 55 is strongly dependent on quencher density in the present case.

On the other hand, results of MEM analysis appear to confirm that a two-component DEM captures the essence of the fluorescence decay process correctly, even though the DEM does not account for nonzero widths of the peaks in the decay rate distribution. The fact that the MEM produces lower fit residuals than does the DEM indicates that the widths of the MEM peaks have a physical basis, even though it is known from previous work on MEM that noise on the data leads to broadening of the peaks in the MEM reconstruction.⁹⁶⁻⁹⁸

What remains to be explained is why the fractional areas of the two peaks are a strong function of quencher density. This behavior has previously been considered nonphysical from the perspective of a

microheterogeneous system, in which each peak is associated with a particular group of fluorophore molecules.⁸⁵⁻⁸⁸ An alternative explanation is suggested in Ref. 104 (also Section 8.0 of the present report), which involves a heretofore unknown intermediate state that appears to play a role in the fluorescence decay process. More work will be required to verify the existence of this intermediate state (involving, perhaps, detailed spatial¹⁰⁵ or spectral measurements¹⁰⁶) and to see if such an intermediate state plays a similar role in other PSP systems.

7.5 DISCUSSION

Three lifetime analysis models from the physical chemistry literature have been reviewed and applied to the fluorescence decay of PtTFPP in FIB, which is the current industry standard for large-scale PSP testing in the U.S. Included in this analysis are two effects that typically are avoided in physical chemistry: the finite width of the excitation pulse, and residual fluorescence from prior pulses. Of the three models studied, the Maximum Entropy Model produces the best fit to the data and suggests strongly that there are two components in the fluorescence decay. The associated decay rates and relative contribution fractions of these two components are also reproduced by a Discrete Exponential Model, even though the DEM fit residuals are larger than those of the MEM. A Förster Decay Model does not appear to be a plausible physical model for PtTFPP in FIB, even though it produces lower fit residuals than does the two-component DEM, and even though it has been advocated as an appropriate model for a similar system.⁸⁸

It is anticipated that insights from this work will guide the further development of lifetime-based PSP techniques. In particular, by providing tools for the measurement and modeling of the fluorescence decay dynamics of PSP systems, it should become possible to approach the optimization of lifetime-based PSP measurements in a fundamental way. This should be of particular interest to current efforts in which the concept of a two-gate measurement for pressure only is extended to one that encompasses three or four gates, while exploiting the nonsingle-exponential fluorescence dynamics of the paint to measure both pressure and temperature.

7.6 APPENDIX 7A: DERIVATION OF PROPORTIONALITY CONSTANT^{††}

The constant C in Eq. (68) may be derived as follows. Consider the case in which the environment of the fluorophore molecules is homogeneous, in the sense that each excited fluorophore molecule has the same probability of deexcitation, whether it be through emission of a fluorescence photon, nonradiative decay, or quenching. The number of excited-state fluorophore molecules in the observation volume, $N^*(t)$, may then be expressed by the rate equation

$$dN^*(t)/dt = R(t) - \gamma N^*(t), \quad (81)$$

where $R(t)$ is the production rate of excited-state fluorophores and γ is the average decay rate of the excited state. The solution of Eq. (81), for the initial condition $N^*(-\infty) = 0$, may be written as

$$N^*(t) = \int_{-\infty}^t R(t_0) e^{-\gamma(t-t_0)} dt_0. \quad (82)$$

If the excitation process is linear (see Section 7.7), the production rate, $R(t)$, may be written in terms of the normalized pulse shape, $p(t)$, as

$$R(t) = A_s d_s n_f \frac{\Phi_{\max}}{h\nu_{\text{ex}}} p(t) \sigma_{\text{ex}} Q, \quad (83)$$

^{††}Material in Sections 7.6, 7.7, and 7.8 is taken from Ref. 23: W. Ruyten, "Assimilation of Physical Chemistry Models for Lifetime Analysis of Pressure-Sensitive Paint," AIAA Paper 2004-0880, 42nd AIAA Aerospace Sciences Meeting and Exhibit, Reno, NV, January 5-8, 2004.

where A_s is the area of the sample viewed by the detector, d_s is the effective thickness of the sample (see Section 7.7), n_f is the ground-state fluorophore density, $\Phi_{\max}/h\nu_{\text{ex}}$ is the incident photon flux at the surface (in terms of the power density Φ_{\max} , Planck's constant h , and the average frequency, ν_{ex} , of the excitation light), σ_{ex} is the effective excitation cross section, and Q is the quantum efficiency for conversion of the initially excited singlet state to the fluorescing triplet state. The ordering of the factors on the right-hand side of Eq. (83) follows the sequence of steps that a fluorophore molecule experiences during its promotion from the ground state to the fluorescing state, starting with $A_s d_s n_f$, the number of available ground-state molecules in the observation volume.

Given the number of excited fluorophores, $N^*(t)$, the fluorescence signal, $S(t)$, may be written as

$$S(t) = N^*(t) \Gamma_{\text{em}} \eta_{\text{em}} \Delta t N_p, \quad (84)$$

where Γ_{em} is the rate of fluorescence (with $\Gamma_{\text{em}} \leq 1/\tau$, because the total deexcitation rate involves nonradiative decay and quenching as well), η_{em} is the overall efficiency with which fluorescence photons are converted to units of signal (e.g., mV), Δt is the sampling interval for the signal $S(t)$, and N_p is the number of pulses over which the signal is integrated.

Combining Eqs. (82) through (84) and integrating over the decay rate distribution $n_\gamma(\gamma)$ from Eq. (67) then yields Eq. (68), with a constant C given by

$$C \equiv A_s d_s \frac{\Phi_{\max}}{h\nu_{\text{ex}}} \sigma_{\text{ex}} Q \Gamma_{\text{em}} \eta_{\text{em}} \Delta t N_p. \quad (85)$$

7.7 APPENDIX 7B: CONDITIONS FOR LINEAR EXCITATION AND FLUORESCENCE

The following assumptions are implicit in the derivation of the excitation and fluorescence decay processes from Section 7.6.

Assumption 1: The excitation process is linear with respect to the intensity of the incident light (i.e., it is not a multiphoton process).

Assumption 2: The decay rate, γ , is independent of time. In the context of PSP measurements, this is to say that the measurement takes place under steady-state conditions, or that the pressure distribution varies on a time scale that is much longer than the associated lifetime $\tau = 1/\gamma$.

Assumption 3: An effective sample thickness, d_s , can be assigned, even though the paint may be (and typically is) optically thick. For an optically thick paint, this means that d_s is less than the actual thickness of the paint.

Assumption 4: The ground-state fluorophore density that is available for excitation, n_f , is independent of time. This assumption is satisfied if, and only if, the excitation process does not lead to a significant depletion of the ground-state population. In practice, this sets an upper limit on the strength of the excitation light, under which a linear input-output relation holds true.

Assumption 5: The quantum efficiency, Q , is independent of time. Specifically, it is assumed that conversion from the initially excited singlet state to the fluorescing triplet state is instantaneous compared to the lifetime τ .

Assumption 6: No processes, other than pumping ground-state atoms via the singlet state, contribute to the production of excited-state molecules. Specifically, this assumes that delayed fluorescence is negligible, by which triplet-state molecules undergo an internal conversion to an intermediate state and, after some delay, are converted back to the triplet state.

Assumption 7: The detection efficiency, η_{em} , is independent of time. Specifically, this assumes that a fast detector is used, whose time constant is fast compared to the lifetime τ .

Assumption 8: Effective values of v_{ex} , σ_{ex} , Q , Γ_{em} , and η_{em} may be assigned, even though both the excitation process and the emission process involve wavelength ranges that are set by the light source, the detector, and any optical filters used.

All these assumptions can be relaxed in favor of a more rigorous treatment. See, for example, Ref. 106 for a study on the ability of a PSP measurement to resolve a dynamic pressure change, or Ref. 107 for a study in which lifetime analysis of a PSP-like system is performed as a function of emission wavelength. Also, if the detector response is not instantaneous but given in terms of an instrument response function (IRF), this IRF can be convolved with the ERF to obtain a total response function for a single decay rate γ .

7.8 APPENDIX 7C: SPECIAL PULSE SHAPES

The excitation response function may be calculated analytically for simple pulse shapes. Table 10 lists the results for excitation by a single delta function (with effective duration Δt_p), a train of such delta functions spaced at a cycle time t_c , a single square pulse with duration t_p , a rounded square pulse with the same duration but with a rise-time τ_r , a sinusoid with frequency $\omega = 2\pi/t_c$ and modulation depth M_0 (or $2m_0$), and a continuous wave.

Table 10. Excitation Response Functions for Selected Pulse Shapes

Pulse Shape, $p(t)$	ERF, $s_\tau(t)$	Illustration
$\delta\left(\frac{t}{\Delta t_p}\right)$	$\begin{cases} 0, & t < 0 \\ \Delta t_p e^{-t/\tau}, & t \geq 0 \end{cases}$	Fig.58a
$\sum_{n=-\infty}^{\infty} \delta\left(\frac{t - nt_c}{\Delta t_p}\right)$	$\frac{\Delta t_p}{1 - e^{-t_c/\tau}} e^{-t/\tau}, \quad 0 \leq \text{mod}(t, t_c) < t_c$	Fig. 58b
$\begin{cases} 1, & 0 \leq t \leq t_p \\ 0, & \text{elsewhere} \end{cases}$	$\begin{cases} 0, & t < 0 \\ \tau - \tau e^{-t/\tau}, & 0 \leq t \leq t_p \\ s_\tau(t_p) e^{-(t-t_p)/\tau}, & t > t_p \end{cases}$	Fig. 58c
$\begin{cases} 1 - e^{-t/\tau_r}, & 0 \leq t \leq t_p \\ 0, & \text{elsewhere} \end{cases}$	$\begin{cases} 0, & t < 0 \\ \tau + \frac{\tau}{\tau - \tau_r} [\tau_r e^{-t/\tau_r} - \tau e^{-t/\tau}], & 0 \leq t \leq t_p, \quad \tau_r \neq \tau \\ \tau - (\tau + t) e^{-t/\tau}, & 0 \leq t \leq t_p, \quad \tau_r = \tau \\ s_\tau(t_p) e^{-(t-t_p)/\tau}, & t > t_p \end{cases}$	Fig. 58d
$1 - m_0 + m_0 \sin(\omega t)$ $\omega = 2\pi/t_c, \quad m_0 = \frac{M_0}{2}$	$(1 - m_0)\tau + \frac{m_0\tau}{\sqrt{1 + \omega^2\tau^2}} \sin(\omega t - \phi_\omega)$ $\phi_\omega = \tan^{-1}(\omega\tau)$	Fig. 58e
1	τ	Fig.58f

Figure 58 gives a graphical illustration of the pulse shapes $p(t)$ and resulting ERFs $s_\tau(t)$ from Table 10 (i.e., the ERFs are expressed in terms of the lifetime τ rather than the decay rate γ), for both fast and slow decay. The relative vertical scaling between $p(t)$ and $s_\tau(t)$ in Fig. 58 (i.e., between quantities with different

units) varies by row, but not by column. Thus, for example, in Fig. 58c, a longer lifetime produces not only a slower rise and a slower decay, but also a higher peak signal. Note the effects of residual fluorescence in Fig. 58b for the long-lifetime case. Figure 58e depicts the scenario encountered in frequency-domain spectroscopy, in which measurement of the phase shift ϕ_ω as a function of the modulation frequency ω forms the basis for lifetime analysis.

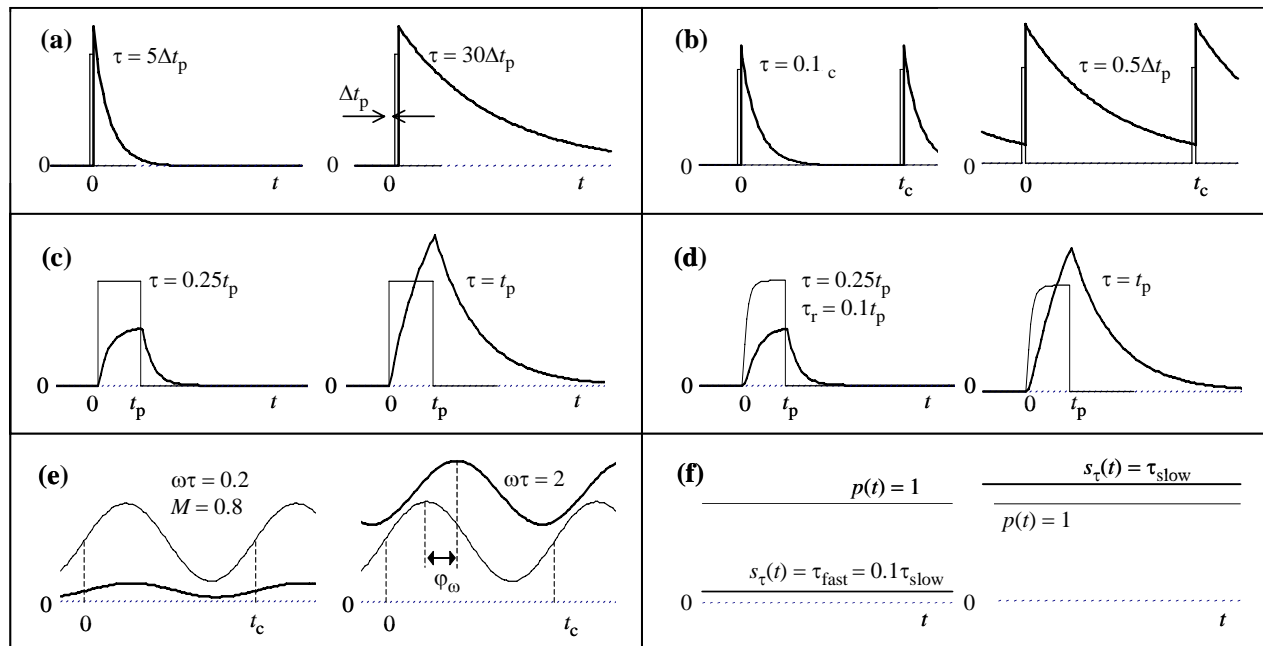


Figure 58. Pulse Shapes and ERFs from Table 10

7.9 ACKNOWLEDGMENTS

The measurements discussed herein were performed by Marvin Sellers. Prof. M.E. Lippitsch of the University of Graz was gracious in supplying supplementary data to Ref. 88. Discussions with Prof. Sullivan of Purdue University are gratefully acknowledged.

8.0 OXYGEN QUENCHING OF PTFPP IN FIB POLYMER: A SEQUENTIAL PROCESS?^{§§}

8.1 OVERVIEW

Oxygen quenching of PtTFPP in FIB polymer is analyzed using a discrete exponential model (DEM), a Förster decay model (FDM), and a maximum entropy model (MEM). The FDM, which has been advocated for a similar system to counter presumed nonphysical dependence of the DEM amplitudes on quencher density, is discounted for the present system. Instead, the MEM is found to support the DEM in suggesting that the decay-rate distribution is bimodal, with fractional contributions that depend on quencher density. A sequential decay mechanism involving a to-be-identified intermediate state is proposed to explain this behavior.

8.2 INTRODUCTION

The study of the fluorescence lifetime behavior of molecules sequestered in a host matrix continues to be the subject of active research.^{9,71,85,88,89,105-111} Since about 1985, it has been clear that it can be difficult to ascertain, by analysis of the fluorescence decay alone, whether the underlying lifetime spectrum is continuous or discrete in nature.¹⁰³ Additional insight into the dynamics may be obtained by studying the quenching behavior of such systems.^{9,71,85,88,89,105-110} In particular, the fractional contributions of discrete components in the spectrum should be independent of quencher density if these contributions are to reflect a fixed partitioning of the fluorophore molecules with regard to quenching.^{85,88,89} In 1995, such considerations led Draxler et al. to advocate a Förster decay model (FDM) over a discrete exponential model (DEM) for oxygen quenching of Ru(dpp) in a number of polymers.^{88,89} Here, the opposite finding is reported for oxygen quenching of PtTFPP in FIB polymer [Pt(II) meso-tetra (Pentafluorophenyl) porphine in fluoro-isopropyl-butyl], a sprayable paint that has become popular for measuring air-pressure distributions on test articles in wind tunnels by optical means.^{1,9,81,109} An alternative explanation, involving sequential decay, is proposed for the observed lifetime behavior of this system. Results of the analysis are supported by a maximum entropy model (MEM).^{92,93,96,98,100}

8.3 EXPERIMENT

The paint PtTFPP in FIB was developed at the University of Washington.^{9,109} and is available from Innovative Scientific Solutions, Inc. Painted aluminum coupons were mounted in a calibration chamber in which air pressure, low humidity, and sample temperature were precisely controlled. Samples were illuminated by an array of blue LEDs with peak emission at 465 nm, resulting in excitation of the PtTFPP first excited singlet state. The illumination level was held constant to better than 1 percent. Fluorescence from the triplet state, filtered at 650 nm using a 40-nm FWHM bandpass filter, was measured by a fast photomultiplier tube (PMT). The LED source was pulsed at 4.95 kHz. Nominal pulse width was 10 μ s, with a rise time of approximately 0.5 μ s. Output from the PMT was sampled at 0.1- μ s intervals, from -0.5 μ s to about +100 μ s relative to the trigger input, and this process resulted in 1002 samples per curve. Curves were summed over 100 pulses using a digital oscilloscope. Preprocessing of the data was performed to subtract a baseline value and to determine the precise start of the optical pulse; the result was fluorescence response curves, $S(t)$, such as those shown in Fig. 50. Measurements were carried out over a range of air pressures (from 1 to 100 kPa) and temperatures (from 4 to 49°C).

^{§§}Previously published as "Oxygen Quenching of PtTFPP in FIB Polymer: a Sequential Process?" in *Chemical Physics Letters*, Vol. 394, No. 1-3, 2004, pp. 101-104.

8.4 ANALYSIS

The measured fluorescence response curves, $S(t)$, were fit to delta-function response curves, $S_\delta(t)$, convolved with the measured pulse shape; also taken into account were small amounts of residual fluorescence (< 4 percent) from prior pulses.⁸¹ For the DEM, FDM, and MEM, $S_\delta(t)$ is presumed to be given, respectively, by the following relations^{9,90,92,109} (see also Section 7.3):

$$S_{\delta, \text{DEM}}(t) = \sum_{k=1}^2 a_k \exp(-\gamma_k t), \quad (86)$$

$$S_{\delta, \text{FDM}}(t) = S_0 \exp(-at - bt^{1/2}), \quad (87)$$

and

$$S_{\delta, \text{MEM}}(t) = \sum_{\mu=1}^{100} a_\mu \exp(-\gamma_\mu t). \quad (88)$$

The DEM and FDM have four and three fit parameters, respectively, while the MEM has 100. (The MEM decay rates, γ_μ , were fixed in equal increments, $\Delta\gamma_\mu$, along a log axis that stretches from $\gamma = 0.001 \mu\text{s}^{-1}$ to $\gamma = 10 \mu\text{s}^{-1}$.) Smoothness of the MEM distribution was enforced by a Shannon-Jaynes entropy constraint, following Refs. 93, 98, and 100. All analysis was based on least-squares fitting of the measured fluorescence response curves, including the excitation phase. Further details of the experimental and numerical techniques employed may be found in Ref. 81.

8.5 RESULTS

Figure 51 shows selected fit residuals for the three models. The three-parameter FDM consistently produced fits that were equally good or somewhat better than the four-parameter DEM fits, while the MEM produced the best fits overall. Relative RMS fit errors, ε (expressed as a percentage of the peak signal), were in the range from 0.35 to 0.65 percent for all data.

Figure 53 shows the implied decay-rate distributions for the data from Fig. 51. For the FDM, this distribution is obtained by taking the inverse Laplace transform of Eq. (87), yielding⁹²

$$n_\gamma(\gamma) = \frac{4S_0}{\sqrt{\pi}b^2} G\left(\frac{b}{2\sqrt{\gamma-a}}\right), \quad (89)$$

where $G(x) \equiv x^3 \exp(-x^2)$ and $n_\gamma(\gamma) = 0$ for $\gamma \leq a$. For the MEM, the distribution in Fig. 53 is given by the factors a_μ in Eq. (88), divided by the widths, $\Delta\gamma_\mu$, of the γ_μ bins.⁹² While the modality of the DEM and the FDM is inherent in the definition of the presumed delta-function response (bimodal and unimodal, respectively), the modality of the MEM is not determined *a priori*. For this reason, the bimodal nature of the MEM distribution may be taken as a strong indication that the fluorescence decay is governed by two time constants, or at least by two distinct distributions. (As established previously, the widths of peaks in a MEM spectrum are attributable, in part, to noise on the data.⁹³) Further indication that the FDM is not the correct model for the present system lies in the fact that the fit parameter a from Eq. (87) is found to *decrease* with pressure (a roughly linear *increase* would be expected⁷⁰), while the fitted value b from Eq. (87) is found to be strongly dependent on pressure, instead of being approximately constant.⁸¹

On the other hand, while the results of the DEM produce the largest fit residuals, they are remarkably consistent with results from the MEM, both with regard to the positions of the two peaks in the distribution (see Fig. 56) and with regard to the fractional contributions of the two peaks to the total signal (see Fig. 57). (For the MEM, the peak positions are those of the maxima in the distributions, while the fractional contributions were determined by dividing the MEM distributions at the minima between the

peaks; the data in Fig. 57 were also averaged over the range from 4 to 49°C, because the fractional contributions were found to be insensitive to temperature.)

Two features stand out in Figs. 56 and 57: the remarkable linearity of the Stern-Volmer (SV) behavior in Fig. 56 and the strong dependence of the fluorescence fractions on pressure in Fig. 57. This latter dependence is inconsistent with a fixed partitioning of the fluorophore molecules with respect to quenching and is precisely the type of behavior that led Draxler et al. to advocate the FDM over the DEM for their system.⁸⁸

8.6 PROPOSED MODEL

It is now argued that the behavior shown in Fig. 57 is consistent with a *sequential* decay model, in which two microsecond-type processes play a role. This concept is illustrated in Fig. 59, in which two excited fluorophore states, “1” and “2,” are populated at rates p_1 and p_2 via the short-lived singlet state, are depopulated at rates γ_1 and γ_2 , and have a one-way crossover rate, γ_{12} . Fluorescence dynamics of this kind are found in donor-acceptor systems, in which excited-state energy is transferred from one type of fluorophore to another,¹¹² yielding fluorescence lifetimes $\tau_1 \equiv 1/(\gamma_1 + \gamma_{12})$ and $\tau_2 \equiv 1/\gamma_2$. Assume now that the decay rate γ_1 is negligible (i.e., $\gamma_1 = 0$). In this case it is not necessary to specify the relative efficiencies with which fluorescence from states 1 and 2 is detected, and the fractional contribution of lifetime τ_1 to the fluorescence signal is given by an expression that is similar to that which follows from Eqs. (17) and (18) in Ref. 112, with p_1 and p_2 playing the roles of the initial donor and acceptor populations, γ_1 and γ_2 playing the roles of the donor and acceptor decay rates, and γ_{12} playing the role of the donor-acceptor transfer rate. Thus:

$$f_1 = \frac{p_1}{p_2} \left\{ \frac{\gamma_{12}}{\gamma_2 - \gamma_{12}} \right\}. \quad (90)$$

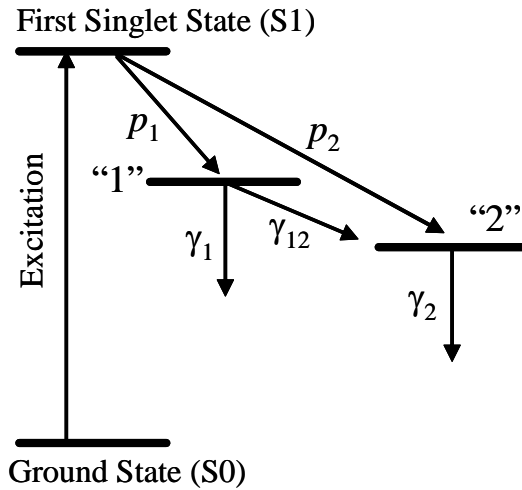


Figure 59. Schematic of Proposed Sequential Decay Process

Now assume that the rates γ_{12} and γ_2 are given by the solid lines in Fig. 60a, which are linear fits to the MEM results in Fig. 56. Also assume that $p_1 = p_2$. The fluorescence fraction, f_1 , from Eq. (90) and its complement, $f_2 = 1 - f_1$, are then given by the solid lines in Fig. 60b. The agreement between this predicted behavior and the measured fractions from Fig. 57 is remarkable and thus argues for the validity of the proposed model.

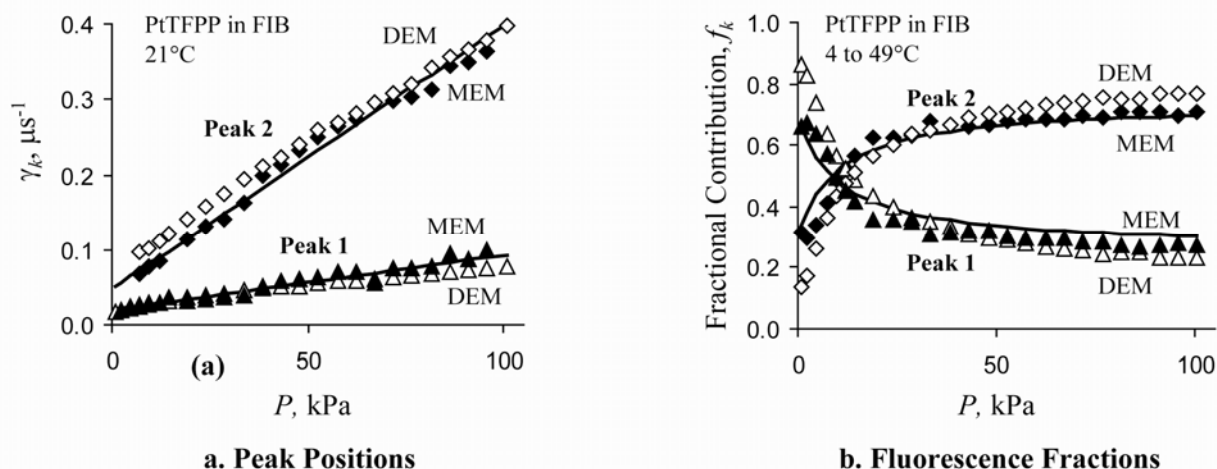


Figure 60. Peak Positions and Contribution Fractions for Sequential Decay Model

8.7 DISCUSSION

The assumptions $\gamma_1 = 0$ and $p_1 = p_2$ are perhaps overly simplistic. More generally, one might allow that $\gamma_1 \neq 0$, that γ_1 and γ_{12} have separate SV dependencies (only the sum dependence is measured in Fig. 4a), that $p_1 \neq p_2$, and that both states 1 and 2 contribute to the observed fluorescence signal, with relative efficiencies η_1 and η_2 . This expanded assumption introduces four additional parameters into the model: one unknown SV intercept, one unknown SV slope, the ratio p_1/p_2 , and the ratio η_1/η_2 . This allows for additional combinations of parameters that can produce the fluorescence fractions in Fig. 60b. Thus, the fact that the fractions in Fig. 60b can be reproduced without the additional four parameters may be a coincidence. Even so, the proposed model makes a strong case for the presence of a heretofore unknown intermediate state. To identify the nature of this state, more research is required, involving, perhaps, spectrally resolved measurements in addition to temporally resolved ones.¹⁰⁶ Among the possible implications of this work is the extension of luminescent paint techniques from measurement of pressure only to measurement of pressure and temperature in combination, as is discussed in detail in Section 9.0.

8.8 ACKNOWLEDGMENTS

The measurements discussed herein were performed by Marvin Sellers. Professor M.E. Lippitsch, one of the several authors of Ref. 88, was gracious in supplying supplementary data to that study.

9.0 OPTIMIZATION OF THREE-GATE LIFETIME PRESSURE- AND TEMPERATURE-SENSITIVE PAINT MEASUREMENTS^{***}

9.1 OVERVIEW

A theoretical model is described to optimize the performance of a lifetime-based pressure-sensitive paint system, in which signals are collected at three gates, with the goal of performing a temperature-compensated pressure measurement, or a measurement in which both pressure and temperature are obtained. While the three-gate approach eliminates the temperature bias of a conventional two-gate measurement, the shot-noise-induced error in a three-gate measurement is not necessarily better than the temperature bias in a two-gate measurement; in fact, it is potentially much worse. This effect is quantified by considering the relative temperature sensitivities of the paint at the selected gate ratios, both for results that have been reported to date in the literature and for new paints that might be developed by combining pressure-sensitive and temperature-sensitive probes in a single binder.

9.2 INTRODUCTION

Pressure-sensitive paint has established itself as an important technique for measuring pressure distribution on test articles in aerodynamic test facilities, especially transonic wind tunnels. The principle of the technique has been reviewed extensively elsewhere.^{1,2} In its most common form, a paint containing luminescent probe molecules is applied to a test article, which then is illuminated by short-wavelength light to produce a pressure-dependent emission signal at a longer wavelength. The pressure dependence typically comes about because of radiationless quenching of excited probe molecules by oxygen. Measurements can be performed using continuous or pulsed illumination. In the latter case, images of the test article are captured using digital cameras that are gated with respect to the train of illumination pulses. By suitable selection of the pulse repetition frequency, pulse duration, and start and end times of the camera gates, the ratio of the signals collected during two gates becomes a function of pressure, thereby forming the basis for a pressure measurement.

Among the complications of such PSP measurements is the fact that signal ratios usually depend on temperature to a mild degree.⁷⁵ Variations in surface temperature thus tend to produce pressure measurement errors. Recent work on lifetime-based PSP suggests that, given a suitable paint, measurement at a third gate might be added to compensate for this unwanted temperature dependence and to perform a temperature measurement in its own right. In Section 9.3 this previous work is reviewed and cast in a form that lends itself to a new theoretical approach. This new approach is developed in Section 9.4 to guide further work in this area. In Section 9.5 the model from Section 9.4 is applied to published data on current paints, with the goal of optimizing three-gate PSP measurements and defining critical parameters for a possible new paint. Section 9.6 concludes with a discussion.

9.3 REVIEW OF PREVIOUS WORK

Figure 61 shows an example of a fluorescence response, $S(t;P,T)$, that might be the result of excitation of the paint by a square pulse. The exact shape of the response (especially that of the decay portion) depends on the pressure, P , and temperature, T , of the surface.^{80,81} High pressures produce faster decays than do lower pressures. To a lesser extent, high temperatures also produce faster decays than do lower temperatures. Because PSP is primarily an image-based technique, it is not practical to measure the detailed shape of the response function, except in calibration measurements. Instead, lifetime-based PSP measurements rely on integrating the signal under limited portions of the response function. The single-pulse signal, s_i , for a gate with index i may thus be written as

^{***}Previously published as "Optimization of Three-Gate Lifetime Pressure- and Temperature-Sensitive Paint Measurements," AIAA Paper 2004-2190, 24th AIAA Aerodynamic Measurement Technology and Ground Testing Conference, Portland, OR, June 28-July 1, 2004.

$$s_i = \int_{t_{i2}}^{t_{i1}} S(t; P, T) dt , \quad (91)$$

where t_{i1} and t_{i2} denote the start and end times of gate i (see Fig. 61). If N_i is understood to represent the number of pulses over which the gate- i signal is integrated and N to represent the total number of pulses (i.e., $N = N_1 + N_2$ for a two-gate measurement and $N = N_1 + N_2 + N_3$ for a three-gate measurement), the pulse-integrated signal for gate i may then be written as

$$S_i = N f_i s_i , \quad (92)$$

where $f_i \equiv N_i/N$. That is, f_i represents the fraction of the total measurement that is devoted to collecting the signal at the i -th gate. (As shown by Bell, it should not be considered a foregone conclusion that the same number of pulses should be devoted to each gate.⁷)

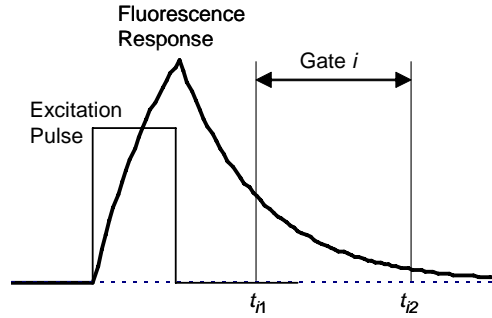


Figure 61. Schematic of Gated Measurement

Based on Eq. (92), the ratio between two signals, S_i and S_j , acquired at separate gates i and j , may be written as

$$R_{ij} \equiv \frac{S_i}{S_j} = \frac{f_i s_i}{f_j s_j} \equiv \frac{f_i}{f_j} r_{ij} , \quad (93)$$

where r_{ij} may be thought of as the intrinsic single-pulse ratio for the two gates. Figure 62 shows an idealized dependence of this ratio on pressure and temperature, with S_i measured during or immediately following the excitation pulse, and S_j measured after some delay.

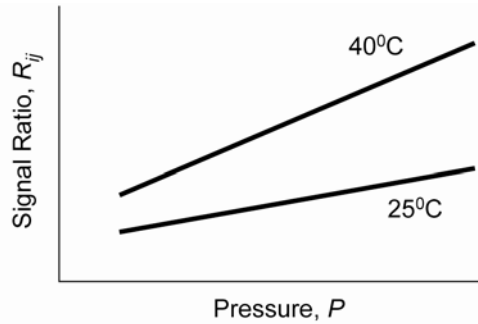


Figure 62. Dependence of Signal Ratio on Pressure and Temperature

If the paint response can be characterized by a single time constant, τ , the ratio R_{ij} may be written explicitly in terms of this time constant.^{7,78,79} Given these conditions, it is possible to define the relative sensitivity $(d\tau/\tau)/(dR_{ij}/R_{ij})$. Several authors have followed this approach to optimize the operational parameters of a two-gate PSP measurement.^{7,78,79} Here a more general approach is employed that allows for the presence of multiple time constants in the fluorescence response. In this generalized approach, the

intrinsic pulse ratio r_{ij} from Eq. (93) at a pressure $P_0 + \Delta P$ and a temperature $T_0 + \Delta T$ near an operating point (P_0, T_0) is written as

$$r_{ij} = r_{ij}^{(0)} [1 + p_{ij} \Delta P + t_{ij} \Delta T], \quad (94)$$

where $r_{ij}^{(0)}$ is the ratio at the operating point and p_{ij} and t_{ij} are the relative partial derivatives of this ratio with respect to pressure and temperature, also at the operating point.

Equation (94) is not meant to describe accurately the calibration equation for a PSP measurement over the entire range of pressures and temperatures of interest. This generally requires the inclusion of quadratic and cubic terms in addition to the linear terms from Eq. (94). Rather, the linear form of Eq. (94) is used in Sections 9.4 and 9.5 to approach the optimization of a two-gate or three-gate PSP measurement near an operating point (P_0, T_0) .

Table 11 lists values of $r_{ij}^{(0)}$, p_{ij} , and t_{ij} that were calculated from published data from authors who have reported early results on combined pressure and temperature measurements using a lifetime-based PSP system. These are Mitsuo et al.,¹² Watkins et al.,¹³ Davies et al.,¹¹³ and Hradil et al.¹⁰ Details on paints and gating parameters are noted in the table and are discussed further in Section 9.5. Of the authors listed in Table 11, only Hradil et al. deliberately introduced a second time constant into the paint, by adding a second probe molecule (a long-lived phosphor with a 3-ms time constant).

Table 11. Paint Parameters at 1 atm and 25°C

Authors	Paint	Gate 1	Gate 2/3	$r_{ij}^{(0)}$	p_{ij} , atm ⁻¹	t_{ij} , °C ⁻¹	η_{ij} , %/°C
Mitsuo et al.	PtTFPP in FEM	0 to 0.8 μ s	12 to 19 μ s	0.70	1.29	0.0370	-2.90
		0 to 0.8 μ s	30 to 83 μ s	0.70	1.55	0.0670	-4.30
Watkins et al.	PtTFPP in FEM	0 to 1 μ s	12 to 20 μ s	2.10	0.99	0.0110	-1.14
		0 to 1 μ s	30 to 83 μ s	3.00	1.23	0.0150	-1.20
Watkins et al.	PtTFPP in FIB	0 to 1 μ s	12 to 20 μ s	1.76	0.74	0.0033	-0.45
		0 to 1 μ s	30 to 83 μ s	2.34	0.99	0.0048	-0.49
Davies et al.	Porphyrin in Siloxane	0 to 0.5 τ	τ to 2 τ	1.69	0.70	0.0037	-0.53
Hradil et al.	Ru(dpp)/MFG in MTEOS	0 to 0.65 μ s	1.3 to 2.6 μ s	0.73	0.08	0.0022	-2.61
		0 to 0.65 μ s	3.5 to 7.1 ms	0.014	-0.05	0.0002	3.65

From Eq. (94) it follows that the temperature sensitivity of a PSP measurement can be expressed as

$$\frac{\Delta P}{\Delta T} = -\frac{t_{ij}}{p_{ij}}. \quad (95)$$

This sensitivity is typically quoted as percent pressure per unit temperature at some operating pressure P_0 and is expressed here as

$$\eta_{ij} \equiv \frac{1}{P_0} \frac{\Delta P}{\Delta T} \times 100\% = -\frac{1}{P_0} \frac{t_{ij}}{p_{ij}} \times 100\%. \quad (96)$$

Values of this relative temperature sensitivity, η_{ij} , are included in Table 11 and are typically on the order of one percent per degree Celsius at one atmosphere. Such values are also typical for intensity-based PSP measurements, in which signal ratios are calculated between reference (“wind-off”) and run (“wind-on”) conditions under constant illumination.¹

9.4 THREE-GATE VS. TWO-GATE MEASUREMENTS

The goal in this section is to take a conceptual look at how a temperature error produces a pressure error in a two-gate PSP measurement and how this error might be reduced by a three-gate measurement. Let ΔS_i and ΔS_j denote errors in the signals S_i and S_j attributable to noise or systematic effects and let ΔP

and ΔT denote the corresponding errors in pressure and temperature. From Eqs. (93) and (94), it follows that these errors are related by

$$\frac{\Delta S_i}{S_i} - \frac{\Delta S_j}{S_j} = p_{ij}\Delta P + t_{ij}\Delta T. \quad (97)$$

From this it follows [cf. Eq. (95)] that a two-gate PSP measurement has a bias error given by

$$\Delta P^{(2)} = -\frac{t_{12}}{p_{12}}\Delta T, \quad (98)$$

where ΔT is the (generally unknown) amount by which the assumed temperature differs from the actual temperature. The corresponding noise-induced error is calculated by assuming (cf. Bell⁷ and Goss⁷⁸) that the signals S_i and S_j are shot-noise limited (the best possible scenario), with a relative variance given by

$$\left\langle (\Delta S_i / S_i)^2 \right\rangle = \frac{1}{kS_i} = \frac{1}{kNf_i s_i} \quad (j \text{ likewise}). \quad (99)$$

Here k is the number of detected photons per unit signal. As shown in Section 9.7, the root-mean-square (RMS) pressure error in a two-gate measurement may then be written as

$$\sigma_P^{(2)} = \frac{1}{|p_{12}| \sqrt{kN}} \left(\frac{1}{\sqrt{s_1}} + \frac{1}{\sqrt{s_2}} \right), \quad (100)$$

where N is the total number of pulses among the two gates, p_{12} is the relative partial pressure sensitivity at the operating point, and s_1 and s_2 are the single-pulse signals from Eq. (91). The result from Eq. (100) assumes that the pulse allocation fractions f_1 and f_2 have been selected optimally.

In a three-gate PSP measurement, the bias error attributable to unknown temperature is removed (i.e., $\Delta P^{(3)} = 0$), and the RMS pressure error becomes (see again Section 9.7):

$$\sigma_P^{(3)} = \frac{1}{|p_{12}t_{13} - p_{13}t_{12}| \sqrt{kN}} \left(\frac{|t_{13} - t_{12}|}{\sqrt{s_1}} + \frac{|t_{13}|}{\sqrt{s_2}} + \frac{|t_{12}|}{\sqrt{s_3}} \right). \quad (101)$$

Here p_{12} and t_{12} are the relative partial pressure and temperature sensitivities for the signal ratio r_{12} , and p_{13} and t_{13} are the relative partial pressure and temperature sensitivities for the signal ratio r_{13} . As is the case for the two-gate result from Eq.(100), the result from Eq. (101) assumes that the pulse allocation fractions (in this case, f_1, f_2 , and f_3) have been selected optimally.

Before the above errors are evaluated numerically, it is instructive to review graphically how the errors arise in a P - T diagram. To this effect, the heavy, solid line in Fig. 63 represents a contour of equal signal ratios R_{12} in a two-gate measurement as a function of pressure and temperature for a noise-free measurement. The actual values of pressure and temperature are represented by the operating point (P_0, T_0) . In the two-gate case from Fig. 63, the result of a temperature error ΔT is to cause a pressure bias error $\Delta P^{(2)}$ that depends on the relative temperature sensitivity η_{12} [see Eqs. (98) and (96)]. Because of shot noise, the equi-ratio contour is broadened, as shown by the gray band in Fig. 63, and the result is a corresponding random component of pressure, with a magnitude $\sigma_P^{(2)}$ given by Eq. (100).

By contrast, there is no bias error in the three-gate case depicted in Fig. 64, by virtue of the fact that the operating point (P_0, T_0) is defined by the intersection of two equi-ratio contours, R_{12} and R_{13} . However, a potentially much larger random error, $\sigma_P^{(3)}$, results, depending on the shape of the overlap region of the associated noise bands in Fig. 64. From Fig. 64 it is clear that the two ratio contours in a three-gate measurement must intersect at an appreciable angle in order not to stretch the diamond-shaped

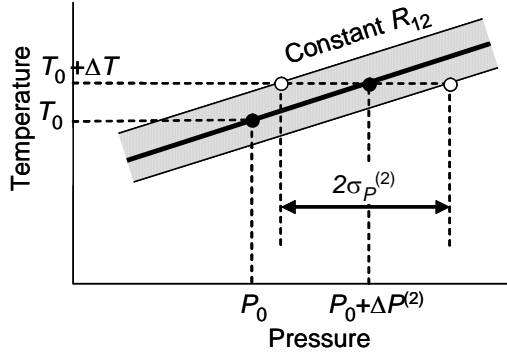


Figure 63. Error Sources in Two-Gate PSP

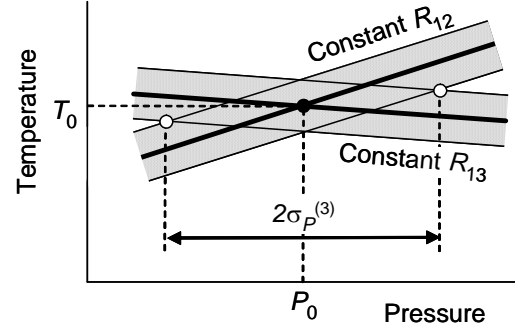


Figure 64. Error Sources in Three-Gate PSP

overlap region significantly. This effect is controlled by the leading denominator in Eq. (101), which deviates from zero precisely to the degree by which the temperature sensitivities η_{12} and η_{13} of the two-gate ratios differ from each other.

Whether the three-gate RMS error from Eq. (101) is smaller than the two-gate bias error from Eq. (98) depends on several factors—specifically, the temperature sensitivity of the two-gate measurement (which can be calibrated), the temperature error in the two-gate scheme (which is generally unknown), and the number of pulses over which the three-gate measurement is performed.

Comparison of the three-gate RMS error from Eq. (101) to the two-gate RMS error from Eq. (100) is possible if: 1) the same number of pulses, N , is used in both cases; 2) the single-pulse signals s_1 , s_2 , and s_3 in Eqs. (100) and (101) are roughly balanced in the sense that (for some common s_0) $s_1 = s_2 = s_0/2$ in Eq. (100) and $s_1 = s_2 = s_3 = s_0/3$ in Eq. (101); and 3) $t_{13} > t_{12} > 0$. In terms of the temperature sensitivities η_{12} and η_{13} for the two ratios from Eq. (96), it then follows that

$$\frac{\sigma_P^{(3)}}{\sigma_P^{(2)}} \cong \left| \frac{\eta_{13}}{\eta_{12} - \eta_{13}} \right|. \quad (102)$$

This result suggests again that, barring large temperature errors in the two-gate scheme, a necessary condition for a three-gate measurement to outperform a two-gate measurement is that the relative temperature sensitivities η_{12} and η_{13} in the three-gate scheme must be substantially different from each other.

9.5 PAINT OPTIMIZATION

The requirement that the relative temperature sensitivities η_{12} and η_{13} in a three-gate measurement scheme be substantially different from each other appears to be marginally the case for the work on PtTFPP in FEM by Mitsuo et al.¹² in Table 11, with $\eta_{12} = -2.9$ percent per degree Celsius and $\eta_{13} = -4.3$ percent per degree Celsius at ambient conditions. According to Eq. (102), this gives a three-gate RMS error that is nominally three times as large as the RMS error in a two-gate measurement.

Quite different results are obtained by Watkins et al.¹³ for a similar system (PtTFPP in FEM also) and equal gate times, i.e., $\eta_{12} = -1.14$ percent per degree Celsius and $\eta_{13} = -1.20$ percent per degree Celsius in Table 11. The fact that these relative sensitivities are equal within the accuracy of the data suggests that a useful three-gate measurement is not possible.

Likewise, for PtTFPP in FIB, Watkins et al.¹³ report results that yield relative sensitivities of $\eta_{12} = -0.45$ percent per degree Celsius and $\eta_{13} = -0.49$ percent per degree Celsius, as shown in Table 11. These values also seem to preclude a useful three-gate measurement, despite efforts by the authors of Ref. 13 to

use the paint in this manner. (Unpublished analysis by the present author on PtTFPP on FIB reaches the same conclusion: that PtTFPP in FIB does not lend itself to a three-gate measurement scheme.)

It is not clear why Mitsuo et al. and Watkins et al. obtain different results for PtTFPP in FEM, but the results for PtTFPP in FIB from Ref. 13 are not too surprising, in light of the fact that this paint has been described as “ideal” by its developers, in the sense that its temperature sensitivity is independent of pressure.⁹ Moreover, PtTFPP in FIB was developed with minimum temperature sensitivity in mind.

The authors of Ref. 113 have also claimed success with a multigate scheme for measuring pressure and temperature, but they have not formally published their results beyond the early report from Ref. 113.

Regarding results published to date, this leaves the work of Hradil et al. from Ref. 10, in which a temperature probe (the long-lived phosphor MFG) was added to a conventional PSP paint, Ru(dpp) in MTEOS. Although Hradil et al. do not consider a gating scheme per se, such a system may be analyzed by assuming that the fluorescence response can be characterized by two decay rates, γ_1 and γ_2 , with relative contributions in the proportion $x : (1-x)$. The response of such a system to delta-function excitation may be written as

$$S(t) = xe^{-\gamma_1 t} + (1-x)e^{-\gamma_2 t} . \quad (103)$$

With Eq. (91) it follows that the resulting single-pulse signal for a gate i is then given by

$$s_i = \frac{x}{\gamma_1} \left(e^{-\gamma_1 t_{i1}} - e^{-\gamma_1 t_{i2}} \right) + \frac{(1-x)}{\gamma_2} \left(e^{-\gamma_2 t_{i1}} - e^{-\gamma_2 t_{i2}} \right) . \quad (104)$$

The pressure and temperature sensitivities of the signal ratio $r_{ij} = s_i/s_j$ may now be written in terms of the partial derivatives of the rates γ_1 and γ_2 with respect to P and T as

$$p_{ij} = \frac{1}{r_{ij}} \frac{\partial r_{ij}}{\partial P} = \left(\frac{1}{s_i} \frac{\partial s_i}{\partial \gamma_1} - \frac{1}{s_j} \frac{\partial s_j}{\partial \gamma_1} \right) \frac{\partial \gamma_1}{\partial P} + \left(\frac{1}{s_i} \frac{\partial s_i}{\partial \gamma_2} - \frac{1}{s_j} \frac{\partial s_j}{\partial \gamma_2} \right) \frac{\partial \gamma_2}{\partial P} \quad (105)$$

and

$$t_{ij} = \frac{1}{r_{ij}} \frac{\partial r_{ij}}{\partial T} = \left(\frac{1}{s_i} \frac{\partial s_i}{\partial \gamma_1} - \frac{1}{s_j} \frac{\partial s_j}{\partial \gamma_1} \right) \frac{\partial \gamma_1}{\partial T} + \left(\frac{1}{s_i} \frac{\partial s_i}{\partial \gamma_2} - \frac{1}{s_j} \frac{\partial s_j}{\partial \gamma_2} \right) \frac{\partial \gamma_2}{\partial T} . \quad (106)$$

Given values of γ_1 , $\partial\gamma_1/\partial P$, and $\partial\gamma_1/\partial T$ for the first component and values γ_2 , $\partial\gamma_2/\partial P$, and $\partial\gamma_2/\partial T$ for the second component, the optimization of the three-gate measurement error from Eq. (101) may now be cast as the problem of establishing the optimum ratio x in Eq. (103), along with finding optimum gate times t_{11} , t_{12} , t_{21} , t_{22} , t_{31} , t_{32} ; optimum pulse allocation fractions f_1 , f_2 , f_3 ; an optimal pulse duration, t_p ; and an optimal pulse repetition period, t_c . A representative (nonoptimized) result is quoted in Table 11 for Hradil et al., assuming that $x = 0.5$, yielding $\eta_{12} = -2.61$ percent per degree Celsius and $\eta_{13} = 3.65$ percent per degree Celsius. These values produce a factor 0.6 when substituted into Eq. (102), suggesting that the implied three-gate temperature measurement not only is free from a temperature-bias error but also has an RMS error that is on the same order as the RMS error in a two-gate measurement.

Incidentally, it follows from Eqs. (103) through (106) that fluorescence decay that can be characterized by a single time constant, τ , does not lend itself to a three-gate scheme. This can be seen by setting $x = 1$ in Eq. (103), in which case the ratio t_{ij}/p_{ij} may be reduced to

$$\frac{t_{ij}}{p_{ij}} = \frac{\partial \tau}{\partial T} \bigg/ \frac{\partial \tau}{\partial P}. \quad (107)$$

This result is independent of the indices i and j and thus of the gating scheme.

9.6 DISCUSSION

The results from Section 9.5 demonstrate that a pressure-sensitive paint that is specifically designed to be sensitive to temperature (namely, by deliberate addition of a temperature probe) may lend itself better to a three-gate measurement scheme than does a paint in which only residual temperature dependence is present (i.e., unintentional temperature dependence that could not be removed during the design of the paint). In particular, the theoretical model that is developed here indicates that a critical performance parameter for a three-gate measurement scheme is the degree to which the relative temperature sensitivities of the two signal ratios differ from each other.

Other considerations have yet to be considered in full. For example, the temperature probe advocated by Hradil et al. in Ref. 13 has a lifetime that is several orders of magnitude greater than that of the pressure probe. This means that the repetition rate of the excitation source has to be reduced significantly, and that, as a result, measurement time will be increased. A temperature probe with a significantly shorter lifetime would alleviate this concern.

Other practical considerations will also have to be considered, such as the spatial homogeneity of the paint, particularly in the case that different probe molecules are mixed together in a single binder.

Finally, optimization of a PSP measurement system has to be considered not only for a fixed operating pressure and temperature, but also for the entire range of pressures and temperatures that are of interest in the measurement.

In summary, considerable further work is required to optimize three-gate PSP measurements. The theoretical model developed in this paper should serve as a useful tool for such further work.

9.7 APPENDIX 9A: DERIVATION OF TWO-GATE AND THREE-GATE SHOT-NOISE ERRORS

When the temperature-induced bias error for a two-gate PSP measurement is ignored, it follows from Eq. (107) that the pressure error is given by

$$\Delta P^{(2)} = \frac{1}{p_{12}} \left(\frac{\Delta S_1}{S_1} - \frac{\Delta S_2}{S_2} \right). \quad (108)$$

From this and Eq. (99) it follows that the resulting RMS pressure error is given by

$$\sigma_P^{(2)} \equiv \left\langle (\Delta P^{(2)})^2 \right\rangle^{1/2} = \frac{1}{|p_{12}| \sqrt{kN}} \left(\frac{1}{f_1 s_1} + \frac{1}{f_2 s_2} \right)^{1/2}. \quad (109)$$

With regard to the pulse allocation fractions f_1 and f_2 , this RMS error is minimized by the choice

$$f_1 : f_2 = \frac{1}{\sqrt{s_1}} : \frac{1}{\sqrt{s_2}}. \quad (110)$$

That is, most of the measurement time should be devoted to the gate with the smallest signal per pulse. From Eqs. (109) and (110), the result from Eq. (100) is obtained.

When a third signal, S_3 , is measured, a second signal ratio may be defined, say, $R_{13} \equiv S_1/S_3 = (f_1/f_3)r_{13}$, with associated relative partial pressure and temperature sensitivities p_{13} and t_{13} . A result similar to Eq. (97) may be written down for this second ratio. When combined with Eq. (97) for the first ratio, R_{12} , a linear system of equations in terms of the pressure error, ΔP , and the temperature error, ΔT , results. This system may be solved to yield the following errors for pressure and temperature in terms of the errors in the signals S_1 , S_2 , and S_3 :

$$\Delta P^{(3)} = \frac{(t_{13} - t_{12}) \frac{\Delta S_1}{S_1} - t_{13} \frac{\Delta S_2}{S_2} + t_{12} \frac{\Delta S_3}{S_3}}{p_{12}t_{13} - p_{13}t_{12}} \quad (111)$$

and

$$\Delta T^{(3)} = \frac{(p_{12} - p_{13}) \frac{\Delta S_1}{S_1} + p_{13} \frac{\Delta S_2}{S_2} - p_{12} \frac{\Delta S_3}{S_3}}{p_{12}t_{13} - p_{13}t_{12}}. \quad (112)$$

It can be shown that the results from Eqs. (111) and (112) are independent of the ordering of the gates in the ratios (e.g., S_2/S_1 vs. S_1/S_2) and independent of the choice of common gate (e.g., S_2 common vs. S_1 common, as is assumed here).

When the signals are shot-noise limited according to Eq. (99), the three-gate RMS pressure error becomes

$$\sigma_P^{(3)} \equiv \left\langle (\Delta P^{(3)})^2 \right\rangle^{1/2} = \frac{1}{|p_{12}t_{13} - p_{13}t_{12}| \sqrt{kN}} \left(\frac{(t_{13} - t_{12})^2}{f_1 s_1} + \frac{t_{13}^2}{f_2 s_2} + \frac{t_{12}^2}{f_3 s_3} \right)^{1/2}. \quad (113)$$

A similar result can be derived for the predicted RMS temperature error. In general, choices of gate times and pulse allocation fractions that optimize the pressure error from Eq. (113) will not optimize the corresponding temperature error, and vice versa. Here, the focus is on the pressure measurement error, which is minimized with respect to the pulse allocation fractions f_1 , f_2 , and f_3 when [cf. Eq. (110)]:

$$f_1 : f_2 : f_3 = \frac{|t_{13} - t_{12}|}{\sqrt{s_1}} : \frac{|t_{13}|}{\sqrt{s_2}} : \frac{|t_{12}|}{\sqrt{s_3}}. \quad (114)$$

For this choice of pulse allocation fractions, the RMS pressure error from Eq. (113) may be written in the form of Eq. (101).

9.8 ACKNOWLEDGMENT

Dr. Neil Watkins of the NASA Langley Research Center was kind enough to provide supplementary data to Ref. 13.

REFERENCES

1. Bell, J. H., Schairer, E. T., Hand, L. A., and Mehta, R. D., "Surface Pressure Measurements Using Luminescent Coatings," *Annual Review of Fluid Mechanics*, Vol. 33, 2001, pp. 155-206.
2. Liu, T., Campbell, B. T., Burns, S. P., and Sullivan, J. P., "Temperature- and Pressure-Sensitive Paints in Aerodynamics," *Applied Mechanics Review*, Vol. 50, 1997, pp. 227-246.
3. Sellers, M. E., "Application of Pressure-Sensitive Paint for Determining Aerodynamic Loads on a Scale Model of the F-16C," AIAA Paper 2000-2528, Denver, CO, June 2000.
4. Baker, W. M., "Recent Experiences with Pressure-Sensitive Paint Testing," AIAA Paper 2001-0135, January 2001.
5. Bencic, T. J., "Calibration of Detection Angle for Full Field Pressure-Sensitive Paint Measurements," AIAA Paper 2001-0307, January 2001.
6. Engler, R. H., Klein, C., and Trinks, O., "Pressure-Sensitive Paint Systems for Pressure Distributions Measurements in Wind Tunnels and Turbomachines," *Measurement Science and Technology*, Vol. 11, 2000, pp. 1077-1085.
7. Bell, J. H., "Accuracy Limitations of Lifetime-Based, Pressure-Sensitive Paint (PSP) Measurements," ICIASF Record, Cleveland, OH (IEEE, Piscataway, NJ), August 2001, pp. 11-16.
8. Bencic, T. J., "Temperature Correction for Pressure-Sensitive Paint," in *NASA Tech Briefs*, January 2000, pp. 50-51.
9. Puklin, E., Carlson, B., Gouin, S., Costin, C., Green, E., Ponomarev, S., Tanji, H., and Gouterman, M., "Ideality of Pressure-Sensitive Paint. I. Platinum Tetra (Pentafluorophenyl) Porphine in Fluoroacrylic Polymer," *Journal of Applied Polymer Science*, Vol. 77, 2000, pp. 2795-2804. (See also following three articles in same issue, by Gouin and Gouterman.)
10. Hradil, J., Davis, C., Mongey, K., McDonagh, C., and MacCraith, B. D., "Temperature-Corrected, Pressure-Sensitive Paint Measurements Using a Single Camera and a Dual-Lifetime Approach," *Measurement Science and Technology*, Vol. 13, 2002, pp. 1552-1557.
11. Hubner, J. P., Carroll, B. F., Schanze, K. S., Ji, H. F., and Holden, M. S., "Temperature- and Pressure-Sensitive Paint Measurements in Short-Duration, Hypersonic Flow," *AIAA Journal*, Vol. 39, 2001, 654-659.
12. Mitsuo, K., Egami, Y., Suzuki, H., Mizushima, H., and Asai, K., "Development of Lifetime Imaging System for Pressure-Sensitive Paint," AIAA Paper 2002-2909, June 2002.
13. Watkins, A. N., Jordan, J. D., Leighty, B. D., Ingram, J. L., and Oglesby, D. M., "Development of Next Generation Lifetime PSP Imaging System," *Proceedings of the 20th International Congress on Instrumentation in Aerospace Simulation Facilities*, Göttingen, Germany, August 2003, pp. 372-377.
14. Liu, T., Cattafesta, L. N., III, Radeztsky, R. H., and Burner, A. W., "Photogrammetry Applied to Wind Tunnel Testing," *AIAA Journal*, Vol. 38, 2000, pp. 964-971.
15. Ruyten, W., "More Photogrammetry for Wind Tunnel Testing," *AIAA Journal*, Vol. 40, No. 7, 2002, pp. 1277-1283.
16. Ruyten, W., "Automatic Registration of Luminescent Paint Images," *Proceedings of the 45th International Instrumentation Symposium*, Albuquerque, NM, May 2-6, 1999 (Instrumentation Society of America, Research Triangle Park, NC, 1999), pp. 279-288.
17. Ruyten, W., "Subpixel Localization of Synthetic References in Digital Images by Use of an Augmented Template," *Optical Engineering*, Vol. 41, No. 3, 2002, pp. 601-607.

18. Ruyten, W., "Automatic Image Registration for Optical Techniques in Aerodynamic Test Facilities," AIAA Paper 2004-2400, June 2004.
19. Bell, J. H., and McLachlan, B. G., "Image Registration for Luminescent Paint Sensors," AIAA Paper 93-0178, January 1993.
20. Bell, J. H., and McLachlan, B. G., "Image Registration for Pressure-Sensitive Paint Applications," *Experiments in Fluids*, Vol. 22, No. 1, 1996, pp. 78-86.
21. Ruyten, W., and Fisher, C. J., "Effects of Reflected Light in Luminescent Paint Measurements," *AIAA Journal*, Vol. 39, No. 8, 2001, pp. 1587-1592.
22. Ruyten, W., "Reconstruction of the Net Emission Distribution from the Total Radiance Distribution on a Reflecting Surface," *Journal of the Optical Society of America A*, Vol. 18, No. 1, January 2001, pp. 216-223.
23. Ruyten, W., Sellers, M., Clippard, R., and Craig, M., "Pressure-Sensitive Paint in Wind Tunnel Testing: a Computational Challenge," DoD HPC Users Group Meeting, Albuquerque, NM, June 5-8, 2000.
24. Ruyten, W., and Sellers, S., "On-Line Processing of Pressure-Sensitive Paint Images," AIAA Paper 2003-3947, June 2003.
25. Quinton, R., "An Introduction to Socket Programming," <http://www.uwo.ca/its/doc/courses/notes/socket/> (last accessed January 2004).
26. Le Sant, Y., "A Method to Correct Effects of Model Deformation on PSP Images," in Ref. 13, pp. 95-104.
27. Schairer, E. T., and Hand, L. A., "Measurements of Unsteady Aeroelastic Model Deformation by Stereo Photogrammetry," *Journal of Aircraft*, Vol. 36, No. 6, 1999, pp. 1033-1040.
28. Ruyten, W., "Model Attitude Determination in a Wind Tunnel with a Luminescent Paint Data System," *AIAA Journal*, Vol. 38, No. 9, 2000, pp. 1692-1697.
29. Ruyten, W., "Extension of Subpixel Augmented Template Matching to Imperfectly Rendered Binary Targets," *Optical Engineering*, Vol. 43, No. 3, March 2004, pp. 639-647.
30. Ruyten, W., "Model Attitude Measurement with an Eight-Camera Pressure-Sensitive Paint System," AIAA Paper 2000-0831, January 2000.
31. Foley, J. D., and Van Dam, A., *Fundamentals of Interactive Computer Graphics*, Addison-Wesley, Reading, MA, 1982, pp. 560-561.
32. Morgan, J. S., Slater, D. C., Timothy, J. G., and Jenkins, E. B., "Centroid Position Measurements and Subpixel Sensitivity Variations with the MAMA Detector," *Applied Optics*, Vol. 28, No. 6, 1989, pp. 1178-1192.
33. Fernández, X., and Amat, J., "Detection of Small-Size Synthetic References in Scenes Acquired with a Pixilated Device," *Optical Engineering*, Vol. 36, No. 11, 1997, pp. 3073-3080.
34. Frischholz, R. W., and Spinnler, K. P. "Class of Algorithms for Real-Time Subpixel Registration," in *Computer Vision for Industry*, SPIE Vol. 1989, 1993, pp. 50-59.
35. Rosenfeld, A., and Kak, A. C., *Digital Picture Processing*, 2nd Ed., Academic, New York, NY, 1982, Sec. 9.4.
36. Ballard, D. H., and Brown, C. M., *Computer Vision*, Prentice-Hall, Englewood Cliffs, NJ 1982, Sec. 3.2.

37. Tian, Q., and Huhns, M. N., "Algorithms for Subpixel Registration," *Computer Vision, Graphics, and Image Processing*, Vol. 35, 1986, pp. 220-233.
38. Olson, F., "Subpixel Localization and Uncertainty Estimation Using Occupancy Grids," *Proceedings on Robotics and Automation*, IEEE, 1999, pp. 1987-1992.
39. Olson, F., "Maximum-Likelihood Template Matching," *Proceedings on Computer Vision and Pattern Recognition*, IEEE, 2000, pp. 52-57.
40. Mitchell, O. R., Lyvers, E. P., Dunkelberger, K. A., and Akey, M. L., "Recent Results in Precision Measurements of Edges, Angles, Areas, and Perimeters," *Proceedings of SPIE*, Vol. 730, 1986, pp. 123-134.
41. Bosco, S., and Trivi, M., "Correlation-like algorithm for superresolution analysis," *Optics Communications*, Vol. 115, 1995, pp. 444-448.
42. Tanaka, K., Sano, M., Ohara, S., and Okudaira, M., "A Parametric Template Method and Its Application to Robust Matching," *Proceedings on Computer Vision and Pattern Recognition*, IEEE, 2000, pp. 620-627.
43. Bose, M., and Amir, I., "Design of Fiducials for Accurate Registration Using Machine Vision," *IEEE Transactions of the PAMI*, Vol. 12, No. 12, 1990, pp. 1196-1200.
44. Chiorboli, G., and Vecchi, G. P., "Comments on 'Design of Fiducials for Accurate Registration Using Machine Vision,'" *IEEE Transactions of the PAMI*, Vol. 15, No. 12, 1993, pp. 1330-1332.
45. Tubbs, J. D., "A Note on Binary Template Matching," *Pattern Recognition*, Vol. 22, No. 4, 1989, pp. 359-365.
46. Fitts, J. M., "Precision Correlation Tracking via Optimal Weighting Functions" in *Proceedings of the IEEE Conference on Decision and Control*, Vol. 1, 1979, pp. 280-283.
47. Fernández, X., "Template Matching of Binary Targets in Grey-Scale Images: a Nonparametric Approach," *Pattern Recognition*, Vol. 30, No. 7, 1997, pp. 1175-1182.
48. Paglieroni, W., Ford, G. E., and Tsujimoto, E. M., "The Position-Orientation Masking Approach to Parametric Search for Template Matching," *IEEE Transactions of the PAMI*, Vol. 16, No. 7, 1994, pp. 740-747.
49. Liu, T., and Sullivan, J. P., *Pressure and Temperature Sensitive Paints* (Springer, 2005, XI, 325 p.), issued in Experimental Fluid Mechanics series.
50. Mebarki, Y., Grenier, M., Ellis, F., Bureau, J., Orchard, D., and Tang, F., "Study of the Flow Around an External Fuel Tank Mounted Under a CR-18 Wing Using Combined PSP and Schlieren Techniques," AIAA Paper 2005-5223, June 2005.
51. Mitsuo, K., Asai, K., Takahashi, A., and Mizushima, H., "Advanced Lifetime PSP Imaging System for Simultaneous Pressure and Lifetime Measurement," AIAA Paper 2004-2188, June 2004.
52. Kurita, M., Nakakita, K., Mitsuo, K., and Watanabe, S., "Data Processing of Pressure-Sensitive Paint for Industrial Wind Tunnel Testing," AIAA Paper 2004-2189, June 2004.
53. Park, S.-H., and Sung, H.-J., "Correlation-Based Image Registration for Pressure-Sensitive Paint," AIAA Paper 2004-0882, January 2004.
54. Wong, C., Amir, M., Lada, C., Kontis, K., and Boudoin, M., "Molecular Image Sensing for Pressure and Temperature Surface Mapping of Aerodynamic Flows," AIAA Paper 2004-0598, January 2004.

55. Klein, C., Engler, R. H., Henne, U., and Sachs, W. E., "Application of Pressure-Sensitive Paint for Determination of the Pressure Field and Calculation of the Forces and Moments of Models in a Wind Tunnel," *Experiments in Fluids*, Vol. 39, No. 2, August 2005, pp. 475-483.
56. Le Sant, Y., Durand, A., and Mérienne, M., "Image Processing Tools Used for PSP and Model Deformation Measurements," AIAA Paper 2005-5007, June 2005.
57. Goss, L., Jones, G., Crafton, J., and Fonov, S., "Temperature Compensation for Temporal (Lifetime) Pressure Sensitive Paint Measurements," AIAA Paper 2005-1027, January 2005.
58. Bell, J. H., "Applications of Pressure-Sensitive Paint to Testing at Very Low Flow Speeds," AIAA Paper 2004-0478, January 2004.
59. Khalil, G. E., Coston, C., Crafton, J., Jones, G., Grenoble, S., Gouterman, M., Callis, J. B., and Dalton, L. R., "Dual-Luminophor Pressure-Sensitive Paint I. Ratio of Reference Sensor Giving a Small Temperature Dependency," *Sensors and Actuators B*, Vol. 97, No. 1, January 2004, pp. 13-21.
60. Kose, M. E., Omar, A., Virgin, C. A., Carroll, B. F., and Schanze, K. S., "Principal Component Analysis Calibration Method for Dual-Luminophore Oxygen and Temperature Sensor Films: Application to Luminescence Imaging," *Langmuir*, Vol. 21, No. 20, September 2005, pp. 9110-9120.
61. Gregory, J. W., and Sullivan, J. P., "Effect of Quenching Kinetics on the Unsteady Response of Pressure-Sensitive Paint," AIAA Paper 2004-0879, January 2004.
62. Ruyten, W., and Sellers, M., "On-Line Processing of Pressure-Sensitive Paint Images," *Journal of Aerospace Computing, Information, and Communication*, Vol. 1, September 2004, pp. 372-382.
63. Ruyten, W., "Assimilation of Physical Chemistry Models for Lifetime Analysis of Pressure-Sensitive Paint," *AIAA Journal*, Vol. 43, No. 3, March 2005, pp. 465-471.
64. Ruyten, W., "Correction of Self-Illumination and Spectral-Leakage Effects in Luminescent Paint Measurements," *Applied Optics*, Vol. 36, No. 14, May 1997, pp. 3079-3085.
65. Ruyten, W., "Sting Deflection Model for Automatic Image Registration in Wind-Tunnel Testing," *Journal of Aircraft*, Vol. 43, No. 3, May-June 2006, pp. 853-855.
66. Bell, J. H., and Sellers, M. E., "Pressure Sensitive Paint Measurements on a Space Shuttle Model with the Luminescent Lifetime Technique," *Proceedings of the 21st International Congress on Instrumentation in Aerospace Simulation Facilities*, Sendai, Japan, August 2005, pp. 195-206.
67. Brown, N. R., Benne, M. E., and Kammeyer, M. E., "Factors Influencing Camera Selection for the Boeing Pressure-Sensitive Paint System," AIAA Paper 2004-0603, January 2004.
68. Sellers, M. E., "Advances in AEDC's Lifetime Pressure-Sensitive Paint Program," AIAA Paper 2005-7638, November 2005.
69. Bell, J. H., and Schairer, E. T., "Texture Mapping for Display and Analysis of Image Data on 3D Surfaces," AIAA Paper 2002-0745, January 2002.
70. Carraway, E. R., Demas, J. N., DeGraff, B. A., and Bacon, J. R., "Photophysics and Photochemistry of Oxygen Sensors Based on Luminescent Transition-Metal Complexes," *Analytical Chemistry*, Vol. 63, 1991, pp. 337-342.
71. Mills, A., "Response Characteristics of Optical Sensors for Oxygen: Models Based on a Distribution in τ_0 or k_q ," *Analyst*, Vol. 124, 1999, pp. 1301-1307.
72. Mills, A., "Response Characteristics of Optical Sensors for Oxygen: a Model Based on a Distribution in τ_0 and k_q ," *Analyst*, Vol. 124, 1999, pp. 1309-1314.

73. Vollan, A., and Alati, L., "A New Optical Measurement System (OPMS)," *Proceedings of the 14th International Congress on Instrumentation in Aerospace Simulation Facilities*, Rockville, MD, October 1991, pp. 10-16.
74. Kavandi, J., Callis, J., Gouterman, M., Khalil, G., Wright, D., Burns, D., and McLachlan, B., "Luminescent Barometry in Wind Tunnels," *Review of Scientific Instruments*, Vol. 61, 1990, pp. 3340-3347.
75. Schanze, K. S., Carroll, B. F., Korotkevitch, S., and Morris, M. J., "Temperature Dependence of Pressure-Sensitive Paint," *AIAA Journal*, Vol. 35, February 1997, pp. 306-310.
76. Coyle, L. M., and Gouterman, M., "Correcting Lifetime Measurements for Temperature," *Sensors and Actuators*, Vol. B61, 1999, pp. 92-99.
77. Woodmansee, M. A., and Dutton, J. C., "Treating Temperature-Sensitivity Effects of Pressure-Sensitive Paint Measurements," *Experiments in Fluids*, Vol. 24, 1998, pp. 163-174.
78. Goss, L. P., Trump, D. D., Sarka, B., Lydick, L. N., and Baker, W. M., "Multidimensional, Time-Resolved, Pressure-Sensitive Paint Techniques: a Numerical and Experimental Comparison," AIAA Paper 2000-0832, January 2000.
79. Holmes, J. W., "Analysis of Radiometric, Lifetime, and Fluorescent Lifetime Imaging for Pressure-Sensitive Paint," *The Aeronautical Journal*, Vol. 102, No. 1014, April 1998, pp. 189-194.
80. Ruyten, W., "Assimilation of Physical Chemistry Models for Lifetime Analysis of Pressure-Sensitive Paint," AIAA Paper 2004-0880, January 2004.
81. Ruyten, W., and Sellers, M., "Lifetime Analysis of the Pressure-Sensitive Paint PtTFPP in FIB," AIAA Paper 2004-0881, January 2004.
82. Lakowicz, J. R., *Principles of Fluorescence Spectroscopy*, 2nd Ed. (Kluwer Academic, New York, 1999), Chapters 4 and 5.
83. Kalyanasundaram, K., *Photochemistry in Microheterogeneous Systems* (Academic, Orlando, 1987), Chapter 1.
84. Liu, Y.-S., and Ware, W. R., "Photophysics of Polycyclic Aromatic Hydrocarbons Adsorbed on Silica Gel Surfaces. 1. Fluorescence Lifetime Distribution Analysis: An Ill-Conditioned Problem," *Journal of Physical Chemistry*, Vol. 97, 1993, pp. 5980-5986.
85. Wang, H., and Harris, J. M., "Origins of Bound-Probe Fluorescence Decay Heterogeneity in the Distribution of Binding Sites on Silica Surfaces," *Journal of Chemical Physics*, Vol. 99, 1995, pp. 16999-17009.
86. James, D. R., Liu, Y.-S., De Mayo, P., and Ware, W. R., "Distributions of Fluorescence Lifetimes: Consequences for the Photophysics of Molecules Adsorbed on Surfaces," *Chemical Physics Letters*, Vol. 120, 1985, pp. 460-465.
87. Förster, Th., "Experimentelle und Theoretische Untersuchung des Zwischenmolekularen Übergangs von Elektronenanregungsenergie," *Zeitschrift für Naturforschung*, Vol. 4A, 1949, p. 321.
88. Draxler, S., Lippitsch, M. E., Klimant, I., Kraus, H., and Wolfbeis, O. S., "Effects of Polymer Matrices on the Time-Resolved Luminescence of a Ruthenium Complex Quenched by Oxygen," *Journal of Physical Chemistry*, Vol. 99, 1995, pp. 3162-3167.
89. Draxler, S., and Lippitsch, M. E., "Lifetime-Based Sensing: Influence of the Microenvironment," *Analytical Chemistry*, Vol. 68, 1996, pp. 753-757.
90. Lakowicz, J. R., *Principles of Fluorescence Spectroscopy*, 2nd Ed. (Kluwer Academic, NY, 1999), Section 4.10.D, Chapters 13-15.

91. Wagner, B. D., and Ware, W. R., "Recovery of Fluorescence Lifetime Distributions: Application to Förster Transfer in Rigid and Viscous Media," *Journal of Physical Chemistry*, Vol. 94, 1990, pp. 3489-3494.
92. Siemiarczuk, A., Wagner, B. D., and Ware, W. R., "Comparison of the Maximum Entropy Method and Exponential Series Methods for the Recovery of Distributions of Lifetimes from Fluorescence Lifetime Data," *Journal of Physical Chemistry*, Vol. 94, 1990, pp. 1661-1666.
93. Livesey, A. K. and Brochon, J. C., "Analyzing the Distribution of Decay Constants in Pulse-Fluorimetry Using the Maximum Entropy Method," *Biophysical Journal*, Vol. 52, November 1987, pp. 693-706.
94. Brochon, J. C., Livesey, A. K., Pouget, J., and Valeur, B., "Data Analysis in Frequency-Domain Fluorometry by the Maximum Entropy Method—Recovery of Fluorescence Lifetime Distributions," *Chemical Physics Letters*, Vol. 174, 1990, pp. 517-522.
95. Siemiarczuk, A., and Ware, W. R., "A Novel Approach to Analysis of Pyrene Fluorescence Decays in Sodium Dodecylsulfate Micelles in the Presence of Cu²⁺ Ions Based on the Maximum Entropy Method," *Chemical Physics Letters*, Vol. 160, 1989, pp. 285-290.
96. Shaver, J. M., and McGown, L. B., "Maximum Entropy Method for Frequency Domain Fluorescence Lifetime Analysis. 1. Effects of Frequency Range and Random Noise," *Analytical Chemistry*, Vol. 68, 1996, pp. 9-17.
97. McGown, L. B., Hemmingsen, S. L., Shaver, J. M., and Geng, L., "Fluorescence Lifetime Distribution Analysis for Fluorescence Fingerprinting and Characterization," *Applied Spectroscopy*, Vol. 49, 1995, pp. 60-66.
98. Swaminathan, R., and Periasamy, N., "Analysis of Fluorescence Decay by the Maximum Entropy Method: Influence of Noise and Analysis Parameters on the Width of the Distribution of Lifetimes," *Proceedings of the Indian Academy of Sciences*, Vol. 108, 1996, pp. 39-49.
99. Vinogradov, S. A., and Wilson, D. F., "Recursive Maximum Entropy Algorithm and Its Application to the Luminescence Lifetime Distribution Recovery," *Applied Spectroscopy*, Vol. 54, 2000, pp. 849-855.
100. Press, W. H., Teukolsky, S. A., Vetterling, W. T., and Flannery, B. P., *Numerical Recipes in Fortran*, 2nd Ed., Cambridge University Press, New York, NY, 1986, Sec. 18.7.
101. Ibid., Section 15.4.
102. Bryan, R. K., and Skilling, J., "Deconvolution by Maximum Entropy, as Illustrated by Application to the Jet of M87," *Monthly Notices of the Royal Astronomical Society*, Vol. 191, 1980, pp. 69-79.
103. James, D. R., and Ware, W. R., "A Fallacy in the Interpretation of Fluorescence Decay Parameters," *Chemical Physics Letters*, Vol. 120, 1985, pp. 455-459.
104. Ruyten, W., "Oxygen Quenching of PtTFPP in FIB Polymer: a Sequential Process?" *Chemical Physics Letters*, Vol. 394, 2004, pp. 101-104.
105. Bedlek-Anslow, J. M., Hubner, J. P., Carroll, B. F., and Schanze, K. S., "Microheterogeneous Oxygen Response in Luminescence Sensor Films," *Langmuir*, Vol. 16, 2000, pp. 9137-9141.
106. Bonzagni, N. J., Baker, G. A., Pandey, S., Niemeyer, E. D., and Bright, F. V., "On the Origin of the Heterogeneous Emission from Pyrene Sequestered Within Tetramethylorthosilicate-Based Xerogels: a Decay-Associated Spectra and O₂ Quenching Study," *Journal of Sol-Gel Science & Technology*, Vol. 17, 2000, pp. 83-90.

107. Winslow, N. A., Carroll, B. F., and Kurdila, A. J., "Model Development and Analysis of the Dynamics of Pressure-Sensitive Paints," *AIAA Journal*, Vol. 39, 2001, pp. 660-666.
108. Lu, X., Han, B.-H., and Winnik, M. A., "Characterizing the Quenching Process for Phosphorescent Dyes in Poly{[(n-butylamino)thionyl]phosphazene} Films," *Journal of Physical Chemistry B*, Vol. 107, 2003, 13349-13356.
109. Gouin, S., and Gouterman, M., "Ideality of Pressure-Sensitive Paint. II. Effect of Annealing on the Temperature Dependence of the Luminescence," *Journal of Applied Polymer Science*, Vol. 77, 2000, 2805-2814.
110. Hurtubise, R. J., Ackerman, A. H., and Smith, B. W., "Mechanistic Aspects of the Oxygen Quenching of the Solid-Matrix Phosphorescence of Perdeuterated Phenanthrene on Partially Hydrophobic Paper," *Applied Spectroscopy*, Vol. 55, No. 4, 2001, 490-495.
111. Vallee, R. A. L., Cotlet, M., Hofkens, J., De Schryver, F. C., and Mullen, K., "Spatially Heterogeneous Dynamics in Polymer Glasses at Room Temperature Probed by Single Molecule Lifetime Fluctuations," *Macromolecules*, Vol. 36, 2003, 7752-7758.
112. Maliwal, B. P., Gryczynski, Z., and Lakowicz, J. R., "Long-Wavelength, Long-Lifetime Luminophores," *Analytical Chemistry*, Vol. 73, No. 17, 2001, pp. 4277-4285.
113. Davies, A. G., Bedwell, D., Dunleavy, M., and Brownjohn, N., "Pressure-Sensitive Paint Limitations and Solutions," *Proceedings of the 17th International Congress on Instrumentation in Aerospace Simulation Facilities*, Pacific Grove, CA, September-October 1997, pp. 11-21.